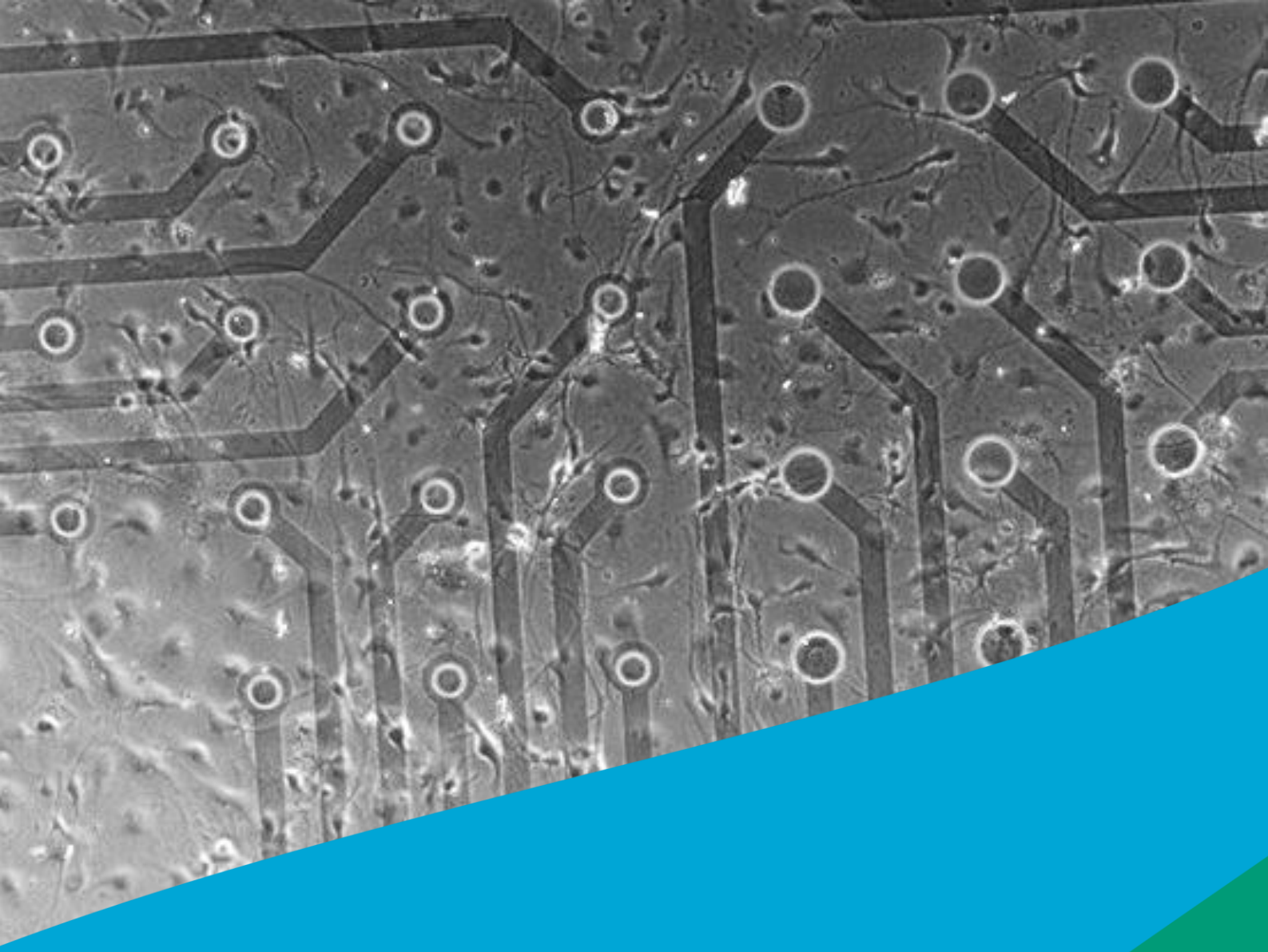

PEDOT:PSS for the development of neuronal cultures: differentiation, biocompatibility and electrical recording

Author: Eduardo Aceves Alfaro
Date: 08-08-2025

TU Delft

PEDOT:PSS for the development of neuronal cultures: differentiation, biocompatibility and electrical recording

By

E. Aceves Alfaro

In partial fulfilment of the requirements for the degree of:

Master of Science
in Biomedical Engineering

at the Delft University of Technology,
to be defended publicly on Wednesday August 27, 2025, at 9:00 AM.

Supervisor:	Prof. dr. A. Savva	TU Delft
Thesis committee:	Prof. dr. M. Mastrangeli,	TU Delft
	Prof. dr. A. Accardo,	TU Delft
	Prof. dr. W. Serdijn,	TU Delft

Contents

Abstract

Neurons are fundamental to cognitive and motor functions, relying on intricate electrical and chemical signaling. However, neurological diseases such as Parkinson's, Alzheimer's, and Amyotrophic Lateral Sclerosis impair neural function, posing a growing challenge due to aging populations and limited regenerative capacity of the nervous system. Advances in induced pluripotent stem cells (iPSCs) have enabled human-derived neuronal models for disease study, while neural interfaces, particularly microelectrode arrays (MEAs), facilitate electrophysiological investigation both in vivo and in vitro.

This thesis explores the use of poly(3,4-ethylenedioxythiophene):poly(styrene sulfonate) (PEDOT:PSS), a conductive polymer with mixed ionic-electronic conductivity, as a superior neural interface for *in vitro* neuronal cultures. The study addresses three key objectives: (1) elucidating the electrochemical mechanisms underlying PEDOT:PSS's performance, (2) validating its biocompatibility and functionality in recording neuronal activity, and (3) establishing protocols for neuronal differentiation and maturation on PEDOT:PSS substrates.

First, a scientific literature search was performed to understand the current standing of PEDOT:PSS as a neuronal interface, exploring the different applications and approaches scientific peers have established, and understanding the working mechanisms of the conduction behind their work. This was complemented with the practical experience with PEDOT:PSS, showcasing its biocompatibility and methods to improve conductivity.

Secondly, neuronal recordings in vitro were made to assess the performance of a custom-built PEDOT:PSS-based MEA and the meaning behind the electrophysiological recordings. Data acquisition, pre-processing, and analysis are discussed to understand the results obtained. Key findings include the performance success of the MEA, while also explaining the shortcomings of the implemented processing algorithms.

Lastly, a motor neuron differentiation protocol from iPSCs was established to further investigate the role of PEDOT:PSS in such context for later studies. The success of the protocol was assessed by morphological, functional, and immunostaining assays.

Future directions include optimizing conductivity through acid treatments, integrating PEDOT:PSS into motor neuron maturation protocols, and exploring electrical stimulation and 3D culture systems. This work contributes to the development of advanced bioelectronic tools for neuronal models and engineering.

Acknowledgments

I have so much to be thankful for and so many people to thank, not only for my thesis, but for my whole academic journey here at TU Delft. Firstly, I extend my gratitude to Dr. Achilleas Savva for welcoming into the Bioelectronics department to be part of this project that has left me with so much. I truly appreciate all the support that has been given to me during this project: all the background work to make this project possible, every discussion we had, and all the guidance and confidence you have given me. I also want to express my gratitude to the rest of the ReBooT group: David, Malina, Ryan, Rajvi, Misha, Yangshan, Liwen, Tawab…, and particularly to (future Dr.) Mustafeez Shah, who introduced me the world of electrochemistry and microelectrode arrays. I would also like to add the people at the MEMPhyS group led by Dr. Massimo Mastrangeli who also helped me with projects outside my thesis, and particular to (future Dr.) Alireza Tajeddin, whose guidance and friendliness helped me develop skills in the clean room and microelectronic field.

I want to thank Dr. Jean-Pierre Frimat, whose knowledge of neural cultures, electrophysiology, and microelectrode arrays was paramount for this project, and I certainly wouldn't have achieved or learned as much without your help.

I would also like to thank the people I met at Bi\ond Solutions: Niko, Mitchell, Cinzia, Lucas, Anish, Vishnu, Durotimi, Tien, Raffaella, Tawab (again, how fun is that!), and, of course, Dr. Marieke Aarts, who guided me and supervised me during the motor neuron culture process of this project. Thank you for the support and encouragement you gave me whenever I ran into issues with the cells, and discussing with me the day-to-day findings and planning for a successful cell culture. Thanks everyone for the welcoming and warm environment I enjoyed and for showing me a glimpse of what research looks like outside of academia.

I express my deepest gratitude to TU Delft's Universiteitsfonds, specifically the Justus & Louise van Effen Excellence Scholarship committee, whose decision to grant me the scholarship has forever changed my life. I was able to not only attend TU Delft but also live and enjoy my time here in the Netherlands without having to stress over making ends meet. I feel beyond grateful for the opportunity they have given me.

Lastly, but certainly not least, I want to thank my family who always stood by me and supported me in my journey, not only academically, but also in the Netherlands, this initially foreign land that I now begin to call home. And to Lizeth, thanks for being part of this journey with me, it is indescribable how important you have been to me and how far I have come, always inspiring me to do my best. All my achievements would not have been possible without the constant support and love you have given me.

Thank you all!
Eduardo Aceves Alfaro

1 Introduction

1.1 Neurons and neuropathology

Neurons are exciting, in every sense of the word. From the neurons that signal your eyes to smoothly follow these words, to the ones that allow you to recognize and understand these shapes we call letters, they are indispensable for making sense of the world and work in a highly coordinated fashion to stimulate, inhibit, or modulate other neurons to interact with our surroundings. These cells experience across the cell membrane short electrical pulses known as action potentials or spikes, which are used for fast communication with other neurons [1]. Most interneuron communication is not strictly electrical, but rather through chemical signals: action potentials trigger the release of neurotransmitters (spike-causing molecules) at the synapse, where the axon of one neuron meets another neuron [2]. For an action potential to occur, a neuron must experience a depolarization of their membrane from rest (around -60 mV) to a threshold (around -50 mV), which then rapidly changes the transmembrane voltage of the neuron to +40 mV and just as fast repolarizes back to the resting potential [2], [3]. This exciting mechanism is present in most types of neurons, of which cortical and motor neurons are of interest for this thesis.

Cortical neurons are highly complex neurons located on the brain cortex that have many higher-order functions, most uniquely they are responsible for cognition [4]. They are present in every brain lobe and contain a diverse set of neurons, e.g. interneurons and pyramidal neurons [5]. Motor neurons, on the other hand, refer to the neurons responsible for the voluntary and involuntary stimulation of muscles and glands [6]. They are divided into two upper and lower motor neurons, with the latter innervating the muscles and receiving the signals from the former, which begin with cortical neurons.

1.1.1 Neural diseases

Despite their unparalleled importance in the body, the nervous system is known for its poor regeneration when wounded or sick, making it particularly vulnerable to long-term degenerative diseases. Diseases such as Parkinson's, Alzheimer's, Huntington's, Multiple Sclerosis, and Amyotrophic Lateral Sclerosis are incurable ailments that decay neural health, producing failures in memory, cognition, sensation, and/or mobility [7]. Such diseases are associated with advanced age, which comes as a growing challenge as global life expectancy increases and the number of elderly individuals is projected to be 1.5 billion by 2050 [8], and with the 3.4 billion people currently affected by neurological conditions [9], it is imperative to solve this problem.

The study of neurological diseases is an active field of study that improves the pathophysiological understanding, develops novel detection biomarkers, and assesses new potential treatments [10]. A popular approach is the development of a model that mirrors the critical characteristics of the disease, and usually has been done with animals to a successful degree [7]. However, a rapidly growing field is the use of stem cells to generate human models and disease with the aid of advanced cell culture techniques.

1.1.2 Induced pluripotent stem cells

Induced Pluripotent Stem Cells, hereinafter referred to as iPSCs, are a groundbreaking discovery that has opened the door for a new kind of cellular research [11]. Taking a step back, stem cells are a critical foundation of multicellular life and complex organisms thanks to their ability to rapidly multiply, self-renew, and differentiate into a range of different cell types depending on their potential. Pluripotent stem cells can differentiate into most, if not all, kinds of cells with the important distinction of not being able to create a new organism on their own, as opposed to totipotent stem cells. Initially, these types of cells have been referred to as embryonic stem cells, as they are derived from the inner cell mass of blastocytes in early development. As such, these cells are invaluable for developmental research, genetics, and even disease modelling.

However, extracting human embryonic stem cells has been subject of much ethical discussion and technical difficulty [11], [12]. On the other hand, iPSCs offer the same genetic potential without the drawbacks of embryonic stem cells, as they are derived from somatic cells that have been reverted from nonexistent differential capacity to pluripotency. This was first achieved through a specific set of factors added to the culture medium, a method that has been improved upon since their discovery [13]. Consequently, research in iPSC technology has yielded advancements in cell therapy, personalized medicine, therapeutics, cellular and developmental models, drug screening, genetic and tissue engineering, and disease study [14]. iPSC-derived lines were used in this work. Firstly, commercially obtained motor neuron progenitors were differentiated under different conditions to establish several culture and preservation parameters. Lastly, commercially available iPSC-cortical neurons were used in different experiments.

1.2 Neural Interfaces

Neural interfaces, as the name suggests, are devices that come into contact with neural tissue, either on the brain or *in vitro* neural cultures, and can perform sensing and/or stimulating functions. They are paramount in advancing our understanding of the brain and its diseases. Such examples include the groundbreaking patch-clamp electrode, flexible electrocorticogram, nerve cuffs, and *in vitro* microelectrode arrays, as seen on **Figure 1-1**. Each application requires tailored design considerations and requirements, with the former two examples being predominantly used for the short term in contrast to the latter two that can have a prolonged use. The last example, the microelectrode array, is of interest in this thesis, and facilitates the recording and/or stimulation of cultured neurons in a specific area thanks to electrode sizes comparable to the size of the neurons (10^{-6} m scale). Planar-type electrodes made of nontoxic metals like gold, titanium nitride, and platinum, are typically used to measure extracellular recordings of the neural activity, which is less sensitive but last longer than intracellular recordings (e.g. patch-clamp) [15]. Ongoing improvement efforts for this type of electrode focus on overcoming high impedance, large electrode size, and biocompatibility. This can be done by coating the electrodes, introducing nanomaterials, or changing the electrode material altogether. This thesis delves into the latter approach, in particular with the use of conductive polymers, thanks to their favorable biocompatibility, mechanical properties, and electrical conductivity [16].

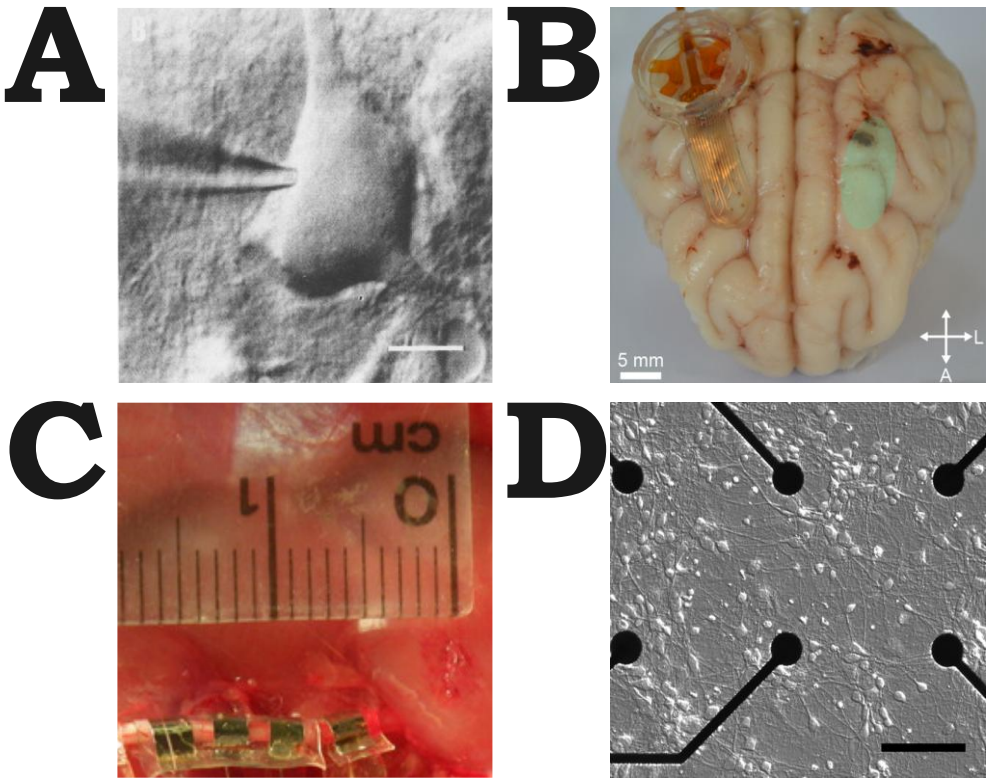

Figure 1-1. Examples of neural interfaces. **A)** Patch clamp of a neuron *[17]*. Scale bar: 10 µm. **B)** Electrocorticograph array on a pig brain model *[18]*. Green area is the position of the array on the contralateral hemisphere. **C)** Nerve cuff on a rat sciatic nerve *[19]*. **D)** Microelectrode array with neocortical cells at DIV 6 *[20]*. Scale bar: 100 µm.

1.3 Organic bioelectronics

Conductive polymers are a group of electroactive polymers that have similar properties to semiconductors and some metals, namely electrically, while being made of organic materials and also exhibiting biocompatible properties [16], [21]. Furthermore, conductive polymers are relatively easy to synthesize through chemical and electrochemical processes from the macro- to the nanoscale, making it compatible with existing microfabrication technologies [21]. As such, there is an interest in the bioelectronics research field for their application in neural studies, such as biosensing [22] and electrical stimulation [23].

Poly(3,4-ethylenedioxythiophene):poly(styrene sulfonate), commonly referred to as PEDOT:PSS, refers to a conductive copolymer that has remarkable properties for bioelectronics: biocompatibility, electronic conductivity, ionic conductivity, electrochemical stability, volumetric capacitance, and microfabrication friendly [24]. The polymer PEDOT has poor solubility but allows for hole conductivity, while PSS stabilizes PEDOT in aqueous solutions and permits ionic conductivity [25], [26], the polymer chains can be seen in **Figure 1-2A**. The interaction between this two polymers results in a colloidal dispersion solution with micelles containing PSS-rich shells and PEDOT-rich cores, or grains, a structure that largely remains in film form [27]. In an electrolyte, the PSS-rich regions allow for charges to enter deep in to the film through solvated ion vehicle transport, as seen on the yellow shaded region in **Figure 1-2B**, greatly expanding the effective surface are of the material for electronic conductivity that is coupled to this mobile ions [28]. Thus,

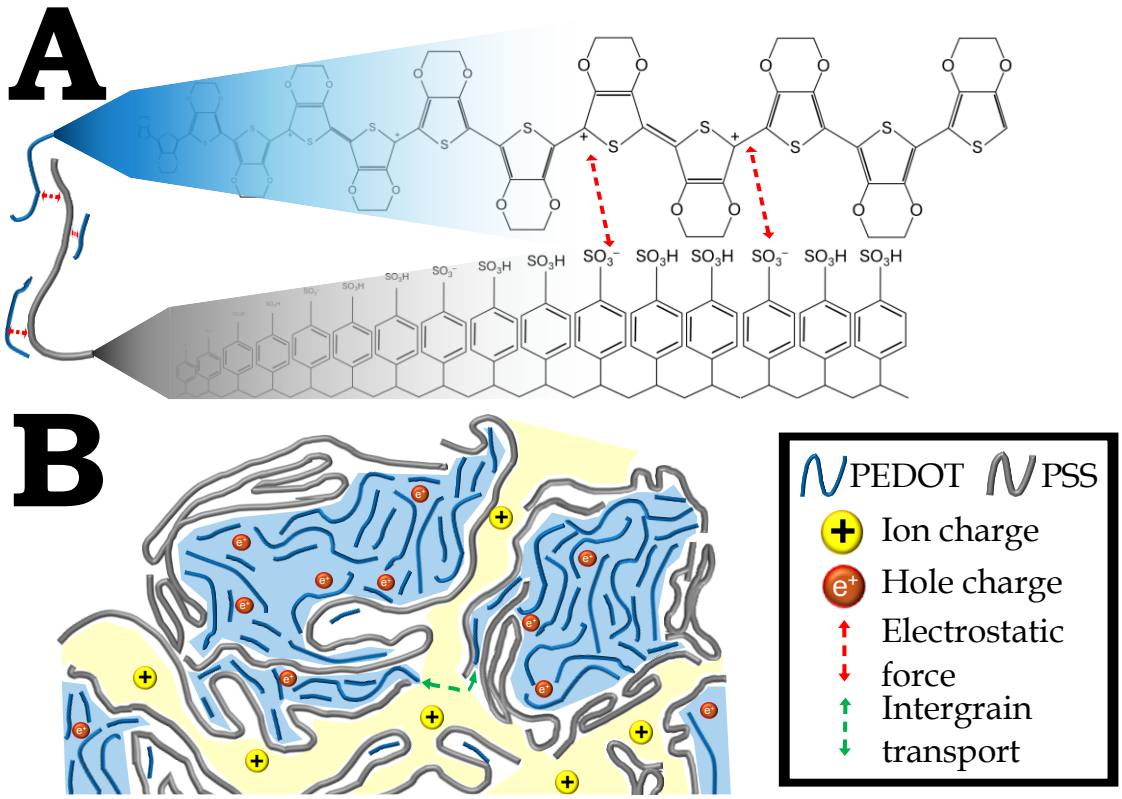

Figure 1-2. **A)** Chain polymers PEDOT and PSS and their interactions. **B)** PEDOT:PSS in an electrolytic solution showcasing the ion conductivity region (shaded in yellow) and hole conductivity region (shaded in blue).

PEDOT:PSS is an organic mixed ionic-electronic conductor that has advantages over metallic interfaces that are solely electronic and rely on faradaic reactions as their working mechanism.

1.4 Research objectives

The general objective of this thesis is to answer the following question: **How can PEDOT:PSS be used for the development of neuronal cultures?**

Specific objectives:

- To understand the electrochemical mechanisms that make PEDOT:PSS such a coveted material.
- To validate PEDOT:PSS as a neuronal interface with biocompatibility assays, the recording of action potentials, and stimulation of neuronal cells.
- To establish a differentiation and maturation protocol of neuronal cells using PEDOT:PSS substrates.

1.5 Thesis Outline

This thesis is organized into 6 chapters. Chapter 1 has so far briefly introduced neurons and their electrophysiology, as well as some illnesses and their impact in society. Technologies that allow for the study of neurons and their diseases are also discussed. Lastly, the organic bioelectronic material PEDOT:PSS is presented as an interface between live tissue and hard electronics and its working mechanism.

In Chapter 2, the literature review establishes the fundamentals of microelectrode array theory and the electrode-neuron interface. Next, state-of-the-art PEDOT:PSS-based electrodes are reviewed according to a defined query to explore the progress and trends in the field. Lastly, additives to PEDOT:PSS solutions

and deposition techniques are compared and discussed, specifically how the working mechanism for enhancing conductivity work in each publication found.
The polymer PEDOT:PSS is put to the test with neuronal cell culture and acid treatments in Chapter 3. This is to confirm in one part the biocompatibility of the material that will serve for later and exploring a straightforward post-processing method of incrementing the conductivity.
Chapter 4 showcases *in vitro* recordings of cortical neurons made with an in-house MEA using the aforementioned PEDOT:PSS. Signal acquisition and post-processing are presented and predominantly discussed, with the action potential waveforms and signal-to-noise ratio shown and described. The chapter continues with strategies to improve the current work to obtain better signals from the extracted data.
The thesis' Chapter 5 then sets to go further in the neuronal characterization by establishing a protocol for differentiation of motor neurons. The chapter describes exhaustively the materials and methods to achieve not only differentiation, but also other critical goals of the motor neuron culture. The results of the protocol consist of morphological changes, biomarker immunostaining, and calcium imaging. Lastly, it is discussed how to further improve the protocol and set future directions.
Finally, chapter 6 brings a summary of the findings in this work, addresses the limitations present while also discussing the outlook of the project.

2 Literature Review

2.1 Literature review introduction

Neural electrophysiology is the direct measure of the electrical properties and signal mechanisms of neurons or their direct stimulation [29]. Moreover, studying neural electrophysiology can mean studying how a single ion channel in the neuronal membrane works or relating brain waves to psychological phenomena. As such, this area of research pushes the boundaries of understanding the inner workings of the healthy or diseased brain, arguably the most important and undoubtedly the most enigmatic organ. Additionally, neurological disorders are the second most common cause death and the leading cause of disability, which will further burden public health services and the quality of life of the general population as it ages [30]. Due to the impact in medicine and public health this field has, it is of great interest to improve the technologies that allow us to sense and interact with neural tissue. One of these is the use of microelectrode arrays, a series of microscale electrodes with high spatial resolution, that are capable of recording neuronal activity and stimulating the neurons to induce a desired state. Speaking of neurons, they can be studied with *in vitro* models, ex vivo tissue slices, or implantable in vivo brain regions.

This literature review will aim to answer the research question ": **How does PEDOT:PSS improve the electrochemical performance of neural electrodes compared to traditional metal electrodes?**" by first introducing fundamental background information of the state of the art, followed the literature retrieval of the state-of-the-art (methodology), the state-of-the-art and the working mechanisms behind each document provided, a discussion of the findings with recommendations for the future, and the concluding remarks.

2.2 Background Information

2.2.1 Microelectrode array

Microelectrode arrays, shortened to MEAs, are a set of electrodes that have dimensions measured in microns (10^{-6}). Electrodes can be modelled with simple electric components such as capacitors and resistors, whose values depend on the material and geometric properties of the electrodes themselves, to create a 'Randles equivalent circuit'. **Figure 2-1** [31], [32] shows a simple example of an electrode in an electrolyte solution with its equivalent circuit.

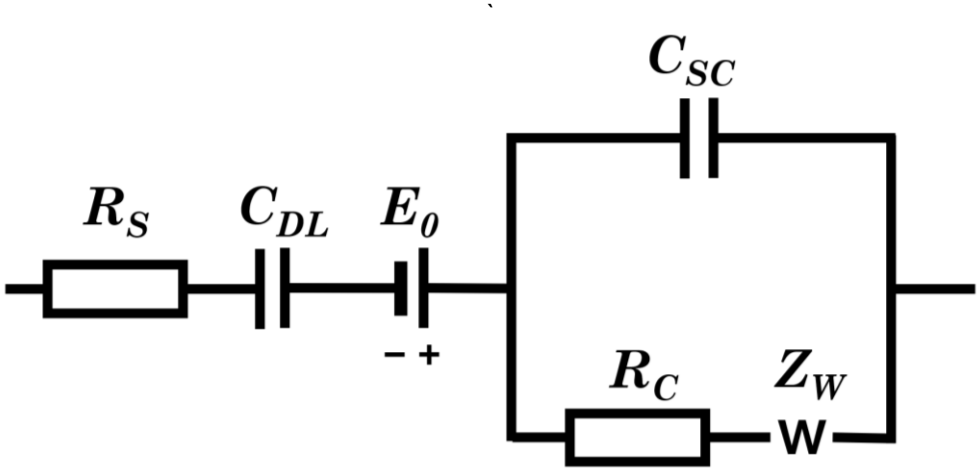

Figure 2-1. Randles equivalent circuit for an electrochemical half-cell electrode [3], [4].

In the figure above, R_S represents the solution resistance of the electrolyte (e.g. phosphate buffer saline, PBS) in bulk and is independent of the frequency of the signal. C_{DL} represents the double-layer capacitance (or Helmholtz capacitance), which arises from two layers at the electrode-electrolyte interface: (1) a rigid

inner layer of solvated ions and oriented water dipoles, and (2) a diffuse outer layer where ionic charge density decays exponentially with distance from the electrode surface [33]. The magnitude of the first layer decreases linearly with distance, while the second layer decreases exponentially; both are accounted for in C_{DL} and act as a frequency dependent component. E_0 is defined by the electrochemical potential difference between the electrode and electrolyte at equilibrium, the half-cell potential, relative to an Ag/AgCl electrode reference. In the example above, the potential is oriented for a recording electrode. C_{SC} represents the capacitance of the charge space, specifically to account for porosity of the electrode material and the overall capacitance of the electrode itself. R_C is the charge transfer resistance, or the resistance for electrons to transfer across the electrode-electrolyte interface during redox reactions. Finally, Z_W is the Warburg impedance and describes the diffusion impedance of ionic mass transport. It contributes heavily at lower frequencies, where the slower ion diffusion becomes rate-limiting. Naturally, the material of the electrode influences all of these components and must be compatible for cell culture and microfabrication techniques, so great consideration must be paid when choosing the material for the MEA.

While **Figure 2-1** is an example of only one electrode, MEAs consist of multiple electrodes (usually in the dozens) and have other specifications that are worth discussing. Firstly, electrode size (effective surface area, ESA) critically impacts MEA performance: larger electrodes exhibit lower impedance (Warburg, charge transfer, and solution resistance), higher capacitance (double-layer and charge space), and improved signal-to-noise ratio (SNR) compared to smaller electrodes. However, as one goes larger one also loses resolution of recording/stimulation, an important aspect of MEAs that is also affected by the interelectrode distances. This interelectrode distance, or pitch, dictates spatial resolution and is heavily dependent on the application of the device: smaller pitches enable single-unit recordings but sacrifice area coverage and increase electrical crosstalk, while larger pitches are better suited for local field potentials (LFPs) reflecting network-level activity. Finally, the thickness of the electrodes is also a parameter that affects the performance of the MEAs, particularly if the material chosen has a significant volumetric capacitance, but also the paths of the electrodes themselves. For the latter, this is related to the resistance as defined by $R = \frac{\rho l}{A}$, where ρ is the intrinsic resistivity of the material, l is the length of the path, and A is the cross-sectional area (thickness x width, which is harder to modify due to the limited space available). In summary, an MEA is a device for neural interfaces that can have a variety of applications depending on the electrode material and size, the pitch length, and the dimensions of the MEA itself.

2.2.2 Electrode-neuron interface

Ever since the first patch-clamp fabricated by Hodgkin and Huxley [34], has the scientific community begun to study neurology at the cellular level and the interface between technology and neural biology. This interface fundamentally relies on the translation of neurophysiological phenomena into measurable signals. In an electrolyte, the flow of ionic currents produced by an action potential traveling through the cell is converted into measurable electrical signals at the electrode-neuron interface through electrochemical interactions. This interface is governed by the electrochemical properties of the electrodes and the surrounding medium, which can be represented by the equivalent circuit (an example is seen on **Figure 2-2**).

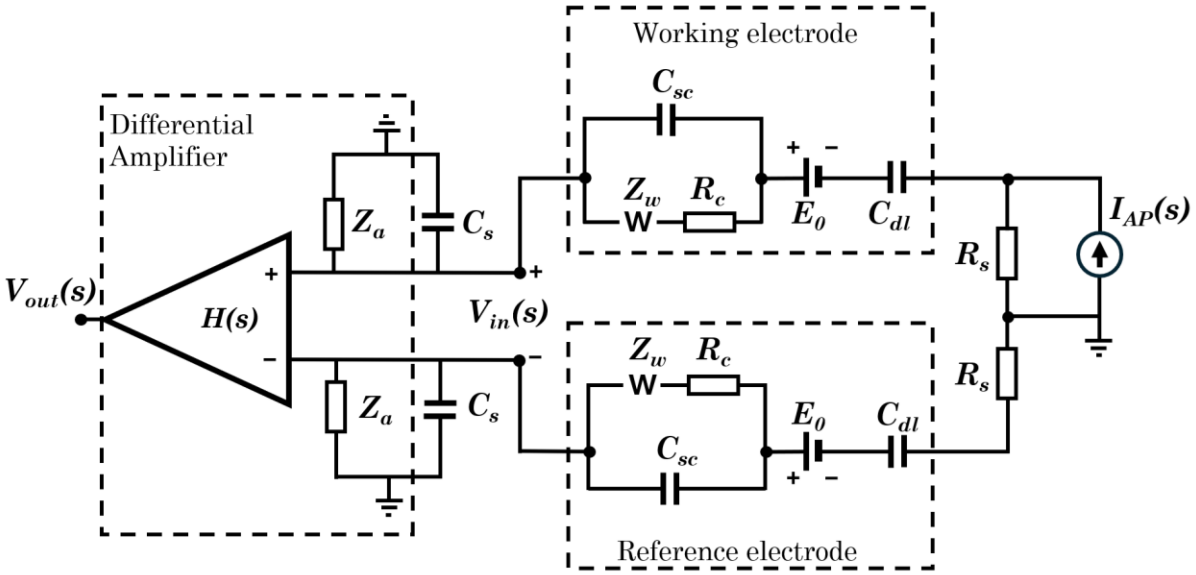

Figure 2-2. Randles equivalent circuit for an electrochemical cell for recording neural activity [3], [4], [5].

The equivalent circuit above contains two electrodes, further described in **Figure 2-1**, and a differential amplifier for the output voltage, $V_{out}(s)$, of the current generated by the neuronal action potential, $I_{AP}(s)$. The amplifier has its own impedance, Z_a, that should ideally be significantly high, so the baseline noise has low amplitudes. The shunt capacitance, C_s, is a parasitic capacitance between the electrode and the amplifier input terminal that arises from the amplifier itself, and the paths leading into it and can act as a low-pass filter. Finally, the transfer function $H(s)$ of the amplifier depends on the electrode impedances (which affect the amplifier input voltage $V_{in}(s)$) and the frequency spectrum of the neural signal. If we imagine a bridge connecting electronic engineering and neuronal biology, one can set the circuit presented on **Figure 2-2** as closer to the former, which is a limitation of this simple circuit. Nevertheless, this electronic representation helps the field better understand the electrophysiological processes found in neurons but also the technical limitations the devices have, providing a springboard to reach novel solutions.

2.2.3 Electrochemical characterization

Assessing the performance of electrodes usually consists of their electrochemical properties being probed. In this review, the most commonly used technique is the Electrochemical Impedance Spectroscopy, referred to as EIS, and it analyzes the response of an electrochemical system to a sinusoidal input (either voltage or current) applied over a wide range of frequencies [35]. It provides insight into the kinetics of the electrode charge-transfer reactions across timescales, assuming a linear, time-invariant system response. For this characterization, two to four electrodes are introduced in an electrolyte solution forming the electrochemical cell (see **Figure 2-1A**), and a well-defined input is applied that can be linearly related to the output signal. The magnitude and phase difference between input and output signals are recorded at each frequency. Usually, results from low frequencies (<1 Hz) explain slow processes such as mass diffusion and adsorption/desorption effects, while high frequencies (>100 kHz) are related to fast time constants such as electrolyte resistance and double-layer charging/discharging. However, slow processes are difficult to maintain precisely because they are slow, as long stabilization times (seconds to minutes) risk system drift. Conversely, high frequencies are susceptible to parasitic inductances and capacitances from the cables and connections that make up the electrochemical cell. Finally, the phase shifts indicate whether the response is dominated by resistive or capacitive behavior, with the former ideally representing no shift (0°) and the latter presenting a shift ideally at (-90°) in respect to the input signal wave. These results are seen in a bode plot for both the magnitude of the impedance and the phase shift itself (**Figure 2-3B**).

In addition to EIS, cyclic voltammetry (CV) is also used extensively to assess the performance of electrodes, more specifically for stimulation purposes. CVs are used to study redox processes, with a forward scan focusing on the reduction effects and a backward scan for the oxidation [36]. It shares many similarities with

the EIS, with practically the same setup and a well-defined input signal, however, there is a key difference: instead of sampling across frequencies, the CV samples across a voltage window several times (hence cyclic) at a specific voltage scan rate. This scan rate, measured typically in mV/s or V/s, affects the response of the system, with faster rates resulting in larger current peaks due to reduced diffusion time of the electrolyte to the electrode surface. The voltage window is also very important, as it determines the redox reactions that can be observed. If it is too narrow some processes may not be detected but if it is too wide then irreversible reactions may occur. For this literature review, the capacitance of the electrodes is the most relevant aspect as it is related to the Charge Storage Capacity (CSC), which is the charge stored in the electrical double layer at the electrode interface [37]. In a CV, the CSC relates to the area under the curve of the voltammogram divided by the scan rate, normalized to the electrode surface area [38]. Such an example can be seen in **Figure 2-3C**. Finally, another relevant parameter for stimulation electrodes is the Charge Injection Limit (CIL), which is found by using voltage transient measurements (**Figure 2-3D**). To calculate the CIL of the electrodes, one needs to find the access voltage, which is the instantaneous voltage that generates when a current is applied or removed to the electrode, represented as V_a [39]. The maximum cathodic or anodic voltage, E_{mc}/E_{ma}, is defined when the transient voltage begins to decay asymptotically without any active electrode shortening. The CIL is found by multiplying the current by the pulse width when E_{mc}/E_{ma} reaches the reduction potential for water divided by the electrode area. This helps establish the limits at which the electrode can safely deliver charge without corroding itself, creating volatile materials in the electrolyte, and avoid damaging cells. Lastly, another important figure of merit for the characterization of MEAs is the performance of assessment through measuring the signal-to-noise ratio, SNR. For this measurement, the electrode needs to record baseline measurements for the background noise and retrieve its root mean square. This noise is baseline fluctuations caused by the thermal noise in the system. A well-defined signal can be introduced in the system to calculate the SNR by measuring the root mean square of the peak signal.

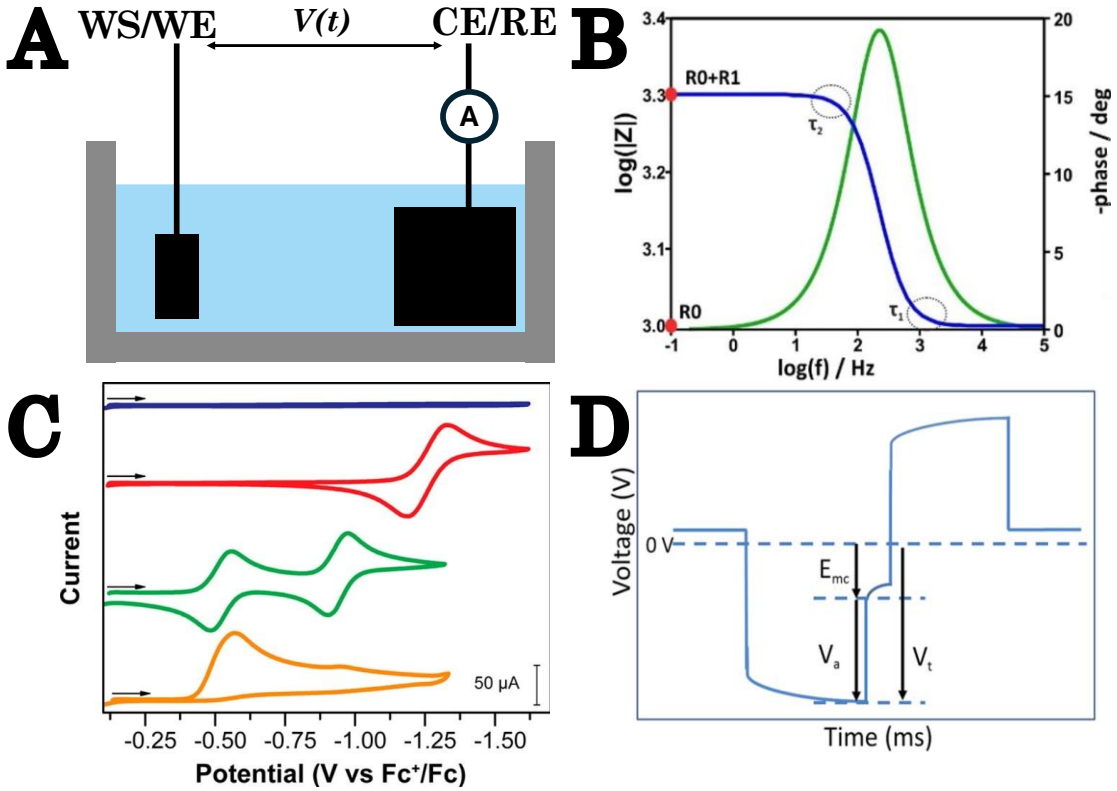

Figure 2-3. **A)** 2-electrode 2-terminal electrochemical cell with one electrode for the working electrode (WE) and working sense (WS) and another electrode for the counter (CE) and reference electrode (RE) [6]. **B)** Bode plot for an ideal parallel RC circuit in series with a resistor *[35]*. **C)** Voltammograms of different electrode materials at different gas conditions *[36]*. **D)** Schematic of biphasic voltage transient potential with the access voltage, V_a, maximum cathodic voltage, E_{mc}, and the total voltage across the cathodic phase, V_t *[39]*.

Figure 2-3 provides a schematic of an electrochemical cell and representative diagrams of EIS and CV analyses, with the bode and the I/V plots. Additionally, the equivalent circuit model of the electrode can give complementary insight into the results of both the EIS and the CV. By fitting the data into different EIS parameters, such as the double-layer capacitance or the charge transfer resistance, a detailed understanding of the electrochemical processes can be gathered. Also, the equivalent circuit model can reveal deviations from ideal behavior, such as heterogenous surface reactions or mixed kinetic-diffusion control, which may not be immediately apparent from CV alone. Moreover, the results of the voltage transient measurements are directly tied to the capacitive performance of the electrodes for stimulation. In conclusion, electrochemical characterization provides the most important information for safe and effective neural interfaces.

2.2.4 PEDOT:PSS

Poly(3,4-ethylenedioxythiophene):poly(styrene sulfonate), hereinafter referred to solely as PEDOT:PSS, is a conductive polymer compound used for its relatively high electrical conductivity, excellent optical properties, and film-forming properties [40]. The polymer PEDOT has been gaining attention due to its conductive properties since its discovery [41], [42], [43]. PEDOT doped with specific anions has a wide range of conductivity of 1-300 S/cm^2 [44]. However, pristine PEDOT is notorious for its low solubility, which is solved by the addition of PSS, a polymer containing counterions to stabilize PEDOT in an aqueous dispersion for thin film processing. The addition of PSS interferes with the intrinsic inter-conductivity of the PEDOT chains, as PSS is an electric insulator. PEDOT:PSS forms micelles with PEDOT cores and PSS shells, increasing the π-π stacking distance of other PEDOT cores [40], [45]. Dopants are usually added to increase conductivity of PEDOT:PSS, as is seen in this literature review, by removing some of the PSS to increase the PEDOT inter-chain entanglements and increase conductivity [46].

Furthermore, unlike metallic electrodes, PEDOT:PSS offers deeper electrolyte penetration into the polymer via storing charge in both double-layer capacitance and Faradaic reactions. This is achieved thanks to the volumetric capacitance of PEDOT:PSS, a result of the co-polymer heterogenous morphology allowing for a two-phase system that allow for percolation of the electrolyte [47]. In fact, PEDOT:PSS is also a conductor of both ions and electrons (actually 'holes') in PSS-rich and PEDOT-rich regions respectively and the double-layer further extends to the interface between these two regions.

Critically, PEDOT:PSS can be modified to have a stiffness orders of magnitude lower than metallic electrodes (~2 MPa with hydrogels against gold's ~69 GPa) [48], [49], [50], which is highly advantageous when used as an interface between electronics and biology. These properties are useful to assess the brain and neuronal tissue, grey matter stiffness in the range of 0.2-7 kPa [51], and the fact the electrical language of the body is ionic (e.g. Ca^{2+}, K^+, Na^+, Cl^-). As such, PEDOT:PSS's ability to support both capacitive (double-layer) and Faradaic charge storage, coupled with its high volumetric capacitance, enhances electrophysiological signal transduction and stimulation efficiency at the electrode-cell interface. Making PEDOT:PSS an unparalleled material candidate to bridge the gap between rigid electronics and soft biological tissue.

2.3 Neuron

Neurons are the functional unit of the nervous system, capable of producing action potential and forming highly sophisticated networks between themselves and the rest of the organs and tissues. It is difficult to grasp the complexity of the brain: ~100,000,000,000 (10^{11}) neurons, each with thousands of connections to other neurons or target cells [1]. Even mapping 1 mm^3 of the brain is a huge achievement that still needed help of artificial intelligence to reconstruct the 57,000 neurons and their 150 million connections [52]. Still, studying the brain at a cellular level, neurons, is no simple task and can produce groundbreaking knowledge. A neuron typically consists of dendrites (input regions), the soma (cell body), and the axon (output region) with pre-synaptic branches at its terminal. Neurons can span 1 meter from dendrite to axon terminal and are lined with voltage-gated ion specific channels on the cell membrane that maintain a resting voltage of around -70 mV. Neuronal electrical activity begins when synaptic inputs depolarize the membrane to the threshold potential, around -50 mV. Neurotransmitters need to trigger enough ion channel openings that generate potential that can spatially or temporarily add up at the axon hillock above the excitation threshold. Then, an

action potential propagates along the axon towards the terminal. The action potential moves much faster thanks to the presence of myelin sheaths by glial cells that induce saltatory conduction [53]. Finally, the action potential ends at the axon terminal that results in the release of neurotransmitters, beginning the cycle again. Evidently, neurons typically communicate with each other with neurotransmitters instead of strictly electrically, though, this can happen thanks to gap junctions. It is important to note that neurons can be either excitatory or inhibitory and react to specific neurotransmitters. Moreover, the action potential works with the flow of ***ions*** and not electrons like in conventional semiconductors, and the cell then repolarizes itself to its resting state after firing, with a refractory period taking place that prevents the neuron from firing again. Due to their electrical activity and sensitivity, there is a great interest in coupling neurons with electronic devices to further understand the nervous system, both in health and disease.

2.4 State-of-the-Art

2.4.1 Methodology

A literature search was conducted in the Scopus database to investigate the state of the art of PEDOT:PSS electrodes for neurophysiological applications. **Figure 2-4** shows a schematic of the query used for the literature search. This query resulted in 62 different articles, which were further assessed for revelance and availability, finally giving 16 works for which this document is based on. The criteria of relevance were established as follows: 1) It must contain PEDOT:PSS, 2) the PEDOT:PSS must be involved in the fabrication of microelectrodes, and 3) the electrophysiology of neuronal cells must be assessed. Several keywords were filtered to narrow the research and articles to PEDOT:PSS MEAs for in vitro neuronal applications. Firstly, the focus was on original work in the last ten years so to not be biased by an inclusion of similar literature reviews the following keywords were filtered: (“Review” OR “Overview” OR “State-of-the-art” OR (“State” AND “of” AND “the” AND “art”). Then, more keywords were used to narrow the in vitro nature of this literature review: (“in-vivo” OR (“in” AND “vivo”) OR “Electroencephalography” OR “EEG” OR “Electrocorticography” OR “ECoG”). Next, it was necessary to exclude non-neuronal cultures: (“Bacter*” OR “Cardio*” OR “Hepat*” OR “Myo*”). Finally, additional keywords were included due to the high volume of papers that were not related to the topic: (“Hormone” OR “Sjögren” OR “Dopamine”).

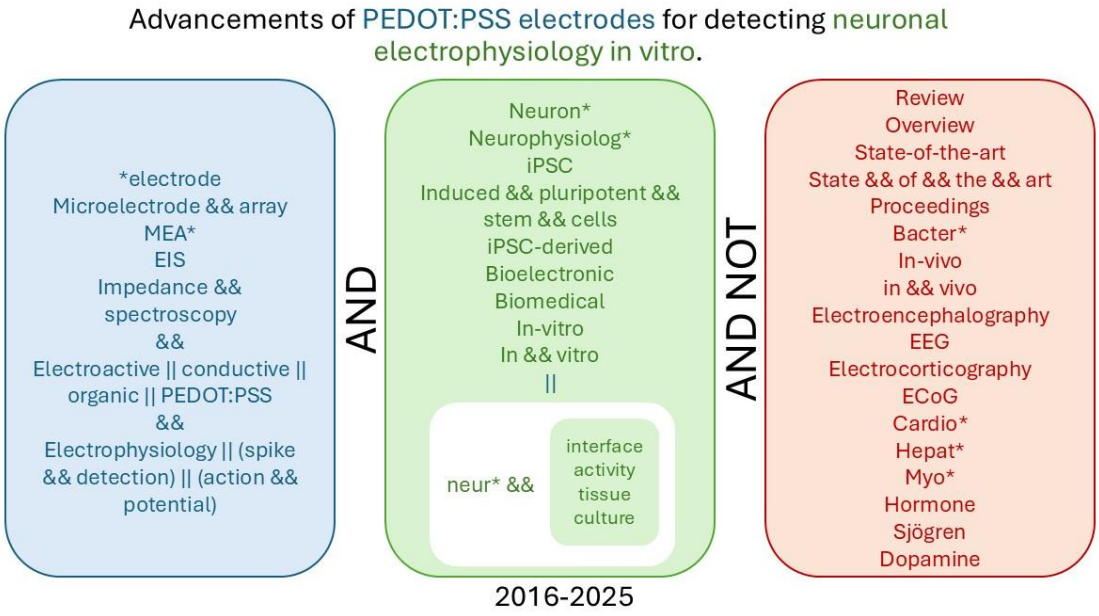

Figure 2-4. Literature review query and scope definitions.

2.4.2 Novel PEDOT:PSS-based electrodes and their application

Table 2-1- Chronological state-of-the-art of PEDOT:PSS-based MEAs, with PEDOT:PSS source, additives (ethylene glycol, *EG*, dodecyl benzene sulfonic acid, *DBSA*, 3-glycidyloxy-propyl-trimethoxysilane, *GOPS*, and the PEDOT:PSS deposition method.

Authors (date published)	**PEDOT:PSS**	**PEDOT:PSS additives** (not study's focus)	**Electrode material**	**PEDOT:PSS deposition**	**Source**
Koutsouras, D.A., Pa,s J., et al. (2017, 2018)	Clevios PH 1000 (Heraeus Holding)	5 wt.% EG 0.1 wt.% DBSA 1 wt.% GOPS	PEDOT:PSS/Au	Spin-coating (350 nm)	[54], [55]
Wang, K., et al (2018)	EDOT (0.1 wt.%), PSS (0.2 wt.%), PEDOT:PSS 1.3-1.7 wt.% (Yacoo Corp)	-	PEDOT:PSS/PCNT-Alg/CdNi PEDOT:PSS/CNT-Alg/CdNi PCNT-Alg/CdNi	Potentiostatic electrodeposition at 1 V for 100-1200s	[56]
Asgarifar, S., et al (2018)	(n.a.)	EG (immersion after annealing)	PEDOT:PSS/Au	Inkjet (Fujifilm DMP 2831)	[57]
Carli, S., et al (2018)	EDOT (0.05 M), Na-PSS (0.1M)	-	ox-SWCNHs/PEDOT:PSS/Au ox-MWCNTs/PEDOT:PSS/Au	Potentiodynamic electrodeposition at 0.1 V/s in 0-0.95 V for 100 cycles	[58]
Tomaskovic-Crook, E., et al. (2019)	EDOT (0.01 M), Na-PSS (0.1 M), PEDOT:PSS 1.3 wt.% (n.a.)	1.5 vol.% GOPS 25 vol.% DMSO	PEDOT:PSS/Au	Potentiostatic electrodeposition at 0.9 V	[59]
Aqrawe, Z., et al (2019)	EDOT (0.01 M), Na-PSS (0.1 M) (Sigma)	-	PEDOT:PSS/Au	Galvanostatic electrodeposition 2mA/cm^2, total: 318 mC/cm^2	[60]
He, E., et al (2020)	EDOT (0.02 M), Na-PSS (0.1 M) (Aladdin, HEROCHEM)	-	COOH-MWCNTs-PEDOT:PSS/Au PEDOT:PSS/Au	Potentiodynamic electrodeposition at 0.1 V/s in 0-0.95 V for 20 cycles	[61]
He, E., et al (2022)	EDOT (0.02 M), Na-PSS (0.1 M) (Aladdin, HEROCHEM)	-	rGO-PEDOT:PSS/Au CNTs-PEDOT:PSS/Au	Potentiodynamic electrodeposition at 0.1 V/s in 0-0.95 V for 10 cycles	[62]
Li, T.L., et al (2022)	Clevios PH 1000	Ionic Liquid	PEDOT:PSS-IL/SEBS/Au	Spin-coating	[63]
Donaldson, P.D, & Swisher, S.L. (2022)	PEDOT:PSS ink (Orgacon IJ-1005)	-	PEDOT:PSS	Inkjet (Fujifilm DMP 11610)	[64]
Lunghi, A., et al (2022)	EDOT (0.01 M), Na-PSS (0.7 wt.%)	-	PEDOT:PSS/Au	Potentiodynamic electrodeposition in 0-1 V for 15 cycles.	[65]
Xu, S., et al (2022)	EDOT (0.02 M), PSS (0.1 M) (Aladdin, HEROCHEM)	-	cGO-PEDOT:PSS/Au CNT-PEDOT:PSS/Au	Potentiodynamic electrodeposition at 0.1 V/s in 0-0.95 V for 15 cycles	[66]
Vajrala, V.S., et al (2023)	EDOT (0.01 M), Na-PSS (0.1% w/v) (Sigma)	0.5 M H_2SO_4	PEDOT:PSS/Au	Potentiodynamic electrodeposition at 0.01 V.s in -0.7 to 0.9 V for 1 cycle	[67]
Lu, Z., et al (2023)	Clevios PH500 (Heraeus Holding)	5 vol.% EG 0.26 vol.% DBSA 1 vol.% GOPS	SLB/PEDOT:PSS/Au	Spin-coating (3000 rpm, 45s)	[68]
Dijk, G., et al (2023)	Clevios PH 1000 (Heraeus Holding)	EG, DBSA, GOPS	PEDOT:PSS/Pt	Spin-coating (550 nm)	[69]

Table 1-2- Electrode performance of chronological state-of-the-art of PEDOT:PSS-based MEAs, with Geometric Surface Area, *GSA*, Diameter, *D*, Outer Diameter, *O.D*, Inner Diameter, *I*.D, height, *h*, impedance at 1 kHz , charge storage capacity, *CSC*, and charge injection limit, *CIL*.

Authors (date published)	**GSA** (μm^2)	$\|Z\|_{1\,kHz}$ (kΩ)	$\|Z\|_{1\,kHz}$ **-normalized to area** ($\Omega \cdot cm^2$)	**CSC** (mC/cm^2) [Scan rate]	**CIL** (mC/cm^2)	**Biological Use**	**Source**
Koutsouras, D.A., Pa,s J., et al. (2017, 2018)	144 (12x12 μm)	38.5±2.4	0.055±0.0035	-	-	Neural activity from hippocampal neuron cell cultures under different drugs for 3-6 weeks.	[54], [55]
Wang, K., et al (2018)	1962.5 (D≈50 μm)	~200 - ~300	~3.925 - ~5.888	1.2 0.5 - [0.5 V/s]	- - -	Culture of SH-SY5Y cells for biocompatibility and growth. Rat brain implant for electrophysiological measurements.	[56]
Asgarifar, S., et al (2018)	2000000	-	~200000	-	-	Record signals from rat glioma cells cultures.	[57]
Carli, S., et al (2018)	7850 (D=100 μm)	3.8±0.4 3.5±0.4	0.298±0.031 0.275±0.031	101±18.6 43±15.9	11.6 8.7	Rat fibroblasts for biocompatibility. In vivo rat brain electrophysiological measurements.	[58]
Tomaskovic-Crook, E., et al. (2019)	3670 (D; h≈14; 80 μm) 314 (D=20 μm)	~300 ~400	~11.01 ~14.68	127±5.6 12.1±0.9 [0.1 V/s]	11.41±0.46 2.31±0.08	Culture and stimulation of neural stem cells in hydrogel scaffolds for neural differentiation.	[59]
Aqrawe, Z., et al (2019)	314 (D=20 μm)	~40	~0.126	-	-	Culture of hippocampal cells for optical and electrical electrophysiological characterization.	[60]
He, E., et al (2020)	78.5 (D=10 μm)	36.1±3.07 68.9±4.39	0.028±0.002 0.054±0.003	-	-	Rat hippocampal tissue for the characterization of the kinetics of epilepsy.	[61]
He, E., et al (2022)	177 (D=15 μm)	14.7±2.49 28.7±1.77	0.027±0.004 0.051±0.003	-	-	Long term differentiation of stem cells to mature dopaminergic neurons. Electrophysiological and dopamine sensing characterization.	[62]
Li, T.L., et al (2022)	1962 (D=50 μm)	20.1±36.1	0.394±0.708	-	-	Stimulation of human cortical organoids for long term culture.	[63]
Donaldson, P.D, & Swisher, S.L. (2022)	~8000 (O.D=550 μm) ~8000 (O.D=400 μm) ~8000 (O.D=300 μm)	15.8 15.2 19.8	1.264 1.216 1.584	21 12 6 [1 V/s]	-	-	[64]
Lunghi, A., et al (2022)	127.1 (D;h= 8.3;2.8 μm) 97.54 (D;h = 7.1;2.6μm)	0.141 0.139	0.00018 0.00014	-	-	Biocompatibility, differentiation, and neurite orientation of SH-SY5Y cells.	[65]

Xu, S., et al (2022)	706.5 (D=30 µm)	7.26±0.26 16.84±0.7	0.051±0.002 0.119±0.005	7.53±0.34 4.8±0.2 [0.05 V/s]	3.11±0.25 1.93±0.23	Long term culture of hippocampal neurons for electrophysiological recordings, stimulation, and neural learning.	[66]
Vajrala, V.S., et al (2023)	1400 (I.D=100 µm) 445 (I.D=40 µm) 1325 (D=40 µm)	3.7±0.42 ~9 ~9	0.052±0.006 ~0.041 ~0.119	~28 ~27 ~26 [0.2 V/s]	15±2 ~14 ~6	Biocompatibility and electrophysiological characterization of SH-SY5Y and hippocampal cells	[67]
Lu, Z., et al (2023)	159000 (D=450 µm)	-	35.11±2.57	-	-	Cell membrane characterization of rat cortical cells.	[68]
Dijk, G., et al (2023)	7850 (D=100 µm)	~10	~0.786	-	-	Biocompatibility and stimulation of rat cortical tissue.	[69]

Beginning with the simplest devices found: planar, metal-PEDOT:PSS electrodes; researchers characterized neuronal activity using both electrical and optical techniques with a PEDOT:PSS/Au MEA [60]. 14 electrodes of 20 μm diameter were shown to have a drop in impedance of two orders of magnitude when compared to Au electrodes. Primary hippocampal neurons were cultured on the MEA for 21 days and had good growth and density. The MEA was able to simultaneously record an action potential without interfering with optical characterization of said action potentials through voltage sensitive dyes, though it was worth noting that more action potentials were recorded electrically than optically, shedding light on the sensitivity of the electrode. The authors discussed the results of SNR characterization, where they found that their electrodes were three-fold more effective in picking up action potentials than Au as opposed to eight-fold that was previously calculated, offering the location of the neuron as a possible explanation.

16 planar, 100 μm in diameter PEDOT:PSS/Pt electrodes were characterized for their stimulation performance for safe neural interfaces [69]. Bare Pt electrodes were used as a reference group and they were found to experience corrosion and delamination when the charge density reached 191 mC/cm^2, while no such phenomenon occurred with the PEDOT:PSS/Pt electrodes even at 255 mC/cm^2. It was also established that the PEDOT:PSS electrode impedance was 2 orders of magnitude lower than the bare Pt electrodes at 1 kHz. Rat cortical tissues were cultured for up to 9 days on the electrodes and stimulated for 2 continuous hours for three consecutive days and it was found that the cells near the bare Pt electrodes experienced almost total cell death, though the cell viability of the cultures were not statistically significant between both MEAs.

Veering into 3D interfaces, but still with planar electrodes, a study assessed the neural networks of neurospheres (3D cell aggregates) with a PEDOT:PSS-coated MEA [54], [55]. The array consisted of 64 Au electrodes with parylene C and the PEDOT:PSS was coated via spin-coating and then peel-off technique. This work introduced laser-patterned PEGDA structures to spatially control neurosphere growth. The researchers investigated the role of cell seeding density (low and high) via the yield of recording electrodes and the quality of the data. When primary rat cortical cells formed neurospheres, single-unit recordings improved dramatically, capturing activity from both superficial and deep layers. However, this came at a trade-off, higher cell densities increased spike detection rates, but they compromised signal separation quality.

These last two examples, in contrast to the first one, used additives in the PEDOT:PSS solution for the purpose of increasing the conductivity and wettability of the conductive polymer, as the deposition method used spin-coating instead of electrochemical deposition. The additives are the following:

- **Ethylene glycol**: EG has been used as a chemical treatment of PEDOT:PSS to improve its conductivity and is actually one of the preferred co-solvents due to its effectivity [70]. It has been found that the addition of this solvent can obtain a conductivity as high as 735 S/cm [71]. Therefore, this additive is an attractive material for electro-neurophysiological recordings.
- **Dodecyl benzene sulfuric acid**: DBSA, just like EG, is a popular chemical treatment for PEDOT:PSS for increases in conductivity, however, it also increases the stability of the solution and prevents particle deposition of PEDOT [72].
- **3-glycidyloxy-propyl-trimethoxysilane**: Finally, GOPS is used as a cross-linker and stabilizer of PEDOT:PSS films to prevent delamination and dissolution in an aqueous solution [73]. This is particularly useful for applications involving electrolyte solutions, as is the case in many biological applications, including cell culture, and electrochemical characterization. However, it has also been noted that the addition of this material negatively affects the conductivity of the PEDOT:PSS, creating a trade-off between stability and conductivity.

2.4.3 Carbon Nanomaterial Composites

The integration of carbon nanomaterials with PEDOT:PSS was a popular choice in the extracted literature. The researchers looked to improve impedance, charge injection capacity, and stability of pristine PEDOT:PSS with carbon nanocomposites rather than using additives for the solution or building upon them. The reason for this, most likely, is due to the electrochemical deposition method of PEDOT:PSS, which also helps for the deposition of the carbon derivatives (see **Figure 2-5**). Nevertheless, these composites have demonstrated positive conductive performances.

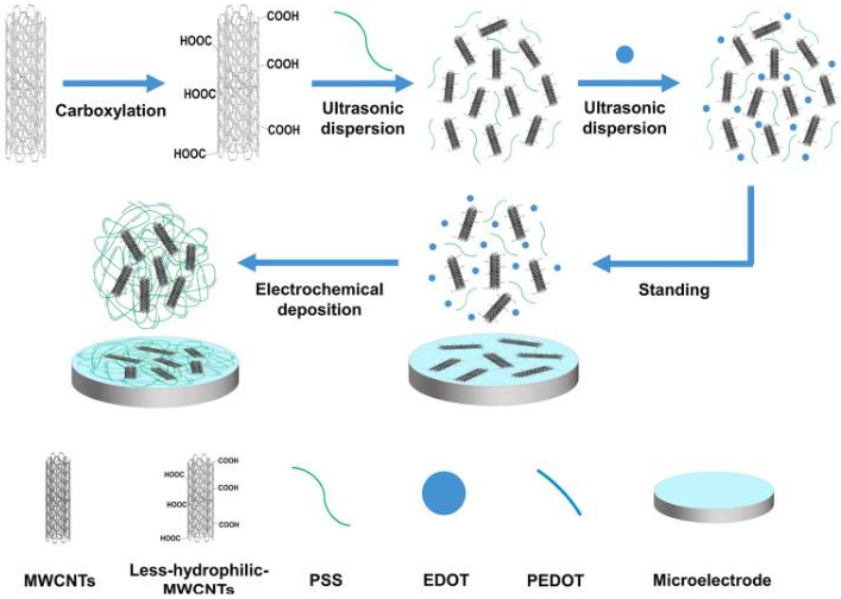

Figure 2-5. Scheme for electrochemical deposition of carboxylated-MWCNTs/PEDOT:PSS onto the Au microelectrodes *[61]*.

This section begins when researchers ambitiously combined PEDOT:PSS with multi-walled carbon nanotubes (MWCNTs) and alginate hydrogels to create an enhanced electrode-neural interface [56]. Unlike conventional planar electrodes that predominantly use Au, this study utilized nickel-cadmium microwires (4-by-4 array of ~50 μm^2), which had PEDOT:PSS electrodeposited. Critically, the coated electrodes were encapsulated with an alginate hydrogel that contained PEDOT:PSS coated MWCNTs (PCNT-Alg), and this hydrogel was even further coated with more PEDOT:PSS. The composite reduced impedance, increased charge storage capacity (CSC), and showed biocompatibility in cell cultures and in vivo rat brain recordings. This demonstrated the benefits of layering PEDOT:PSS for better electrode performance, with CNTs as an additive.

Another study explored oxidized single-walled carbon nanohorns (ox-SWCNHs) as an alternative to MWCNTs on Au/PEDOT:PSS electrodes (16 with 60 µm diameter) [58]. While both carbon composites reduced impedance similarly, ox-SWCNHs had higher CSC and CIL, making them better for stimulation. A biocompatibility assay was performed where ox-SWCNHs had slightly less cell death (non-significant) and neuronal electrophysiology was assessed with rat somatosensory neurons (in vivo). This study highlighted the importance of nanomaterial selection in optimizing electrode performance.

Keeping in line with CNTs, researchers incorporated carboxylated MWCNTs and PEDOT:PSS to a tailor-made MEA for hippocampal slice studies to study epileptic discharges (deposition seen on **Figure 2-5**) [61]. By comparing super-hydrophilic (sh-MWCNTs) and less-hydrophilic (lh-MWCNTs) variants, researchers found the latter offered better impedance reduction (50% lower than PEDOT:PSS alone) due to a higher density, porosity, phase separation, and lower thickness than sh-MWCNTs. Thanks to

the tailored design of the MEA, the spread speed and origin of epileptic discharge were characterized, and it was found that a backward spread is faster than a forward spread and that they are mediated by different receptors.

Researchers introduced reduced graphene oxide (rGO) to PEDOT:PSS on an MEA to both characterize electrophysiology and serve as a biosensor [62]. It halved impedance at 1 kHz compared to CNT-based electrodes and supported long-term (>30 days) neuron cultures.The electrodes not only were able to pick up the action potentials of the neurons, but also the picoampere current responses of oxidized dopamine. The MEA could distinguish between two kinds of spike events and proved that the neuronal cell line investigated had dopaminergic physiological functions.

Lastly, the quest for durable interfaces led to an MEA with carboxylated graphene (cGO) and PEDOT:PSS for hippocampal neurons [66]. The cGO/PEDOT:PSS MEAs were shown to outperform CNT composites in both impedance and electrochemical surface area, supported by CSC and CIL measurements. Furthermore, The electrodes remained stable over extensive testing (100k CV cycles), enabling neuron stimulation and learning experiments due to their high spatio-temporal resolution and electrochemical stability.

2.4.4 Novel fabrication and coating techniques

Naturally, the development of new MEAs goes hand in hand with the progress made in fabrication techniques and coating technology. These two address critical challenges in neural interface design, from electrochemical stability and impedance reduction to 3D integration and multifunctionality. The following papers relate to novel electrode fabrication techniques that do not involve carbon composites.

Planar electrodes

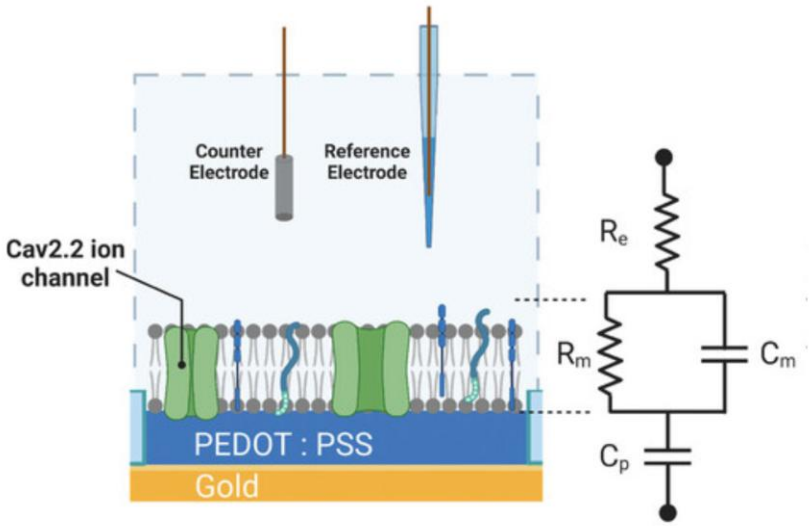

Figure 2-6. Native lipid bilayer on top of PEDOT:PSS/Au electrode in an electrochemical setup with a model circuit. R_e, electrolyte resistance, R_m, membrane resistance, C_m, membrane capacitance, and C_p, PEDOT:PSS capacitance *[68]*.

Additive manufacturing techniques for neural electrodes was explored by researches who inkjet-printed PEDOT:PSS electrodes on glass for glial cell monitoring [57]. Curiously, the PEDOT:PSS electrodes (2 mm² rectangular) were compared to much larger Au electrodes (9 mm² circular), complicating performance assessments. Additionally, the authors did not perform any sort of pre-treatment to the glass substrate and reported that the electrodes faced delamination issues five days after submerging in cell culture medium, an important disadvantage. Moreover, the Au electrodes were coated with Poly-L-Lysine for cell culture but not the PEDOT:PSS, though cells did attach to the substrate. Nevertheless,

the authors showed that the PEDOT:PSS electrodes had a lower 'resistance' and a higher SNR for voltage and current measurements than the Au ones, but also a much lower capacitance in all probed frequencies. The researchers focused on current measurements to assess the membrane depolarization of the cells, which are not electrogenic and cannot produce an action potential.

The most ground-breaking innovation arrived when PEDOT:PSS electrodes were functionalized with native lipid bilayers (SLB) from SH-SY5Y cells (seen on **Figure 2-6**) [68]. Circular and rectangular electrodes of 450 μm in diameter and 200x200 μm in size respectively were created from Au electrodes with spin-coated PEDOT:PSS. The MEA was air plasma treated before the addition of the vesicles produced by the neural cells, effectively forming a layer of cell membrane that includes, critically, voltage-gated ion channels. While impedance matched standard PEDOT:PSS (~1 kΩ), adding stabilizing liposomes for surface adhesion increased it tenfold, a trade-off for accessing ion channel electrophysiology. The authors were able to sense the effects of voltage-gated calcium ion channel inhibitor drugs through electrochemical characterization, with higher doses resulting in higher impedances, though it is worth mentioning that the lipid bilayer had a more substantial effect when it was derived from differentiated SH-SY5Y cells. In all, this is an incredibly innovative paper that pushes what organic electrodes can be.

3D electrodes

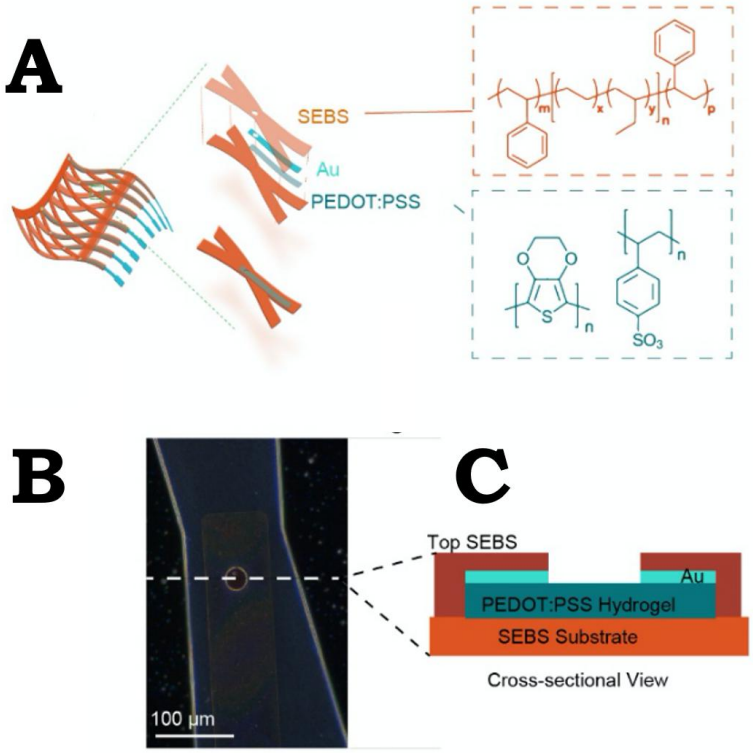

Figure 2-7. **A)** Illustration of the PEDOT:PSS-IL/Au/SEBS mesh. **B)** A micrograph of a single electrode on the mesh. **C)** Cross-sectional view of the electrode *[63]*.

The shift to 3D electrodes began with a familiar fabrication. Inkjet printing was refined in [64] with a refined approach for implantable electrodes. The researchers inkjet-printed PEDOT:PSS ink on an Argon plasma-treated PET sheets with different diameters: 300, 400 and 550 μm, but with the caveat that the electrodes were encapsulated with Parylene C and a contact opening of 100 μm in diameter was put in the center. Critically, the PEDOT:PSS was printed as annular rings to increase thickness

without sacrificing transparency. Intuitively, the largest electrode size exhibited the best capacitance, charge storage, while maintaining a good bending tolerance, addressing earlier delamination concerns plus veering into the three-dimensional (3D) interfaces.

This hollow ring design was further explored for 3D neural network in vitro characterization using PEDOT:PSS-coated Au electrodes [67]. The array consisted of four different electrodes with inner diameters of 40 and 100 µm (surface area 445 and 1400 µm respectively). In the electrochemical characterization, the electrode with the larger surface area had the lowest impedance at 1 kHz, 3.7 kΩ, while the smaller electrode had a similar impedance to a 40 µm diameter planar electrode. The CSC was found to be similar between the electrodes, even with the planar one, at around 30, however, the CIL measurements showed the hollow ring electrodes (15 mC/cm^2) to be 3 times higher than the planar ones. When interfaced with 3D rat embryonic hippocampal cultures, they captured high-resolution burst propagation, demonstrating how tailored 3D geometries could extract more physiologically relevant data from complex neural networks.

The next step consisted of using polydimethylsiloxane (PDMS) micropillars (6 or 8 µm wide) coated with PEDOT:PSS for neural interface applications [65]. The micropillar array consisted of two different diameters of the same height (3 µm) with different pitches (15 or 30 µm). It was found that the at 1 kHz, the impedance level was similar across the 3D electrode types (around 140 Ω) and not that different from flat PEDOT:PSS-Au electrodes (150 Ω); however, for the capacitance measurements, the 8µ-high electrode pillar with the low pitch was found to have the best capacitance in comparison with the rest. SH-SY5Y cultures revealed anisotropic neurite guidance along pillar arrays, showing how 3D topographies could actively direct neural network formation. The authors, however, do not explore the flexibility or even stretchability of their arrays with the culture as logically implied, instead treating it as an MEA with soft materials.

More sophisticated 3D electrodes came when direct-write micropipetting was used to fabricate PEDOT:PSS pillars (80 µm tall, 14 µm wide) on top of Au electrodes [59]. These pillars exhibited remarkable performance: a 10x higher charge storage capacity (127 mC/cm^2), 5x greater charge injection limit (11.4 mC/cm^2) and a lower impedance at 1 kHz compared to planar PEDOT:PSS electrodes. While both PEDOT:PSS electrodes had their impedance increase with time, the planar electrodes presented delamination issues, while the pillars had none. A hydrogel with neural stem cells was deposited onto the MEAs for seven-day culture and stimulation. It was found via immunostaining that unstimulated cells had less mature neuronal tissue as compared to the stimulated ones, though no comparison between planar and pillar electrodes was made.

Finally, researchers developed a breakthrough PEDOT:PSS-based mesh electronics for cortical organoids (shown on **Figure 2-7**) [63]. A solution of PEDOT:PSS and an ionic liquid, 4-(3-butyl-1-imidazolio)-1-butanesulfonic acid triflate (IL), was spin coated on an elastomer poly(styrene-ethylene-butadiene-styrene) (SEBS), and then a layer of Au was deposited through thermal evaporation and encapsulated with another layer of SEBS. The array of 16 electrodes of 50 µm in diameter maintained stable impedance (~20 kΩ at 1 kHz) even under biaxial strain. Most impressively, these meshes supported human cortical organoids for 140+ days, demonstrating biointegration and enabling successful stimulation after 90 days in culture, an achievement for long-term 3D neural interface stability.

2.4.5 Novel PEDOT:PSS-based electrodes working mechanisms

PEDOT:PSS only and metal electrodes

As shown in each study presented in this literature review [54], [55], [57], [59], [60], [65], [67], [69], PEDOT:PSS is commonly interfaced with a metal electrode to enhance the conductivity of the MEA, particularly with gold. This is possible thanks to the low energy barrier between Au's Fermi level (~5.1 eV) and PEDOT's highest occupied molecular orbital (HOMO, ~5 eV) and lowest unoccupied molecular

orbital (LUMO, ~4.4 eV) in the oxidized state (when coupled with PSS) that allows for charge injection of both electrons and holes [74], [75]. As a result, electrons flow from Au into PEDOT with minimal resistive losses, while the PSS phase facilitates ionic percolation, coupling electronic and ionic conduction. Thus, electrons can flow into PEDOT with minimized resistive losses at the interface and effectively increase the volumetric capacitance of the Au electrode. This enhancement not only increases the electrode's volumetric capacitance, but also expands the double-layer interface, improving CSC. Moreover, the redox state of PEDOT can be modulated with electrons from the Au to reduce the PEDOT and create a high charge injection capacity, critical for neural stimulation.

Some authors further expand the volumetric capacitance of their devices with novel geometric designs, though the working principle stays the same [59], [67]. However, 3D pillars can be more complex if they are small enough for the cell to engulf them completely. The effective surface area is greatly increased and the cleft between the cell membrane and the electrode is also reduced, resulting in a better SNR and a modified equivalent circuit to account for the different interfaces [76]. The pillars can even be introduced to a hydrogel containing neuronal cells [59], which help distribute the charges uniformly for stimulation and facilitates ion conductivity for recording. In summary, even extensively used PEDOT:PSS/Metal composite electrodes are versatile enough to give rise to novel designs that can push the performance of MEAs further.

As mentioned earlier, PEDOT:PSS can have additives that increase the conductivity of the polymer when used as a solution. However, to understand the working mechanisms of the additives, it is important to recall what PEDOT:PSS looks like in solution: hydrophobic PEDOT-rich regions with a hydrophilic PSS-rich shell forming micellar structures. The working mechanism of the mentioned additives are explained as follows:

- **Ethylene glycol**: PEDOT chains can be formed by coil-shaped benzoid structures or sheet-like quinoid structures (seen on **Figure 2-8**), with the latter having improved charge mobility [70]. EG has been shown via Raman spectroscopy to change the structure of the PEDOT chains from benzoid to quinoid, thus improving conductivity [70], [77]. Moreover, EG also interacts with the PSS chains through hydrogen bonds and arrange them into a less dense shell-network, producing shorter distances between PEDOT-rich regions [70]. As such, EG modifies the structures of both PSS and PEDOT to enhance the conductivity of the polymer through two mechanisms, resulting in a popular chemical modification.

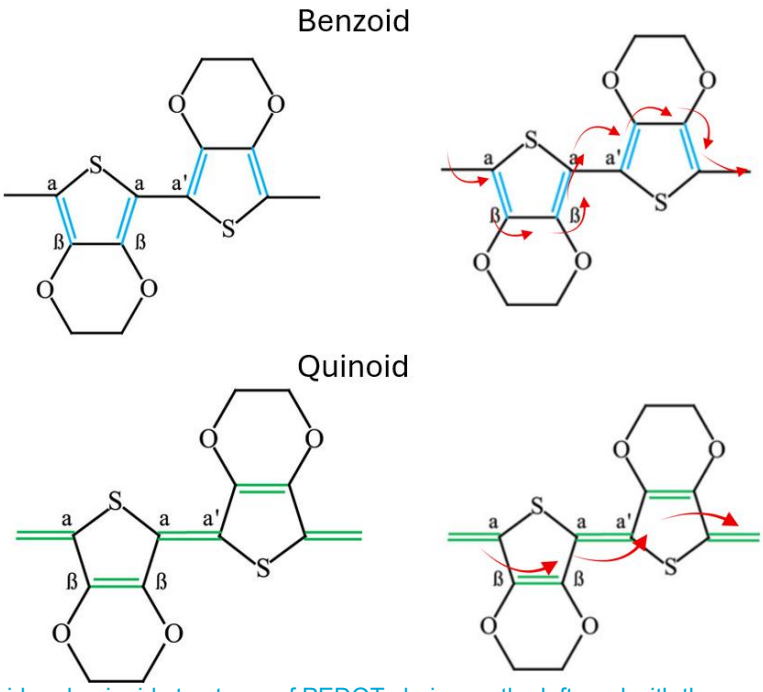

Figure 2-8. Benzoid and quinoid structures of PEDOT chains on the left, and with the conduction path of a charge on the right.

- **Dodecyl benzene sulfuric acid**: DBSA, in turn, etches away the PSS chains by weakening the hydrogen bonds with PEDOT while also transforming the PEDOT chains into a quinoid structure through oxidation charge transfer [72]. It is noted, however, that an excess of DBSA can negatively affect the structure of PEDOT, resulting in a loss of conductivity. The DBSA not only removes PSS but also replaces its chains entirely with itself, which is considerably smaller than the long PSS polymer, and acts as an anionic surfactant, reducing the surface tension of water. This causes a reduction of particle size and improved wettability that allows for better distribution of PEDOT in an aqueous solution.
- **3-glycidyloxy-propyl-trimethoxysilane**: In contrast, GOPS reduces the conductivity of PEDOT:PSS films, though mainly the ionic conductivity, since it interacts strongly with PSS, particularly the excess that is not bonded with any PEDOT chains [73]. It has been suggested that the working mechanism of this reaction occurs between GOPS' epoxy ring and PSS' sulfonate group bonding together, while GOPS' methoxysilane bonds with itself to create a cross-linked network of GOPS. The combination of occupied sulfonate groups and insulating cross-linked web reduces the overall conductivity of the films.

PEDOT:PSS and carbon nanocomposites

In contrast, carbon nanocomposites due not interact as strongly with the polymer chains of either PEDOT or PSS, but can still provide an enhancement in conductivity. Though, it is important to realize that this is mostly due to their own conductivity rather than improving the conductive characteristics of PEDOT:PSS. As such, the working mechanism of these materials will be lightly touched, with the focus instead being on PEDOT:PSS as the main material.

Graphene oxide (GO) is modified graphene sheets with oxygen-containing functional groups, such as carboxyls and hydroxyls, increasing solubility. The conductivity of graphene and GO is due to delocalized π-π electrons through the lattice structure formed by sp^2 bonds, turning the lattice to a sort of super-highway for conductivity, though GO less so due to defects. These oxygen groups separate the PEDOT-rich regions from the PSS-shells, resulting in elongated PEDOT linear chains that expand

the volume of PEDOT-rich regions [78]. Moreover, the GO increases the wettability of the PEDOT:PSS and allows for more percolation of the ions, thereby increasing the double-layer capacitance. A derivative of GO, carboxylated GO, cGO, is a carboxyl-dominated GO that has a higher reactivity and redox activity than GO [66]. This last one is possible due to covalent bonding with PSS and boosts the capacitance of the material. Lastly, reduced graphene oxide (rGO) is in between pristine graphene and functionalized graphene, with less oxygen functional groups than GO. As such, rGO is an alternative to find balance between the conductivity of graphene and the hydrophilicity of GO.

Carbon nanotubes are graphene sheets rolled into cylinders with a very high aspect ratio and can be divided into single-walled (SWCNT) or multi-walled (MWCNT). As such, the mechanism of enhancement is similar to graphene, with π-π interactions dominating, but also the introduction of a 'channel' effect [79]. This effect is related to the network formation of the CNTs, held together by van der Waals forces, which enhance the conductivity of the system. The CNTs, which can be further enhanced with carboxylation, interact with the aromatic rings of PEDOT to form a π-π conjugated interaction, allowing for electronic transfer between the PEDOT-rich regions along the CNT 'channel' bypassing the PSS shells. This applies as well to the carbon nanohorns, with the critical difference being twice the surface area (higher capacitance) and larger network pores (higher percolation) than SWCNTs.

Finally, the working mechanism of a layered PEDOT:PSS neural interface doped with CNTs in alginate hydrogel is explored through the authors' circuit model (**Figure 2-9**) [56]. First, PEDOT:PSS was deposited as a thin film on a metal wire electrode, thus leveraging the volumetric capacity of PEDOT:PSS and increasing the surface area. Then, while the alginate was being polymerized on the electrodes, MWCNTs were coated with PEDOT:PSS and electrodeposited on the same electrodes, further increasing conductivity with π-π conjugated interactions. Finally, PEDOT:PSS was grown inside the hydrogel to make the hydrogel conductive. Intuitively, the addition of PEDOT:PSS sites resulted in an increase in charge storage capacitance, but most importantly, the addition of PEDOT:PSS to MWCNTs to create the nucleation sites resulted in an increase deposition of PEDOT:PSS. However, the authors also found that an increase of electrodeposited PEDOT:PSS in the final step after a certain threshold can lower capacitance since the effective surface area is reduced by the clogging of pores. The authors decoded this trade-off with their equivalent circuit: PEDOT:PSS increases C_c (3.4 to 4.8 F) by improving ion coupling and faradaic capacitance while having a smoother capacitive interphase, as the CPE approaches the ideal value 1. After 200 seconds of electrodeposition, the R_p and R_s increase to start offsetting the gains made in C_c, which also reduces. Since the MWCNTs act as scaffolds for PEDOT:PSS and ion-percolation, excessive coating insulates them and hinders their performance.

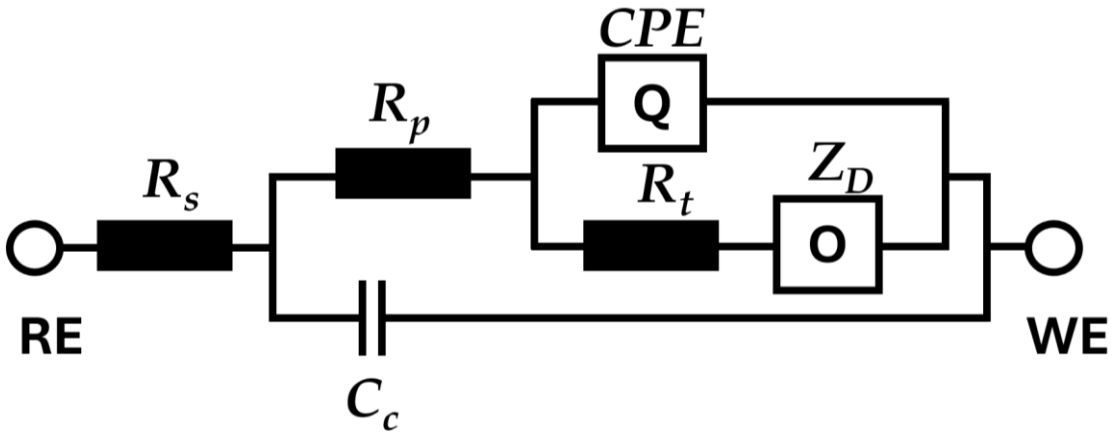

Figure 2-9. The hydrogel-electrode-electrolyte equivalent circuit model with circuit elements including solution resistance (R_s), coating capacitance (C_c), pore resistance (R_p), double layer interface impedance (Z_{CPE}), charge transfer impedance (R_t) and finite diffusion element (Z_D) *[56]*.

Unique approaches`

Other neural interfaces had design choices and implementations that did not fit in with the groups above. Their working mechanisms, while innovative, still present familiar elements.

The following device combines a stretchable material with IL-doped PEDOT:PSS/Au electrodes for long term neural culture [63]. The PEDOT:PSS/Au should share the same working mechanism as provided before, but there is an important difference with the inclusion of an ionic liquid. This additive enhances the electrochemical and conductive properties of the electrode by improving charge carrier mobility and percolation of conductive PEDOT chains due to the disruption of PSS-rich shells. The breakup of these shells allows PEDOT:PSS cluster to interact more freely, and this is also aided by the fact that the PEDOT:PSS is doped with more ions, leading to a reduced resistance and increased charge injection. Meanwhile, the stretchable material SEBS does not appear to contribute directly to the performance of the electrode at first, it mostly acts as an encapsulation layer to prevent leakage from the IL, but since this material stretches at relevant scales, changes in performance can be expected. However, the mesh device showed that under compression and tension the impedance was stable (±5% difference), though the charge injection capacity decreased by 19% at maximum strain. Thanks to the IL and the mesh design, the PEDOT:PSS/Au electrode maintains continuous conductive pathways with relatively low deformations even when stretched. This makes it ideal for conformal contact of organoids and laboratory handling.

Finally, the working mechanism of the lipid bilayer on PEDOT:PSS/Au electrode is deceptively simple [68]. First, the experimental set up is the closest to a conventional electrochemical cell, with a reference electrode and a counter electrode suspended in the electrolyte, while the working electrode is the PEDOT:PSS/Au film at the substrate. The authors actually model the device as an RC circuit: with the electrolyte resistance in series with the membrane capacitance||resistance and the capacitance of the PEDOT:PSS layer. While the first and last elements have been previously been explored in more detail, the membrane elements are just introduced by the researchers. Starting with the membrane capacitance, this relates the insulating properties of the lipid bilayer, as the cell membrane oversees maintaining a transmembrane potential between the cytoplasm and the interstitial fluid. The capacitor is dictated by the composition of the lipids and proteins that make up the cell membrane, as well as its defects. The membrane resistance, on the other hand, represents the ionic semipermeable nature of the bilayer and is inversely proportional to the amount of ion channels present in the membrane. More importantly, whether the channels are open or closed affects the resistance, making it a particularly

powerful tool for drug development. While the concept is relatively simple, the real challenge comes from obtaining the good lipid bilayers and depositing them to “seal” the PEDOT:PSS/Au electrode uniformly.

2.5 Discussion

The development of neural interfaces based on PEDOT:PSS has seen remarkable progress, driven by the need for low-impedance, high charge storage capacity and charge injection limit, and biocompatible electrodes capable of long-term stability in electrophysiological applications. By analysing material properties, interfacial mechanisms, and design innovations, this literature review addresses the core research question: **How does PEDOT:PSS improve the electrochemical performance of neural electrodes compared to traditional metal electrodes?** Findings from twenty studies (2016-2024) were synthesized to propose new models, identify unresolved challenges, and outline a research plan for next-generation neural interfaces.

2.5.1 Electrochemical performance: PEDOT:PSS vs metal electrodes

In all studies that compared PEDOT:PSS-metal composites to bare metal electrodes, the former had a reduction 1-2 orders of magnitude at the neurophysiological relevant frequency of 1 kHz, e.g. 40 kΩ → 0.128 kΩ at 1 kHz for Au [37]. This is explained thanks to the porous morphology of PEDOT:PSS that allows for a superior volumetric capacitance, an extended double-layer interface, and hybrid ionic-electronic conducting regions. Moreover, PEDOT:PSS is the perfect candidate for the interface between biological material and hard electronics. PEDOT’s HOMO level (~5 eV) enjoys an energy band similar to gold’s Fermi level (~5.1 eV), which facilitates hole injection and conductivity, while PSS enable ionic percolation from the electrolyte solution. In contrast with metals that rely solely on double-layer capacitances, PEDOT:PSS achieves faradaic pseudocapacitance in addition to its capacitive charge storage. This is extremely important to safely inject charge for stimulation purposes. The reversible redox reactions in PEDOT enables high CIL without harmful byproducts and electrode corrosion as with metals. Additionally, this can only be further improved with 3D designs that increase the surface area and volumetric capacitance.

2.5.2 Additives and carbon nanocomposites

PEDOT:PSS, when in dispersion form, are usually enhanced with three additives: ethylene glycol (EG), dodecyl benzene sulfuric acid (DBSA), and 3-glycidyloxypropyl-trimethoxysilane (GOPS). Both EG and DBSA enhance the conductivity by transforming PEDOT chains from coil-shaped benzoid to sheet-like (more conductive) quinoid structures, while GOPS enhances the stability of the PEDOT:PSS film by cross-linking itself and the PSS. EG also reorganizes the PSS so the insulating shell is thinner, while DBSA replaces it instead. All these properties come together to directly modify the conductivity of the PEDOT:PSS, though it could be interesting to see the addition of such compounds to the electrochemical deposition methods, either as a pre-treatment or post-treatment. As such, these additives represent a highly tuneable option to enhance PEDOT:PSS electrodes.

Carbon nanostructures are a popular conductivity enhancement for PEDOT:PSS composites, however, this improvement is due to the own conductivity of carbon nanomaterials, with limited interaction with the PEDOT:PSS unlike the mentioned additives. PEDOT chains interact with CNTs via π-π stacking, with a new ‘channel’ model being presented where CNTs bypass PSS-rich shells and connect PEDOT-rich regions. On the other hand, oxidized graphene and derivatives have been found to enable multimodal applications of MEAs, not only for electrophysiological applications but also sensing [62]. Finally, the carbon nanostructures can withstand numerous stimulation cycles and be integrated into complex environments such as hydrogels with good results.

2.5.3 Looking up: 3D design

As previously touched upon, there is also a push for MEAs to have a 3D design to better study 3D neural cultures. The most common examples are the inverse of each other: pillar and hollow-ring electrodes. While the pillars take advantage of the increased surface area and their limitation is how high they can reliably be, hollow-ring designs also capitalize on the increased surface area and the volumetric capacitance of the planar electrodes. Moreover, the pillars achieve high CILs and depending on the size they can guide neurite growth and minimize cleft space to achieve parallel capacitive pathways with reduced impedance. However, it is clear that these designs are more interested in the stimulation parameters as much of the spatial resolution is lost with the current fabrication techniques. On the other hand, in a breakthrough with stretchable flexible 3D MEA that used not only a criss-cross mesh design but also doped the electrodes with ionic liquids, ensuring that conductivity is preserved during stretching and actually enhances the performance [63]. Amazingly, the results showed integration with a long-term neural organoid with no signs of adverse effects, biologically or performance-wise. This last example may be suitable for the exploration of self-assembly tissue models or 4D biomaterials.

2.5.4 Challenges and opportunities

Notwithstanding the advancements made in the field, there are still challenges and opportunities ahead to be addressed. One such example is the scalability and fabrication, particularly for ink-jet and direct writing, which are low-throughput approaches that can produce vulnerable structures for delamination. Moreover, the literature showed the possibility of multimodal integration for recording MEAs, with stimulation, biosensing, and even scaffold applications that can further enhance the quality of the tissue model. Finally, long-term stability is a future direction more research projects should focus on, as more mature neuron cultures can provide better insight into the physiology and disease of the brain.

2.6 Concluding remarks

This literature review addresses the research question: **How does PEDOT:PSS improve the electrochemical performance of neural electrodes compared to traditional metal electrodes?** The findings highlight PEDOT:PSS as a transformative material for neural interfaces, offering superior electrochemical properties, biocompatibility, and versatility when compared to metal electrodes.

PEDOT:PSS significantly reduces impedance (by 1-2 orders of magnitude at 1 kHz) compared to metal electrodes, thanks to its porous morphology and hybrid ionic-electronic conductivity. Its volumetric capacitance and faradaic pseudocapacitance enable efficient charge storage and injection, critical for both recording and stimulation applications. Which can be further capitalized on with 3D geometries, dispersion additives, and paired with carbon nanomaterials.

In summary, PEDOT:PSS not only addresses the limitations of traditional metal electrodes but also opens new avenues for advanced neural interfacing, paving the way for transformative applications in neuroscience and medicine. Future research should focus on scalable fabrication, enhanced durability, and multifunctional integration to unlock its full potential in understanding and treating neurological disorders.

3 PEDOT:PSS thin films

This chapter touches upon the possibilities of using the conductive polymer PEDOT:PSS, thanks to its emergence as critical interface between electronic devices and biological systems due to its favorable properties in conductivity and biocompatibility. However, achieving optimal electrical and biological performance requires careful tuning of PEDOT:PSS properties through additives and processing techniques. This chapter explores the fabrication and characterization of PEDOT:PSS thin films that have been tuned for spin-coating with the additives EG, DBSA, and GOPS. The PEDOT:PSS films are cultured with cortical neurons for evaluating its biocompatibility. Moreover, scientific literature has shown that different acids can be supplemented as a post-processing step to further enhance the conductivity of the PEDOT:PSS films. Following this approach, it was decided to experiment with acetic acid to observe changes in conductivity, and this specific acid was chosen due to its availability and low risk. Finally, a discussion takes place concerning the biocompatibility of the PEDOT:PSS and its enhancement with acetic acid.

3.1 PEDOT:PSS deposition

Acid treatment of PEDOT:PSS is a common and straightforward technique to increase the electrical conductivity of the polymer after deposition. This process typically involves soaking or treating the films with strong acids such as sulfuric acid (H_2SO_4), hydrochloric acid (HCl), or organic acids. The acid releases protons that convert the polystyrene sulfonate (PSS^-) component into its neutral form (PSSH), which can then be easily washed away with (distilled) water. This removal of excess PSS reduces the insulating barriers between PEDOT rich regions, promotes phase separation, and leads to a more ordered and densely packed PEDOT structure [80]. In this section, an exploration of electrical enhancement of PEDOT:PSS films was done using acetic acid. Acetic acid is a simple organic compound, CH_3COOH, that has been investigated as a post-treatment material for PEDOT:PSS films [81].

PEDOT:PSS (Hereaus Clevios PH-1000) is well mixed with 5% v/v EG (Sigma Aldrich) and 0.5% v/v DBSA (Sigma Aldrich), then 1% v/v GOPS (Sigma Aldrich) is added to the mixture followed by sonication (Fisherbrand) for 8 minutes. In practice, a suspension of PEDOT:PSS will tend to aggregate, rendering the mixture heterogeneous, hence the use of a sonicator to break those aggregates into mor homogenous particles. A 0.45 µm glass fiber filter was used to further remove aggregates. The solution was then transferred to a glass film measuring 2.5 x 2 cm with a micropipette. Spin-coating was performed using an Ossila Spin-coater and 2500 rpm for 1 minute. Next the films were soft-baked at 90°C using a hot-plate (Thermo Scientific). Some films underwent the acid treatment by covering the whole film with acetic acid (99%) for 15 minutes. After which, the excess acetic acid was removed and the films were annealed for 1 hour at 140°C. Once done annealing, the films were stored at 4°C under ethanol (70%). These steps are displayed in **Figure 3-1**.

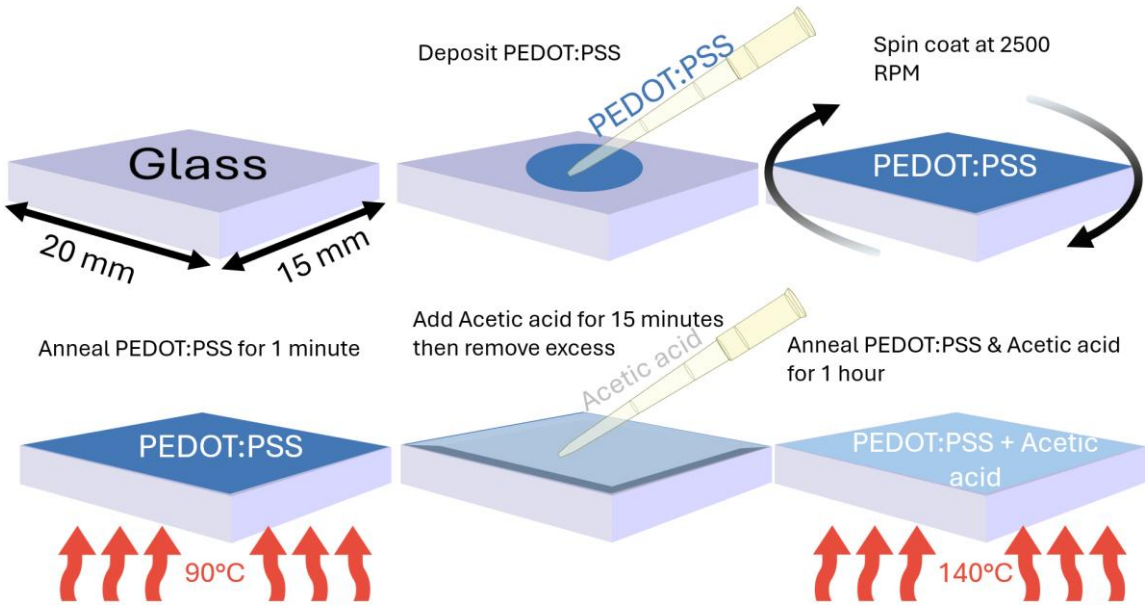

Figure 3-1. Acetic acid deposition on a PEDOT:PSS film

As for the measuring the conductivity of the films, a four-point probe (Four-Point Probe Plus, Ossila) was performed that was designed to probe soft materials. The results of the measurements are observed in **Figure 3-3**. In this case, it was observed that the acetic acid treatment had a slight, but significant, increase in conductivity when compared to the PEDOT:PSS films without the treatment.

3.1.1 Acetic acid results

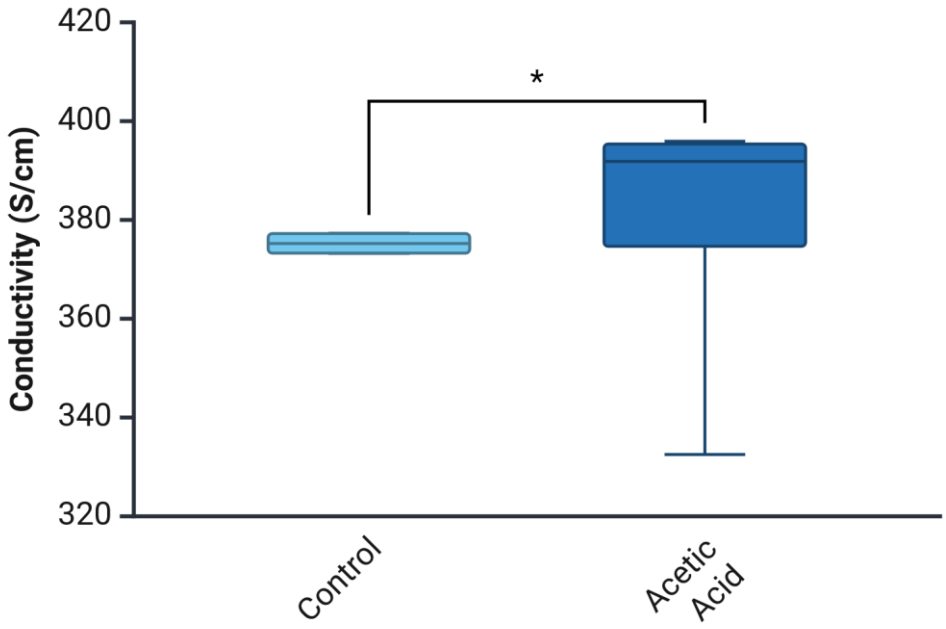

Figure 3-2. Box plot showing the conductivity measurements of the prepared PEDOT:PSS with and without acetic acid treatment. * $p < 0.05$, following an unpaired, two-tailed Mann-Whitney U test.

3.2 Biocompatibility assay

The biocompatibility of PEDOT:PSS is well researched in the literature and in this section films of the polymer were deposited on glass substrates and seeded with iPSC-derived neuronal progenitors (seen below in **Figure 3-3**). This was performed thanks to a collaborator who did the cell culture at Leids Universitaire Medisch Centrum (LUMC). Unfortunately, the acetic acid-treated films were not seeded for this assay. The figure proves the biocompatibility of PEDOT:PSS by clearly showing cell growth and attachment to the films. Though the

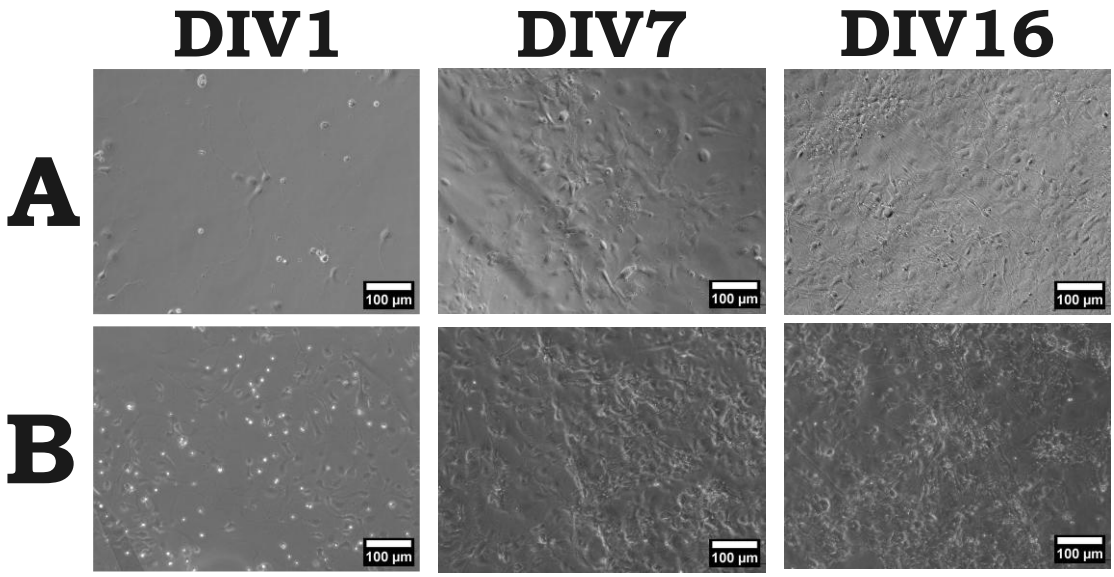

Figure 3-3. Neuronal culture derived from iPSCs on top of **A)** control group and **B)** PEDOT:PSS films.

3.3 Discussion

3.3.1 PEDOT:PSS conductivity enhancement

As discussed in the Literature Review, acid treatment is a popular method to enhance the electrical conductivity of PEDOT:PSS films, as can be seen in **Figure 3-4**. In that figure it can be seen how acid treatments improve the conductivity of PEDOT:PSS (particularly pristine which has a conductivity of around 0.2 S/cm [82]). This works because acids erode the PSS, allowing PEDOT-rich regions to have better inter-conduction, and not necessarily because the acids are somehow conductive themselves [80]. For acetic acid in particular, it has been shown that it can reach a conductivity of around 450 S/cm [81], which is significantly different from the one used in our results, but this is derived from the fact that the PEDOT:PSS used was pristine and without the EG, GOPS, and DBSA additives. Speaking of which, due to the working mechanism of the acid treatment, GOPS is the most directly affected of the additives and the one that can actually hinder the treatment thanks to its cross-linking of PSS regions. As future direction, it would be interesting to observe which acid treatment can increase the conductivity the most of PEDOT:PSS thin films when GOPS is present, and how does it affect the long-term properties of the film. In summary, acid treatments are a tried-and-true method of increasing the conductivity of PEDOT:PSS, especially true for pristine conditions without additives, but in this section it was proven that even a weak acid such as acetic acid can still increase the conductivity of PEDOT:PSS films with EG, GOPS, and DBSA.

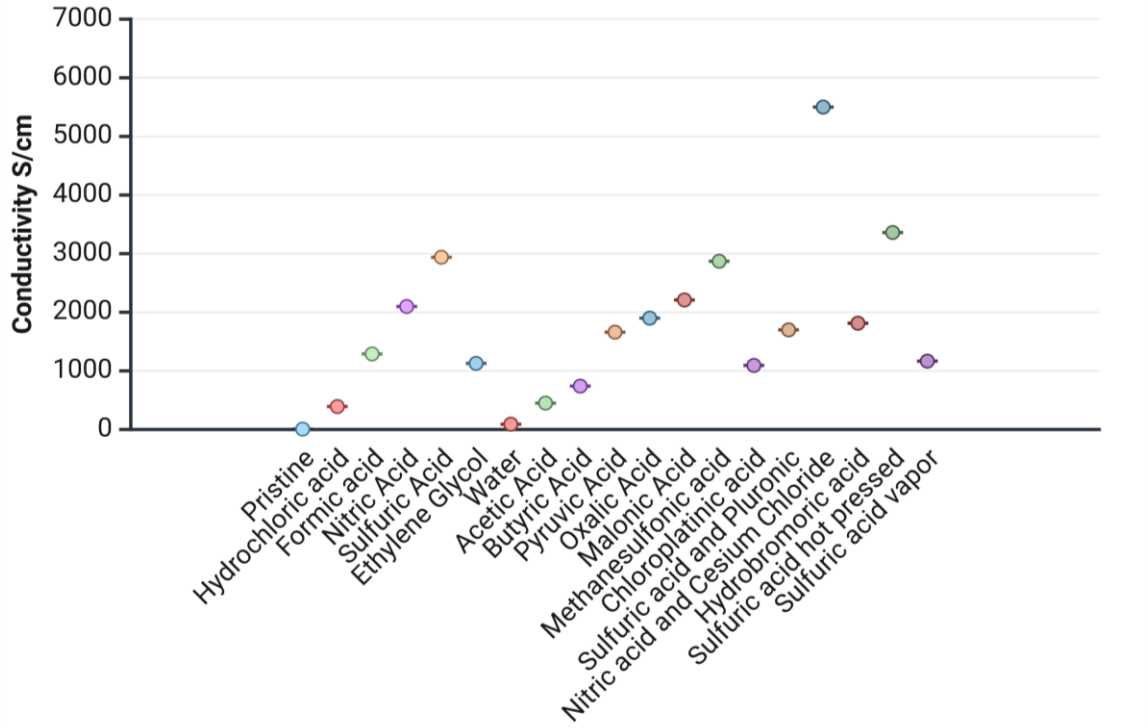

Figure 3-4. PEDOT:PSS* acid treatments found in literature. However, this is not a direct comparison since *different formulations and methods were used. [80], [81], [82], [83], [84], [85], [86], [87], [88], [89], [90]

3.3.2 PEDOT:PSS biocompatibility

Though brief, the biocompatibility assay of the PEDOT:PSS films was a successful insofar it. This is unsurprising, since PEDOT:PSS has been shown to be biocompatible with other materials. Naturally, a shortcoming of this section was the lack of biocompatibility assay that could directly assess acid-treated films. In any case, with PEDOT:PSS films it can be expected for neuronal cultures to differentiate and mature [91]. In fact, the neurogenic properties of PEDOT:PSS also have demonstrated that it can regulate glial density [92]. In summary, the PEDOT:PSS thin films were shown to be biocompatible, although further investigations are needed to assess the acetic acid. As for the next steps, exploring maturation of neuronal cultures and utilizing the polymer's conductive properties for greater roles such as electrical activity recordings or stimulation are of great interest.

3.4 Conclusion and future directions

In conclusion, a short set of experiments were performed to have a hands-on experience with the organic conductive polymer PEDOT:PSS. The main finding that the proposed method of enhancing the conductivity of the polymer using acetic acid was a success, while also ensuring that the PEDOT:PSS used was biocompatible. The biocompatibility results serve as a starting point for the next chapter as PEDOT:PSS is used more actively for neuronal cultures. For future directions, it is recommended to:

- Explore different acid treatments to assess their effect on PEDOT:PSS with additives, particularly stronger acids such as sulfuric acid.
- Culture neurons in vitro with acid treatment to assess biocompatibility and the neurogenic properties of the films.

4 Electrophysiological recordings of cortical neurons with MEA

From the humble depolarization-repolarization cycle found in action potentials to the enigmatic and complex interneural interactions, neural electrophysiology holds one of the keys to understanding the functionalities of neurons and the brain. Studying the electrophysiology of the neural tissue can be quite complex, regardless of the tissue being sensed in an *in vivo, ex vivo,* or *in vitro* setting, and MEAs are particularly useful for all settings. Of these, *in vivo* systems are the more complex devices that have the most constraints for a safe and effective implantable device, with the understanding that their application has the most direct results. Naturally, *in vivo* devices deal with the complexities of the brain, the artifacts from different regions of the brain, and the hostile environment of the body to foreign objects. *Ex vivo* devices, on the other hand, can assess specific regions of the brain, typically in the form of slices, with organotypic behavior without the aforementioned artifacts and environment. Finally, *in vitro* settings allow for the culture of neuronal cells, tissue, and organoids, which gives rise to different applications: neuron development studies, knockout/knock-in studies with CRISPR technology, (high-throughput) pharmacological studies and drug development, network dynamics, among others. In this chapter, a newly fabricated PEDOT:PSS MEA is used for the study of *in vitro* neural electrophysiology from iPSC-derived cortical neuron cultures. This chapter begins with the electrophysiological data acquisition setup and the conversion of the data type for analyses. Then, said analyses of the data are shown to both assess the performance of the MEA and characterize the cortical neurons. Finally, the results and methods are discussed and compared to the literature to find the limitations at hand and what improvements can be made.

4.1 MEA recording setup and data acquisition

An in-house MEA with PEDOT:PSS- only electrodes was designed to be compatible with the recording systems of commercially available MEAs (See Supplementary Information: MEA). As such, there was no need to design and fabricate custom electrode readers and instead it was a matter of simply plugging the device to and optimizing the parameters of the established channel measuring device. **Figure 4-1** shows a schematic of such measurement set up (**A**) and its data acquisition (**B**).

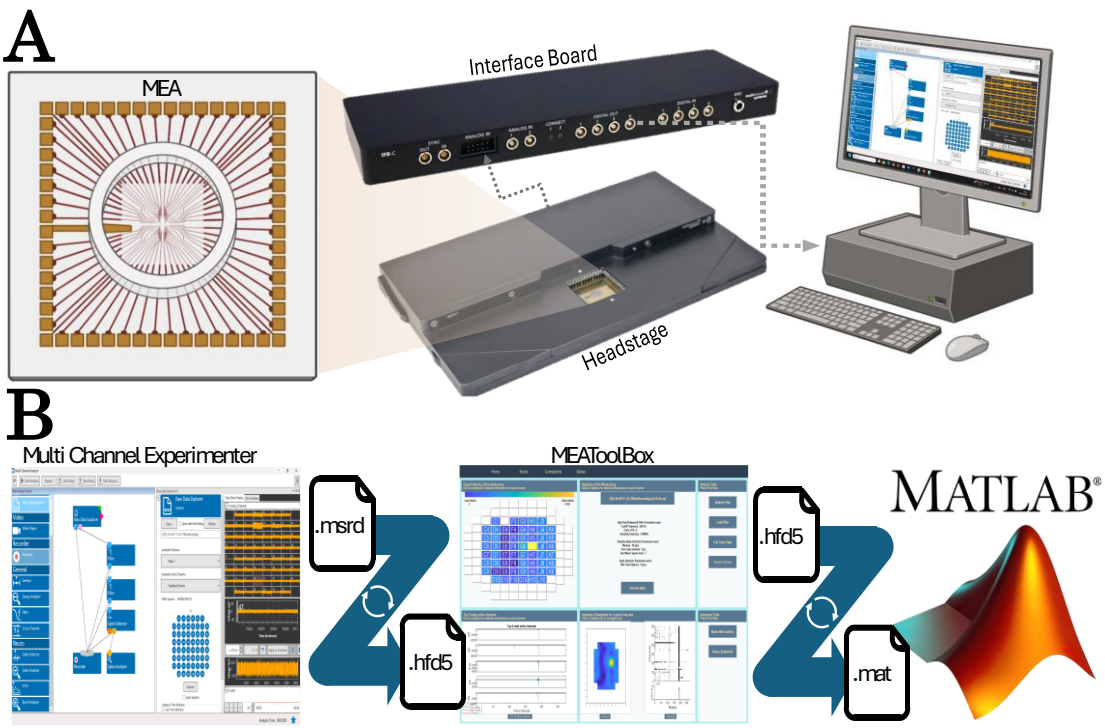

Figure 4-1 **A)** Schematic representation of the devices and connections for the MEA data collection. The MEA is read by Multi Channel Systems' MEA-IT60, whose data is converted and processed by IFB-C Interface Board Multiboot for real-time sensing. This is connected to a computer with Multi Channel Experimenter program. **B)** Data conversion steps from the Multi Channel Experimenter program to the MEAToolbox and MATLAB® programs.

The MEA is inserted in the measuring device (MEA-IT60, Multi Channel Systems), which has an amplifier, analog-digital converter, and stimulus generator. This device is the connected with an iX-industrial cable type B to the interface board (IFB-C, Multi Channel Systems) capable of digital processing of the signal for in real-time filtering, analysis and feedback stimulation. Intuitively, these last functions and the recording of the data are done with a personal computer, using the Multi Channel Experimenter or Analyzer application, connected by an USB 3.0 cable. With this application, it is also possible to graph, review, and save the recorded data. Furthermore, with the 'record' option it is possible to save all the experimental parameters and output data from every channel, as seen on **Figure 4-2**. In the same figure the filters used in place to reduce the noise are in the low-frequency domain (>200 Hz) and the 50-Hz electrical noise, which is inherently present in the electronics in the European continent. As for the 200 Hz high-pass filter, this is commonly used to filter out artifacts such as cell movements and offset of the signal, using a Butterworth type filter to have a frequency response as flat as possible [93], [94]. These filters are used for the visualization of the recorded signals on the Multi Channel Systems applications only.

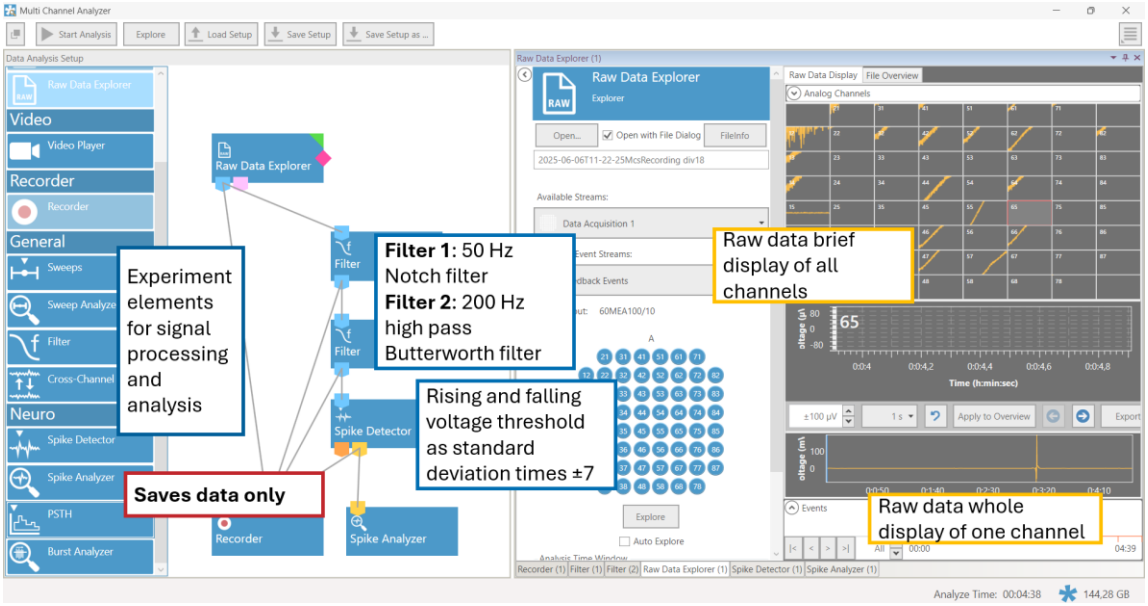

Figure 4-2. Multi Channel Systems Analyzer application.

Once the data is properly recorded in its *.msrd* file format, it can be transformed into a more accessible file format to better analyze the recordings without relying on the Multi Channel Analyzer, which has limited analyzing prowess. This was done only with the program Multi Channel Data Manager, which transformed the recorded data into an *.hdf5* file. HDF5, or Hierarchical Data Format version 5, is used for large, complex, and heterogeneous data and can be described as a single file containing within itself a hierarchical file system, similar to a *.zip* file. Its format allows for self-description in a ranked manner with metadata describing each object and level within the file, allowing for a facilitated application in other programs.

4.1.1 MEAToolBox

Evidently, with the *.hdf5* format it was possible to analyze the electrophysiological recordings with open-source programs. In this work, the MEAToolBox open-source program based on MATLAB® was used to extract and analyze the data from the MEA. More detailed information on the MEAToolBox can be found on https://github.com/mhyhu/MEA-ToolBox, but the functions used are also described in this section.

The program opened with the setting parameters for data analysis, in which the sampling frequency was set to 10,000 Hz and the spike detection threshold was 7x RMS (root mean square) noise as has been suggested in literature [95], the rest of the parameters were left in the default (seen in **Figure 4-3**).

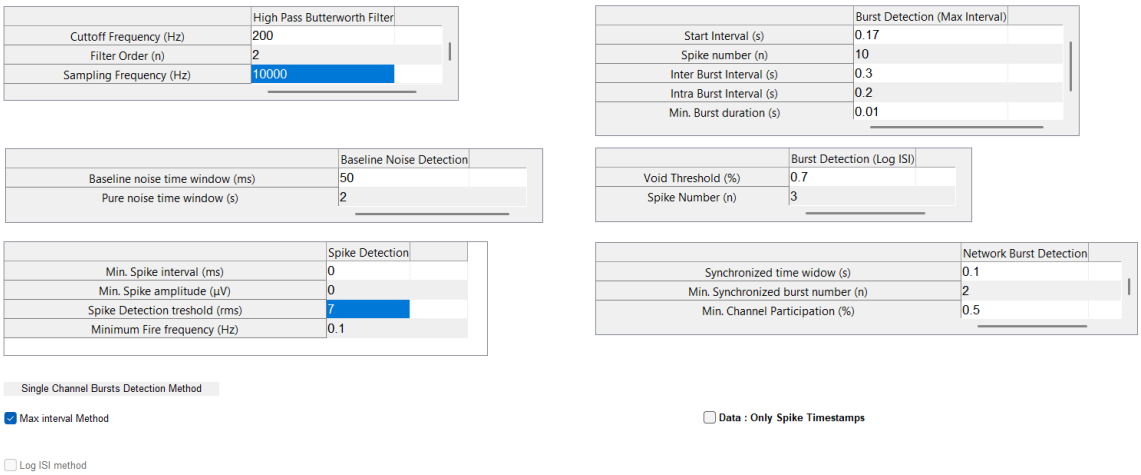

Figure 4-3. Starting parameters of the MEAToolBox program.

After the parameters were correctly set, the program analyzed the *.hdf5* file and a new window opened with different results of the analysis: heatmaps and raster plot of the spike activity per electrode, recordings of the five most active channels, statistics of the whole array, and other tabs with more functions (a screenshot of the opening window is seen on **Figure 4-1B**). Then it is simply a matter of saving the file in a *.mat* format to further analyze it with the MATLAB® program. Still, the MEAToolBox provided further valuable information such as the baseline noise levels, from which voltage-based threshold for spike detection were derived, spike data (location, timestamps, magnitudes, and 3.2 millisecond snippets), and, crucially, the code behind spike detection.

4.1.2 MATLAB®

Despite the usefulness the MEAToolBox provides as an MEA analyzer, the purpose of this chapter is to be able to understand and analyze neural electrophysiological recordings. For this reason, the MEAToolBox was used as a preliminary data analysis and converter to *.mat* format. Unlike the *.hdf5* format file, the given *.mat* file by the MEAToolBox also includes the analyses done by the program, while maintaining the original data. The data extracted from the *.mat* file were the filtered recordings per channel, the spike activity (timestamps and voltage values) and the voltage threshold values for each electrode to sense action potentials. These values were analyzed with help of the source code, which was modified to have additional pre-processing steps for data cleaning (See Supplementary Information: MATLAB code).

4.2 Electrophysiological recordings

Cortical neurons derived from iPSCs were cultured and differentiated by a collaborator at LUMC for 19 days (**Figure 4-4**). Though the neurons presented some atypical low confluency and slow growth, per empirical observations, the MEA was able to detect activity from the cells.

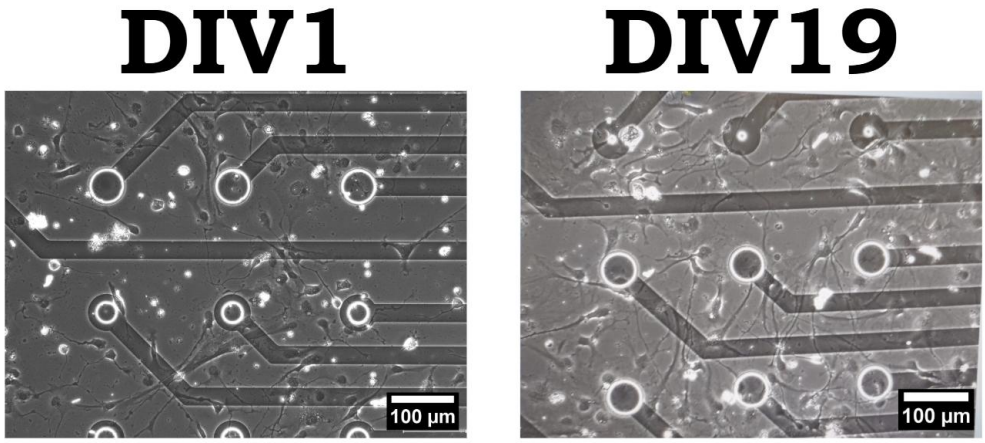

Figure 4-4. Widefield images of iPSC-derived cortical neurons.

The electrophysiological recordings were performed on DIV 19 with a recording time of 4’38” with the previously mentioned recording setup, seen on **Figure 4-5**. There was no stimulation performed on the electrodes, so the activity recorded was purely spontaneous (best seen in **Figure 4-5ii**). While action potentials are well established to be in the order of millivolts [34], [96], this is true for intracellular recordings. Instead, extracellular recordings are typically in the order of microvolts, though advances in electronics have reached millivolts as well [97], due to the current generated by the change of transmembrane potentials, the medium impedance, and the distance and properties of the electrode [97]. It was also seen in **Figure 4-5i.**, that there were some signals of very high amplitude for around 10 seconds after the 3’ mark found across all electrodes. These artefacts negatively impacted the (automatic) analyses made by both Multi Channel Systems and the MEAToolBox, as such, data cleaning was done with MATLAB®. As previously mentioned, the spike detection algorithm is based on the noise levels of the particular electrode. More specifically, it is a voltage threshold with seven times the value of the RMS of the noise, which is results in a value close to the standard deviation, and can be best seen in **Figure 4-5B**. Adding more constraints in the spike detection code proved cumbersome, and, with the cause of such unusually high-amplitude artefacts remaining unexplained, it was decided for the extraction to omit the artefact window entirely.

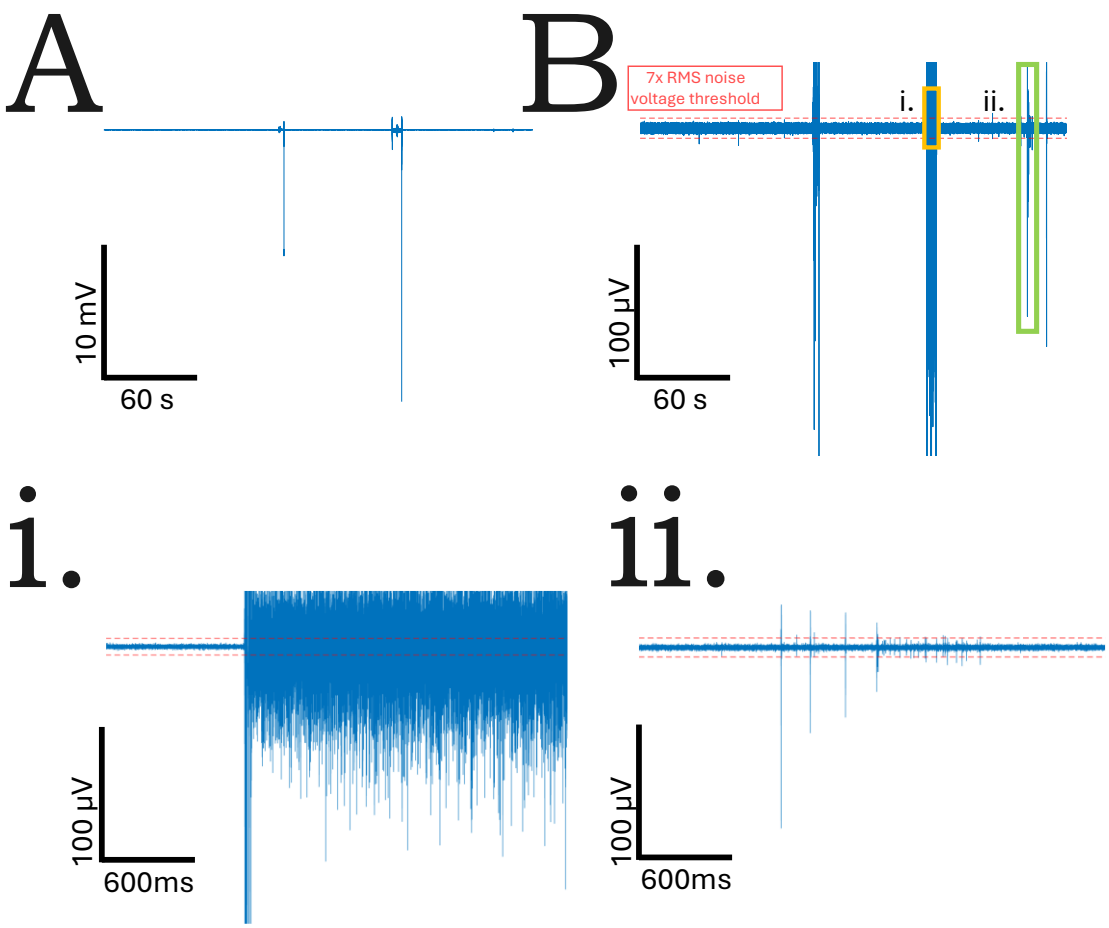

Figure 4-5. **A)** complete neural activity recording from a single electrode channel, and **B)** with the y-axis scaled down, showing the voltage threshold value used to detect the spike activity (in red). Insets are zoomed in in **i.)** and **ii.)** to showcase the non-spike artefact activity and spike activity found.

Next, the spike waveforms were extracted and sorted to assess the neuronal activity in the MEA, and some additional cleaning of the data was done to purge non-waveform artefacts (**Figure 4-6**). For the extraction of the waveforms, code from the respective MEAToolBox source code was modified and used to extract the spikes. All waveform snippets start 1 millisecond before the peak signal of the spike and continue 2.2 milliseconds afterwards. The waveforms were then categorized according to the shape of the waveform in this period and the threshold values of their respective electrodes. Monophasic waveforms were defined as having a single large (i.e. threshold-crossing) negative peak at the 1 millisecond mark. Biphasic waveforms were identified as having one large negative peak at the 1 millisecond mark followed by a large positive peak. Triphasic waveforms consisted of a one large negative peak at the 1 millisecond mark preceded by and followed by large positive peaks [97]. Lastly, the code of the MEAToolBox that extracted the spike activity also produced waveforms that did not have their peak at the 1 millisecond mark or crossed the negative voltage threshold multiple times without having a positive peak. This last type of waveform was named non-phasic and considered to be undesired data. Moreover, each waveform was sorted according to the amplitude of the negative peak to better observe the differences within each waveform type. For extracellular recordings of action potentials, as is the case here, negative spikes account for approximately 80% of recorded activity and are usually the basis for the assessment of somatic activity [97].

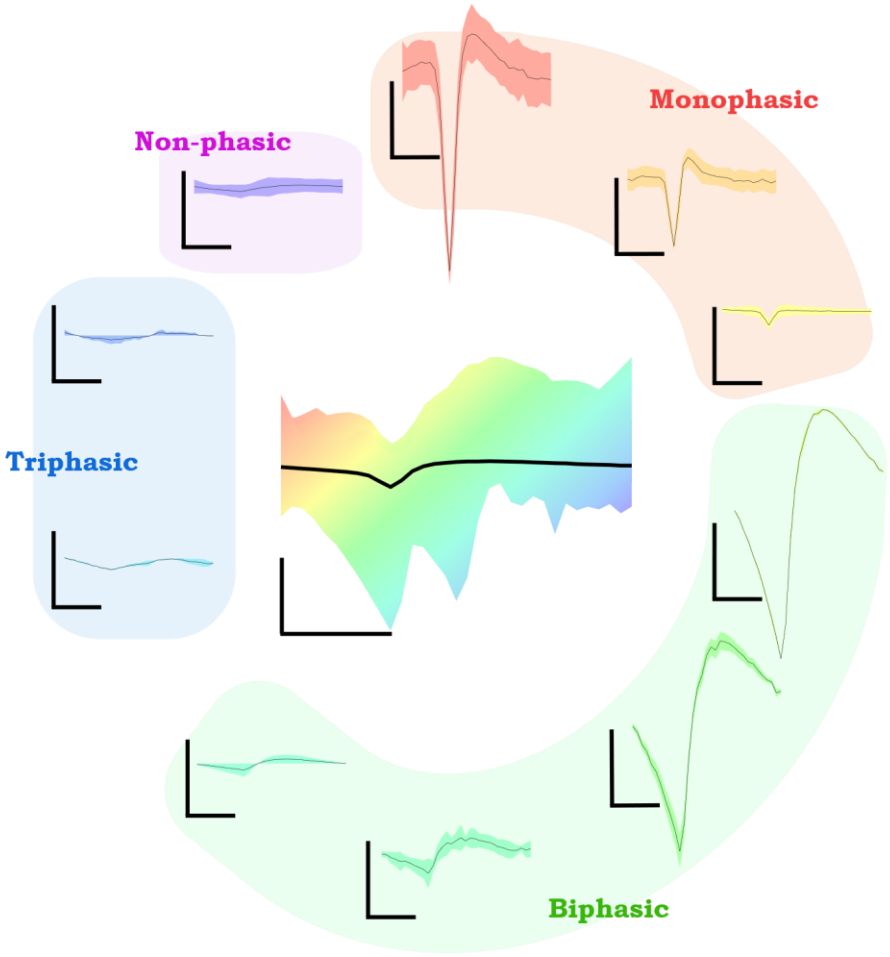

Figure 4-6. Center: Range of unsorted negative spike waveforms extracted from all electrodes in the MEA with the average as the solid black line. Shaded regions from top, clockwise: Spike waveforms with a monophasic, biphasic, triphasic, or without a phasic shape per noise-dependent voltage threshold extracted from each electrode. Within each shaded region the waveforms are sorted by their peak values in relation to the average of all respective waveforms. Scale bars: horizontal, 1 millisecond; vertical, 200 μV.

The same was done with the waveforms that had a positive peak instead, as seen on **Figure 4-7**. Under this context, these wave forms would indicate the electrode was detecting sodium ions depletion from regions acting as sources, such as dendrites, to the active sink zones, represented by the axon hillock [97]. Since the mechanism of extracellular current generation for positive spikes is less powerful than action potentials, the amplitudes are typically much smaller in comparison. The number of waveforms for negative and positive spikes were 526 and 143 respectively, which fits the reported value of ~80% of all recorded waveforms being negative (78.62% in this case). The present algorithm produced an excessive number of false positives (non-phasic waveforms) with the negative spikes having 577 non-phasic waveforms and the positive signals 608, both being more than half of the recorded signals.

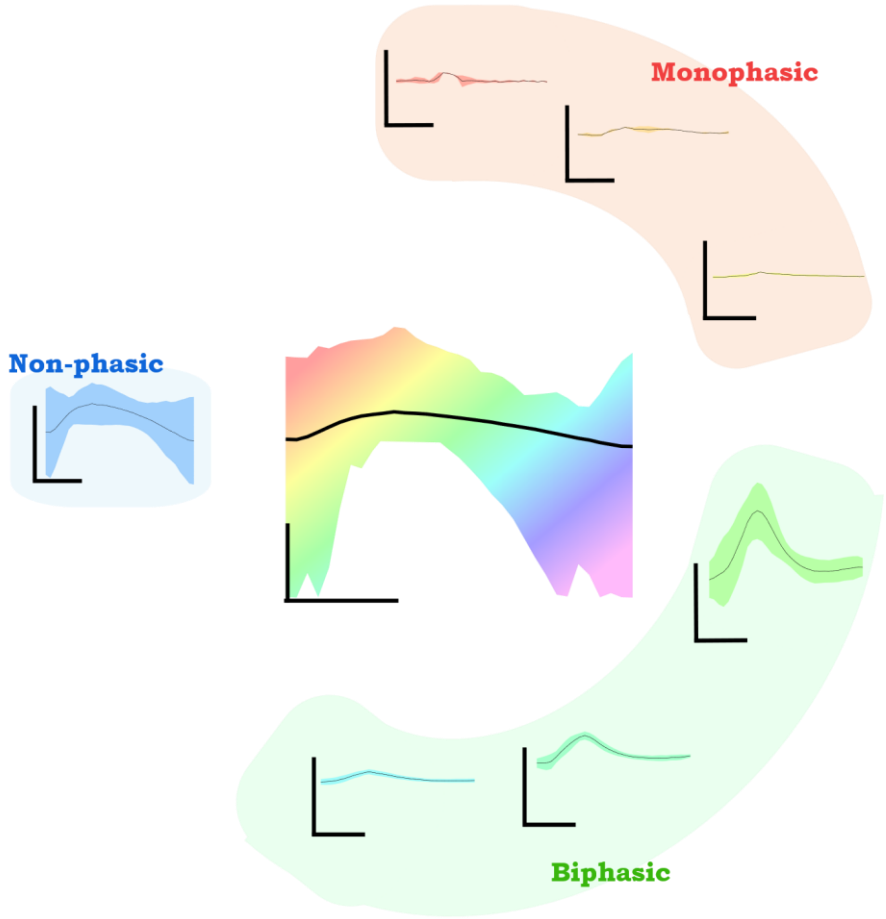

Figure 4-7. Center: Range of unsorted positive spike waveforms extracted from all electrodes in the MEA with the average as the solid black line. Shaded regions from top, clockwise: Spike waveforms with a monophasic, biphasic, or without a phasic shape per noise-dependent voltage threshold extracted from each electrode. Within each shaded region the waveforms are sorted by their peak values in relation to the average of all respective waveforms. Scale bars: horizontal, 1 millisecond; vertical, 200 μV.

With these waveforms and control of the detection code, it was possible to count how many actual spikes each electrode had to see the real activity across the array (**Figure 4-8A**). Only one electrode did not detect any neuronal activity. Furthermore, the SNR of the electrodes from the waveform spikes as well (**Figure 4-8B**). To quantify the SNR, the following equation was used:

$$SNR = 20 \times log_{10}\left(\frac{V_{RMS,peak}}{V_{RMS,noise}}\right),$$

Equation 1- SNR

where $V_{RMS,peak}$ is the root mean square (RMS) of peak signals measured and $V_{RMS,noise}$ is the RMS of the noise This approach was selected due to its straightforward nature, though it is not the only way to calculate the SNR (see SNR below). In any case, it has been established that purely PEDOT:PSS electrodes in an MEA can be used to assess the electrophysiology of neural cultures.

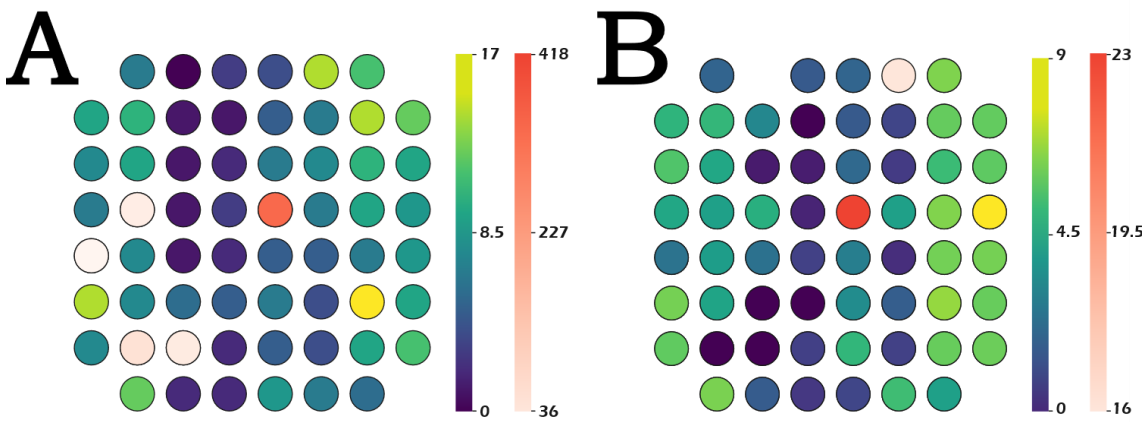

Figure 4-8. Summary of the MEA recordings. **A)** Number of detected neural activity that corresponded to the spike waveforms per electrode. **B)** SNR values found in the MEA recordings.

4.3 Discussion

4.3.1 Spike detection

Action potential detection and sorting is a complex challenge requiring ingenious mathematical and coding skills. One approach is using the normalized template matching (NTM), that detects spikes by comparing extracellular voltage recordings to prototypical spike waveforms ("templates") representing individual neurons, using a normalized similarity metric [98]. Spikes are detected when the similarity score exceeds a set threshold, indicating that the investigated signal closely matches one of the known templates in both shape and amplitude. This contrasts with the approach used in this thesis: the standard fixed-threshold (SFT) method, as previously explained. However, these approaches are not necessarily mutually exclusive, in fact, it is not unheard of to use the SFT in conjunction with the NTM to first detect the waveform and then sort it according to the template [95]. In general, using NTM is more robust to noise and firing rate fluctuations than SFT, and it improves spike detection sensitivity, especially for spikes that may otherwise be missed in noisy or dense firing conditions. In fact, considering that the SFT method had a combined false positive rate of 66.6%, it is highly recommended to improve the current algorithm used in this due to a relatively low SNR and variations in noise and spike amplitudes that led to false positives (non-phasic waveforms) and possibly false negatives.

As alluded to earlier, NTM is not the only spike sorting algorithm available in use. *Table 4-1* shows additional approaches and their advantages and limitations [98]. It is worth mentioning the different benchmarks these algorithms should be subject to for making an informed decision when choosing one. These benchmarks consist of comparing the number of false positives and negatives, and true positives and negatives to obtain the precision, hit-rate, and false-positive rate of the algorithms [95].

Table 4-1. Spike detection methods in extracellular recordings.

Method	*Spikes detected when...*	*Advantages*	*Limitations*
Standard fixed-threshold	A predetermined voltage threshold is crossed	Simple	False negatives/positives
Normalized template matching	Similarity with template crosses a threshold	Robust to global changes	Struggles with cluttered signals

Offline sorter nonlinear energy	The product of the amplitude and derivative is not 0	Good for high-frequency signals	Poor performance at low SNR
Offline sorter signed energy	A threshold is crossed within a moving window	Robust to baseline shifts	Window size critical
Spike detection differential threshold	Reaches peak-to-peak threshold within set window	High specificity	Miss spikes in bursting activity
Precision timing	The relative maxima/minima pass dynamic checks	High temporal specificity	Computational load

4.3.2 Waveform shape

The relevance of spike detection algorithms is that the waveform of these action potentials can be tied to biological mechanisms. Maturation of the neurons is an important process that can be assessed with MEAs to avoid more invasive alternatives. Not only can the waveforms by themselves tell that neurons are maturing, but also changes in the shape and amplitude of the action potentials as the days pass can give insight into its maturation process [97]. Moreover, the decision to sort the waveforms between monophasic, biphasic, and triphasic was made due to the relevance each type has in neuronal electrophysiology, as seen on *Table 4-2*.

Table 4-2. Biological relevance of each waveform type for extracellular recordings

Polarity	*Phase*	*Biological relevance*	*Source*
Negative	Monophasic	Inward sodium currents during depolarization of action potentials near the soma	[97]
Negative	Biphasic	Spike propagation including axonal return current	[99]
Negative	Triphasic	Dendritic, somatic, and axonal spikes	[100]
Positive	Monophasic	Far from soma, dendritic or axonal currents	[99]
Positive	Biphasic	Spike propagation including axonal return current	[99]

The waveforms sorted with the present algorithm are affected by the spike detection used, and some waveforms need to be addressed further. When comparing with the consulted literature, it is obvious that some waveforms are misclassified. First, the detected triphasic waveforms are *not* helping elucidate the axonal and dendritic components of the action potential, since there is no pronounced negative peak, and should be considered the same as the non-phasic counterparts: false-positive. It is also suspected to be the same case for the positive monophasic spikes, though the peak is still discernable, if very small. For the negative biphasic waveforms, they differ from the ones discussed in literature and instead of having a smaller peak or bump after the large signal they instead have a positive peak mirroring the negative peak in terms of amplitude and duration. These can still fall under the biphasic type and more specifically in the biphasic unit, where both polarities are dominant, and can indicate the inward and outward currents during propagation [99]. Finally, the monophasic waveforms appear to display characteristic small peaks that can also be found in triphasic and biphasic spikes using other algorithms. This exemplifies the severe limitations that SFT has on its own for spike sorting.

4.3.3 SNR

The SNR of MEAs for neuronal activity is not a straightforward measurement either. As alluded earlier, there are plenty of approaches in literature that use more complex mathematical models for calculating the SNR that will be briefly discussed [101], [102], [103], [104], [105]. First, the SNR can be simplified to the ratio between a meaningful and background power, typically measured in decibels to properly express a wide range of values. Since power is proportional to the square of voltage, voltage values can be used instead of power, but it is also common to used power spectral density (PSD) of both the signal and noise to calculate the SNR [104], [105]. These relationships can be seen in

$$SNR_{dB} = 10 \times log_{10}\left(\frac{P_{Signal}}{P_{Noise}}\right) = 20 \times log_{10}\left(\frac{V_{Signal}}{V_{Noise}}\right) = 10 \times log_{10}\left(\frac{S(f)}{N(f)}\right)$$

Equation 2. SNR equations as measured in decibels.

Where P represents the power of either the signal or noise, V the voltage of either signal or noise, $S(f)$ is the PSD of the signal, and $N(f)$ of the noise. While SNR in the voltage domain is intuitive and can directly tell how distinguishable the spikes are from the noise, the power spectral domain allows for more comprehensive signal and noise analyses. Ultimately, it is a matter of research objectives and context for the choice between these options. Power spectral SNR is useful for system design and noise mitigation, shining light on environmental interference and intrinsic thermal noise. In contrast, voltage domain SNR is the preferred metric for spike-based analyses, where the immediate clarity of individual waveforms matters most, as such, this is what was used in this work. In the end, the average SNR across all electrodes was found to be 4.69 ± 4.14 dB.

There was an intent to benchmark the SNR obtained here against those established in the literature, however, there were significant disparities encountered. Differences in SNR calculation, the heterogenous nature of cell culture, and the different designs of MEAs, obstruct drawing direct comparisons with the present MEA. For example, PEDOT:PSS/Au electrodes and transistors obtained SNR measurements of 30.2 dB and 52.7 dB respectively, using power spectra technique and in vivo setting [106]. While an implantable IrOx MEA obtained an average SNR of 17.1 ± 0.9 dB and 16.8 ± 0.8 dB for higher-density and lower-density arrays, but they also calculated the SNR from the *amplitude range* peak-to-peak over the RMS voltage [107]. These examples serve to highlight the challenges of literature comparisons and suggest a lack of standardization for SNR assessment methodology.

4.4 Conclusions and future directions

The work done in this chapter resulted in many insights into the works of detecting and analyzing neuronal electrophysiology. The custom MEA with PEDOT:PSS-only electrodes successfully captured spontaneous neuronal activity in an *in vitro* setting, which was able to be done thanks to the data conversion workflow used. Combining custom MEA design with commercial hardware (Multi Channel Systems), open-source software (MEAToolBox) and custom MATLAB® scripts proved to be viable, though admittedly cumbersome, for data acquisition, pre-processing, and spike analysis. However, the standard fixed-threshold spike detection method exhibited a high false-positive rate (minimum 66.6%), underscoring the need for more sophisticated algorithms, such as normalized template matching, to improve sensitivity and specificity in future work. This is particularly important because it affects the analysis of waveform shapes (monophasic, biphasic, triphasic) through misclassification. While the present MEA exhibited a signal-to-noise ratio much lower than what can be achieved in the literature, this conclusion must be approached with nuance since discrepancies can be explained by differences in methodology or quality of the cell culture.

In short, as directions for the future include:

- Refining spike detection algorithm. Preferably using NTM or a hybrid approach to reduce the number of misclassifications.
- Culture conditions. Addressing low neuronal confluency to increase quality and quantity of the activity.
- Validation with robust models. Using mature and established neural networks or even simultaneous intracellular recordings can offer a better insight into the MEA
- Signal and noise definition. Settling into a more robust SNR methodology using power spectral density for easier cross-study comparisons.
- Explore the effects of stimulation to evoke neuronal responses and assess the stimulation capacity of the MEA.

In summary, this chapter establishes a foundation for using PEDOT:PSS MEAs for *in vitro* neuronal studies while candidly addressing current limitations in neuronal activity analysis. By following these directions, future iterations could achieve higher precision and broader applicability in electrophysiological research.

5 Development of a motor neuron differentiation protocol

The purpose of the work in this chapter was to develop a differentiation and culture protocol of MNs for eventual integration with MEA technology for electrophysiological characterization. The chapter starts with detailed descriptions of the reagents and procedures done to achieve the culture of MNs. Then the results are presented with representative figures of brightfield images, immunofluorescent results, and calcium imaging, as well as statistical analyses done. Finally, discussion of the results and future directions are given to supplement the protocol.

5.1 Materials and methods

The Motor Neuron Progenitors (MNPs) (Axol Biosciences, ax0078) came with a culture protocol found in **here** (*axolbio.com/wp-content/uploads/2023/12/axol-user-guide-monoculture-axocells-motor-neuron-progenitors-december-2023.pdf*) that results in the culture of Motor Neurons (MNs). In this section, a chemically defined media different to the commercially available one provided by Axol Biosciences and an alternative surface coating are described, in addition to the methods for culturing the MNPs.

5.1.1 Coating

A Geltrex (Gibco, A14132-02) based coating was defined as of equal parts DMEM/F12 with Glutamax (Gibco, 31331-028) and Neurobasal (Gibco, 21103-049) medium diluting 100x Geltrex to create a 1x working solution. The Geltrex was thawed in an ice bath for an hour and the media with the predetermined amount were chilled in the same ice bath for an hour. After thawing, the ice bath was sprayed with isopropanol and transferred to a biological cabinet where the Geltrex was mixed with the media while in the ice bath. The coating solution was deposited on wells of a 24 well plate (Avantor, 10062), 500 µL per well. The coating was incubated for at least an hour at 37 °C. The coating solution was removed just before seeding the cells without significantly evaporating.

5.1.2 Thawing and plating

For the thawing of the MNPs, the chemically defined media, hereby referred to as MNEMi (Motor Neuron Expansion Medium with ROCK inhibitor) and previously defined by Spijker et al [108], was prepared before the thawing on the same day. It consisted of equal parts DMEM/F12 with Glutamax and Neurobasal medium, supplemented with 0.5 × N2 supplement (Thermo Fisher, 17502-048), 0.5X B27 supplement (Thermo Fisher, 12587-010), 1% penicillin/streptomycin (Sigma, P4333), 0.1 mM ascorbic acid (Sigma, 49752), 3 µM CHIR99021 (Axon Medchem, 1386), 2 µM DMH-1 (Sigma, D8946), 2 µM SB431542 (Sigma, S4317), 0.5 µM purmorphamine (Enzo Life Sciences, ALX-420-045-M001), 0.5 mM VPA (Sigma, P4543-10G), 0.1 µM retinoic acid (Sigma, R2625), up to here this medium is hereby called MNEM, and the addition of 10 µM of Y-27632 2HCl (Rho-associated coiled-coil kinase, ROCK inhibitor) (Focus Biomolecules, 10-2301) gave MNEMi. The cell cryovial was warmed in a water bath at 37 °C with 2/3rds of the vial submerged as to not let water seep into the cap. The cryovial was removed from the water bath with a small chunk of ice still inside and then transferred to the biological cabinet, sprayed with isopropanol before entering the cabinet. The completely thawed cryovial was aspirated using a P1000 micropipette and gently deposited in a 15 mL tube containing 8 mL of MNEMi, with 1 mL extra to rinse the cryovial and transfer again to the 15 mL tube. The cells were centrifuged (Multifuge 3L, Heraeus) at 200xG for 5 minutes, after which the cells were transferred back to the biological cabinet and the supernatant was gently discarded without affecting the cell pellet. With 1 mL

of MNEMi the cells were gently resuspended and then counted. For counting, 10 µL of well-asppirated cell suspension were extracted and mixed with equal parts stain (Luna, L13002) and deposited in a 10 µL chambers of the cell counter, then again for the other chamber, and counted accordingly using the Luna II™ automated cell counter. The appropriate cell density was chosen (130,000-180,000 cells/cm2) and the respective amount of cell suspension was deposited in the previously coated wells. The media was changed to MNEM 24 hours after seeding and onwards every other day a half media change was done.

5.1.3 Expansion and passaging

The expansion of MNPs used MNEM (Motor Neuron Expansion Medium) as previously described in the thawing and plating section for the MNPs. The cells were seeded between 75,000 to 150,000 cells/cm^2 per well and 24 hours after plating the media was changed completely to MNEM and then every other day a half media change with MNEM. MNEM was stored in the fridge (4-8°C) and protected from light. The MNEM was warmed to 37°C before doing a medium change.

For passaging, the wells were first washed with pre-warmed 1x DPBS once and then room temperature Accutase (Sgima-Aldrich, A6964) with a density of 250 µL/cm^2 is added. The Accutase was not prewarmed beforehand and was aliquoted upon receipt in -20°C, thawed at room temperature on the day of use. The cells were then incubated at 37°C for 10 minutes, although the detachment of all cells is not guaranteed by just waiting passively, thus, the cells were mechanically detached by carefully aspirating the medium with a P1000, letting the flow of water detach the cells. Once suspended, the cells are transferred to a 15 mL tube and some Accutase was used to rinse the wells well and transferred to the tube for centrifugation. The centrifuge parameters were the same as for thawing the cells: 200xG for 5 minutes. The supernatant was then carefully aspirated and then the cells were resuspended with MNEMi and seeded in prepared wells.

5.1.4 Cryopreservation

The cryopreservation medium Cryo-SFM (Sigma-Aldrich, C-29912) was chosen as the cryomedium for the MNPs, and no attempt to freeze differentiated MNs was made. To cryopreserve the cells, the same protocol for passaging was used. In this case, however, the cells were resuspended with Cryo-SFM and then deposited in cryovials (Greiner Bio-One, 122263) with a cell density of preferably 2 million cells and a minimum of 1 million cells per vial. The volume of each cryovial was of 1 mL of Cryo-SFM. The cells were then transferred to a -20°C freezer with a controlled freezing rate of -1°C/min and left overnight. The next day, the vials were transported to long term storage with the vapor phase of liquid nitrogen.

5.1.5 Differentiation

For the differentiation of the MNPs the following differentiation medium: equal parts DMEM/F12 with Glutamax and Neurobasal medium, supplemented with 0.5 × N2 supplement, 0.5X B27 supplement, 1% penicillin/streptomycin, 0.1 mM ascorbic acid, 0.5 µM purmorphamine and 0.1 µM retinoic acid. This medium is hereby referred to as MNDM, Motor Neuron Differentiation Medium, and is supplemented after 6 days from seeding with 0.1 µM compound E, denominated as MNDM+E. This is in accordance to the protocol established by Spijker et al. [108]. MNDMi, which is MNDM and 0.1 µM of ROCK inhibitor, was used to seed the cells for differentiation on day 0. A complete medium change was performed 24 hours after seeding to MNDM and again 72 hours after seeding. After which, a half medium change was performed every other day with MNDM and MNDM+E after day 6.

5.1.6 Immunostaining

The day of staining, the cells were blocked with 2% Bovine Serum Albumin (Roche Diagnostics, 10735078001) in 1x PBS for 30 minutes at room temperature. A 1x PBS wash was done once for 20 minutes at room temperature. During this waiting time, the antibody solutions were prepared using the blocking solution to dilute DAPI 1000x working solution and Phalloidin 1000x working solution

separately. Each stain was deposited simultaneously to the cells, then the wells were wrapped with Parafilm and aluminium foil left overnight at 4°C. Before imaging the cells, the staining solution was aspirated, and the cells were washed with 1x PBS thrice for 10 minutes each in the dark. The fixed neuronal cultures were also stained with neurofilament marker MAP2 at LUMC.

5.1.7 Calcium imaging

Calcium imaging of the cells was done with imaging medium and calcium staining and with the microscope incubator heated up to 37°C at least 90 minutes before the imaging. Imaging medium (IM) contains FluoroBrite DMEM (Gibco, A1896702), 1x glutamax, 1% penicillin/streptomycin, 1x sodium pyruvate (Gibco, 11360070), and 10 mM HEPES (Gibco, 15630080). Calcium staining was prepared from a 100x stock solution of 1 mM Fluo-4 AM (Thermo Fisher, F14201) in DMSO and diluted in the IM. The reagents were to be warmed up to 37°C, the cells were washed once with IM and then the calcium staining was added and incubated for 1 hour. After which the cells were washed twice with IM and kept at room temperature for 15 minutes. They were then transferred to the microscope incubator and left incubating there for another 15 minutes before starting the imaging.

5.2 Results

The path towards the differentiation protocol of the MNPs was definitely not straightforward and linear, however, this section involves the most relevant results from the developed protocol, with more detailed information found in Differentiation protocol. The results start with the cell expansion and the alternative coating results, followed by the viability of the MNPs after being cryopreserved, the differentiation to MNs and its characterization by immunostaining and calcium imaging.

5.2.1 Coating and cell expansion

The goal of this subsection was to establish a cell proliferation protocol for the MNPs and assess an alternative substrate coating for such protocol. This was necessary to keep the Axol's MNPs longer for different experiments instead of acquiring a new vial each time. Axol bioscience, at the time of writing, does not provide any maintenance or proliferation protocol for their MNPs, though they used to offer this service along with specific media and coating products for such expansion. As such, the MNEM and Geltrex coatings were developed.

First, the expansion protocol was able to successfully maintain the MNPs and proliferate while maintaining their differentiation potential, brightfield images seen on **Figure 5-1**. This was the keystone work for this section, since all subsequent experimentation hinged on the success of this goal. On the figure below, the MNPs were originally seeded at a density of 120k cells/cm^2 and were able to expand and form colonies of MNPs. In Differentiation protocol, it can be further seen the effects of longer cultures forming monolayer of MNPs and the effects of density for expansion (and differentiation). In summary, an expansion protocol was successfully established, and it allowed for the development of the differentiation and cryopreservation protocols found in the rest of this chapter.

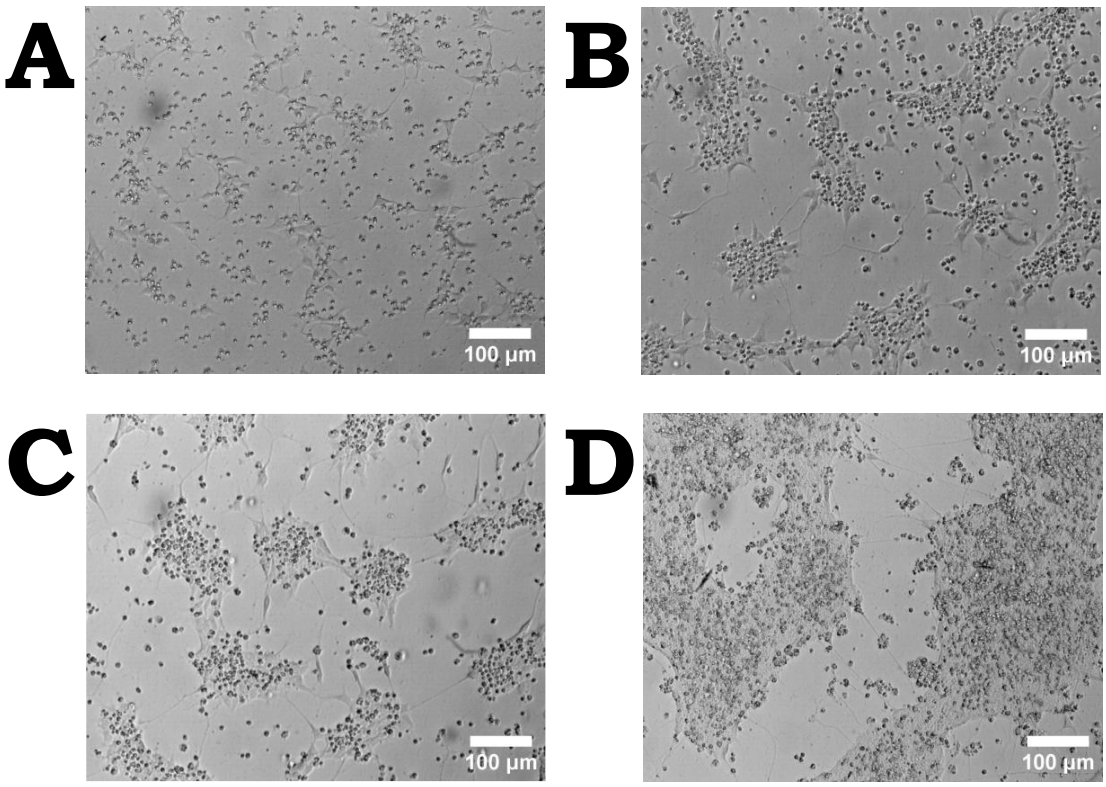

Figure 5-1. Evolution of MNPs expanded on a 24-well plate for DIV A) 1, B) 2, C) 3 and D) 6.

Then, it was observed that for expansion the Geltrex coating performed better for longer cultures than the Poly-D-Lysine and Vitronectin (PDL-VTN) coating recommended by Axol Biosciences. It can be seen in **Figure 5-2** that the wells coated with PDL-VTN had disastrous results with cell detachment starting to be seen at DIV 5 and being rampant at DIV 7, unlike the Geltrex-coated wells. This was quantified by counting the cells on each well, **Figure 5-3**, and a significant difference was found in the cell increase between the coatings at DIV 7. For these results, it was decided to continue with Geltrex for the coating of MNPs for cell expansion purposes. In conclusion, a protocol for expanding the MNPs was established with an additional coating protocol for such expansion to take place without significant cell losses within one week of seeding.

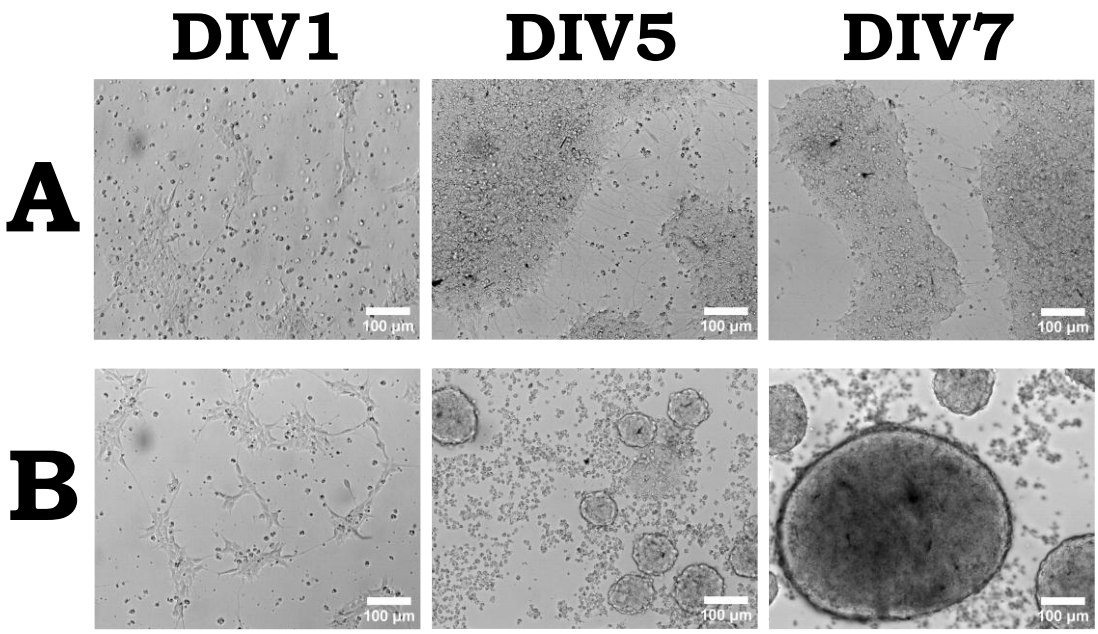

Figure 5-2. Evolution of MNPs expanded on a 24-well plate with A) Geltrex or B) PDL-VTN as a coating substrate.

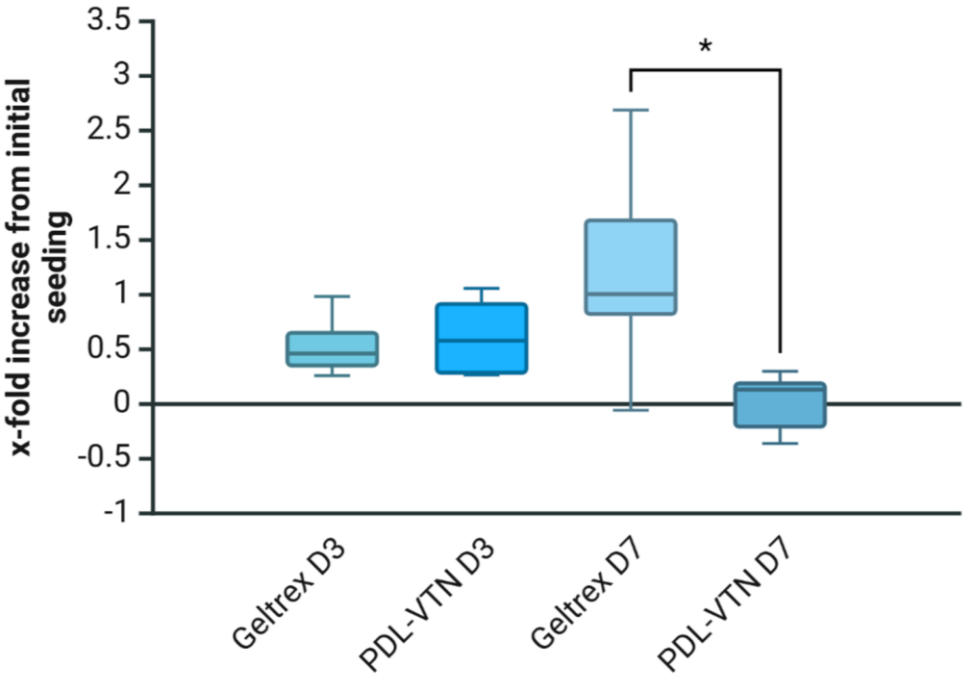

Figure 5-3. Box and whiskers plot showing the increase of number of cells relative to the seeding density. * $p<0.05$ two-way ANOVA Tukey post-hoc.

5.2.2 Cryopreservation and thawing

Cryopreservation of the MNPs was also explored to further improve the MN protocol, as storing the neurons for significantly later timepoints for experimentation was desired. After an initial successful

expansion of the MNPs, four cryovials were stored and three were thawed back. To assess the performance of the cryopreservation, it was compared to the cell viability of the original cryovial given by Axol Bioscience, whose protocol and materials are unknown, according to the cell counter used, the results are shown in **Figure 5-4**. It is worth noting that the data for this plot was retrieved before the plating of the cells, as such, each point represents two measurements instead of the usual ≥3 for the rest of the plots in this section.

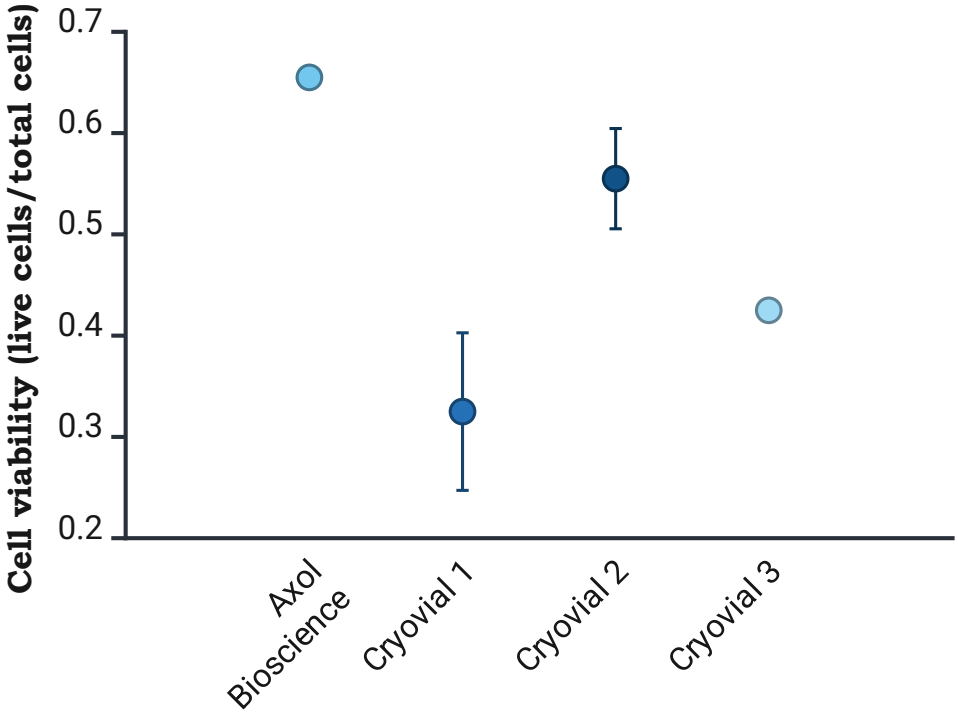

Figure 5-4. Plot of the cell survival rate after thawing.

Another point of interest for the cryopreservation protocol was the expansion and differentiation performance of the MNPs after a new freezing and thawing cycle. For the proliferation potential maintenance, **Figure 5-5** clearly shows a drop after cryopreservation. However, the MNPs are still able to proliferate and expand, which meets the goal of this section. For differentiation, it is best to see MN differentiation, but in short, the MNPs were able to differentiate into MNs. In summary, a cryopreservation protocol for MNPs was established that could preserve Axol's MNPs for further proliferation and differentiation at later timepoints, though optimization is still recommended as a future direction (see discussion below).

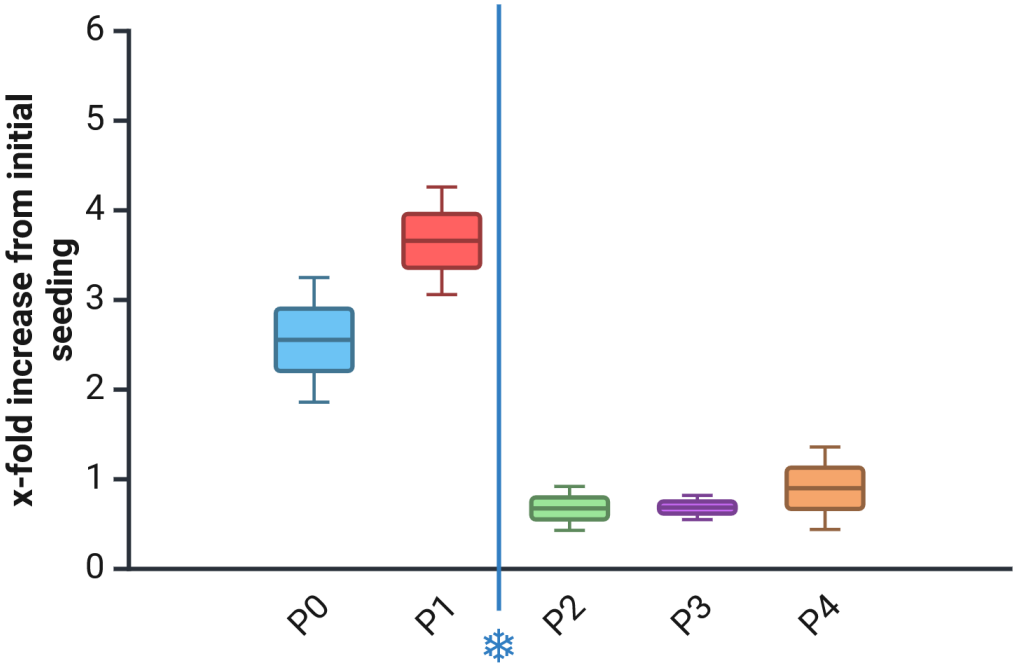

Figure 5-5. Increase of cell number per passage, normalized to seeding density. ❄ sets when the cryopreservation was done.

5.2.3 MN differentiation

Finally, a protocol with a chemically defined medium was established for the differentiation of the MNPs into MNs. For this section, it was possible to compare the results done in this work directly with the commercially available protocol established by Axol bioscience. **Figure 5-6** shows brightfield images of both protocols head-to-head and the morphological development of the MNs share similar traits. It was the quantified in **Figure 5-7** the thickness of the neurite growth to measure the maturation stage of the MNs and the robustness of the protocol. All in all, the established protocol resulted in morphologically different neurons compared to the MNPs and hinted heavily at MN differentiation, the confirmation of which was explored with immunostaining and calcium imaging.

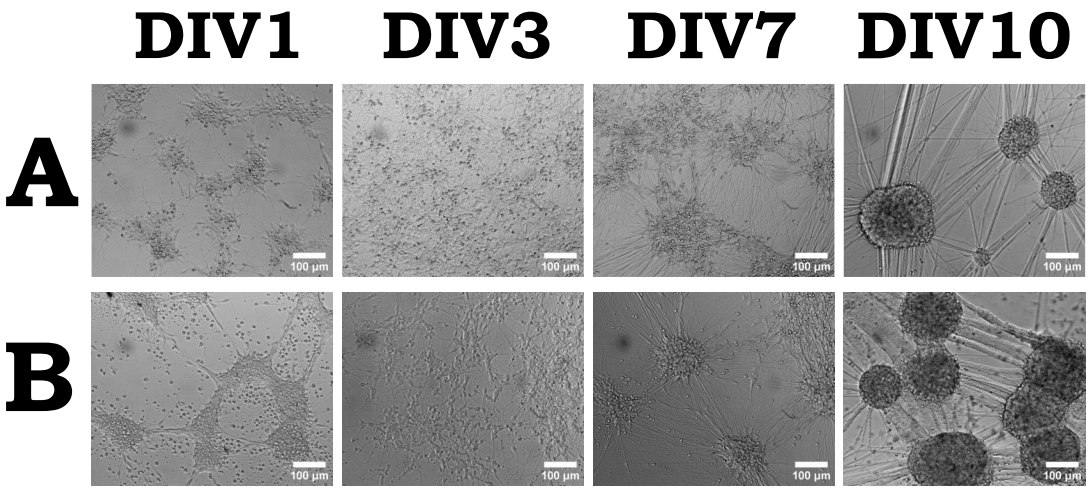

Figure 5-6. Differentiation of MNPs in a 96-well plate cultured with A) Axol's medium or B) MNDMM for different DIV.

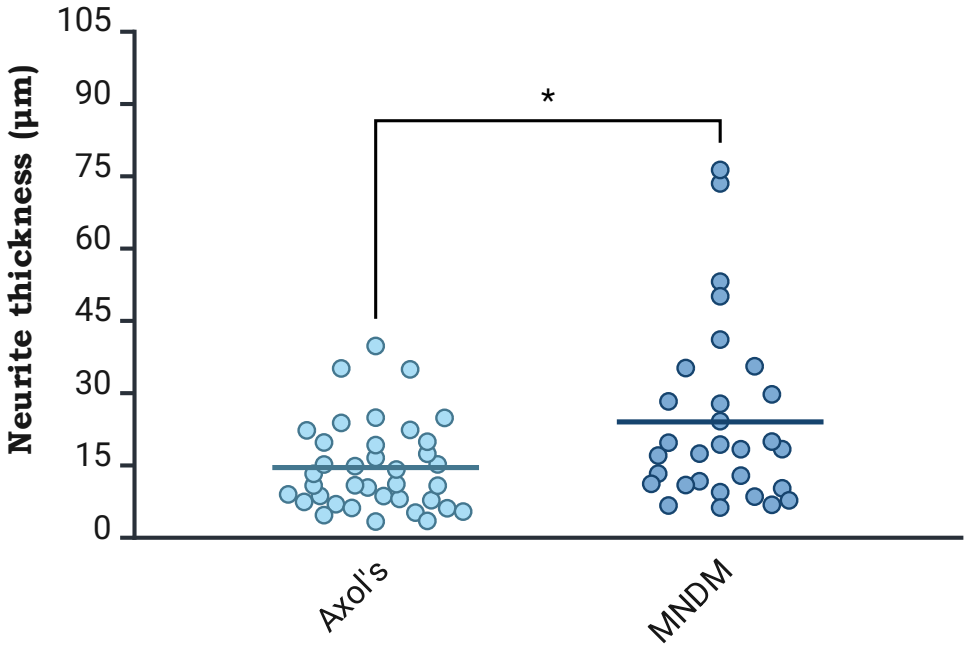

Figure 5-7. Mean line plot showcasing differences in motor neuron neurite thickness between differentiation media at DIV10. * p<0.05 non-parametric Mann-Whitney U-test.

The differentiation protocol was assessed by immunostaining, specifically for MAP2, which stains for the Microtubule Associated-Protein 2 a neuronal differentiation marker [109]. **Figure 5-8** and **Figure 5-9** show the immunostaining for the neuronal cultures using the Axol protocol and the protocol of this work, respectively. It is apparent in those figures that the neuronal cultures detached from the surface and started to agglomerate and lose axonal length; this was an issue seen throughout the development of the protocol and it was exacerbated at the moment of fixing and staining the cells themselves. So, it could be that at the start of the fixing procedure the MNs looked as in **Figure 5-6**, but by the end the

cells would have detached after all the washes and staining, indicating that there is a need to optimize the coating for differentiated cells (consensus with peers suggests a challenging task).Nevertheless, a neuronal network was imaged with the MAP2 staining that showed the correct differentiation, for the Axol protocol, on **Figure 5-10**, but not for the protocol in this work. While it is unfortunate that the neural network from the MNDM protocol was not nicely stained with MAP2, it is speculated that considering the morphological similarities between the protocols in the brightfield images and the fact that the marker was stained for the detached neural network, the current protocol can achieve differentiated MNs with MAP2 expression.

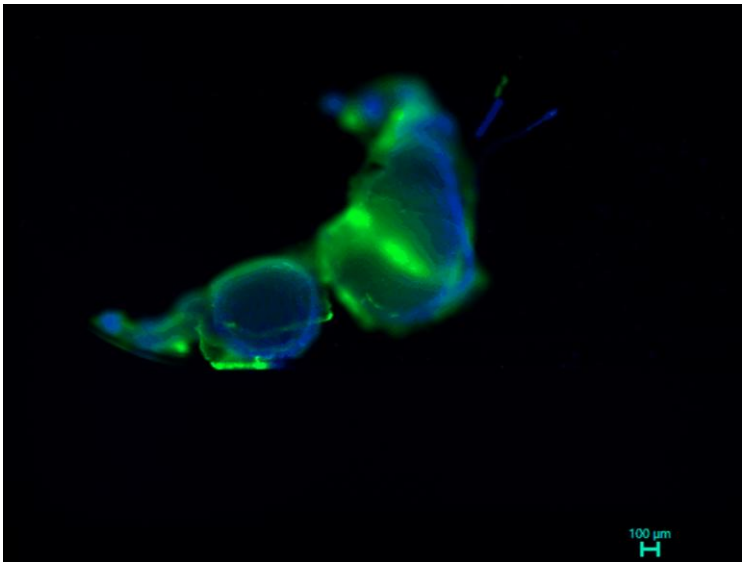

Figure 5-8. Axol protocol cells differentiated at DIV13. Green is MAP2 (neurofilaments) and blue is DAPI (nuclei).

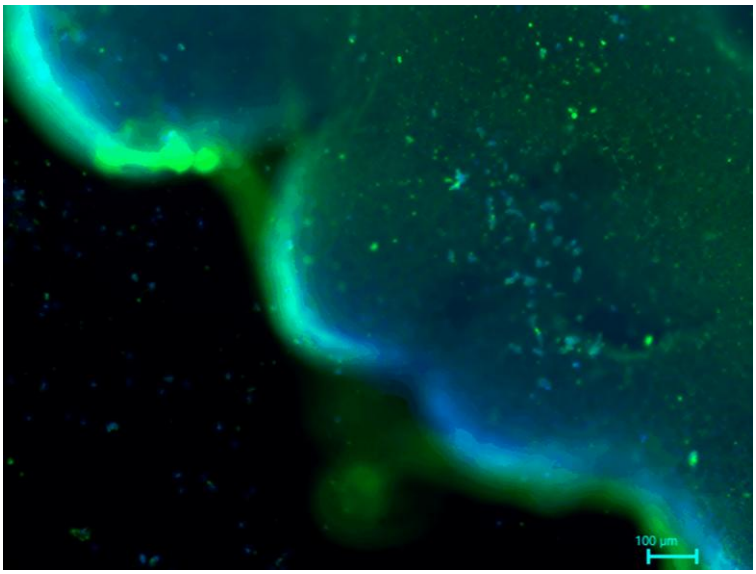

Figure 5-9. MNDM protocol cells differentiated at DIV13. Green is MAP2 (neurofilaments) and blue is DAPI (nuclei).

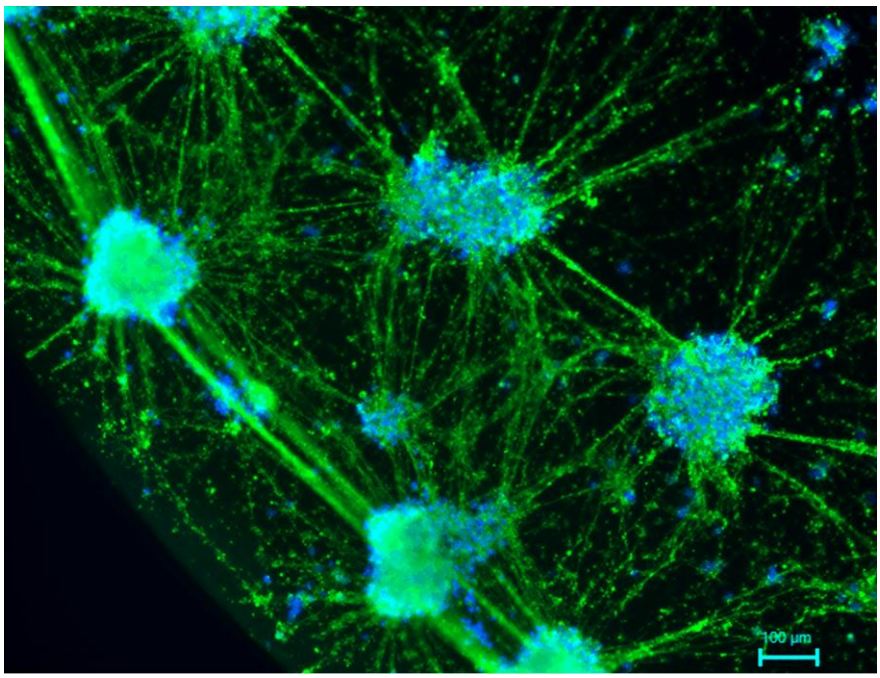

Figure 5-10. Axol protocol cells differentiated at DIV 10. Green is MAP2 (neurofilaments) and blue is DAPI (nuclei).

Finally, the differentiation of the MNPs was further characterized by their electrical activity. This was done with calcium imaging as mentioned before and spontaneous electrical activity was detected for both the Axol Bioscience's protocol and the protocol of this work, seen on **Figure 5-11** and **Figure 5-12** respectively. In those figures, it was possible to observe single cell firing in both conditions, but in the present protocol, synchronous and low-frequency network firing was observed. This behavior was not fully characterized with the calcium imaging, but a remnant can be seen in the normalized intensity values of **Figure 5-12** were a clear descending slope in the signal that is caused by the "cooling" of the synchronous firing. In summary, a differentiation protocol was established in this work that produced MNs with spontaneous activity.

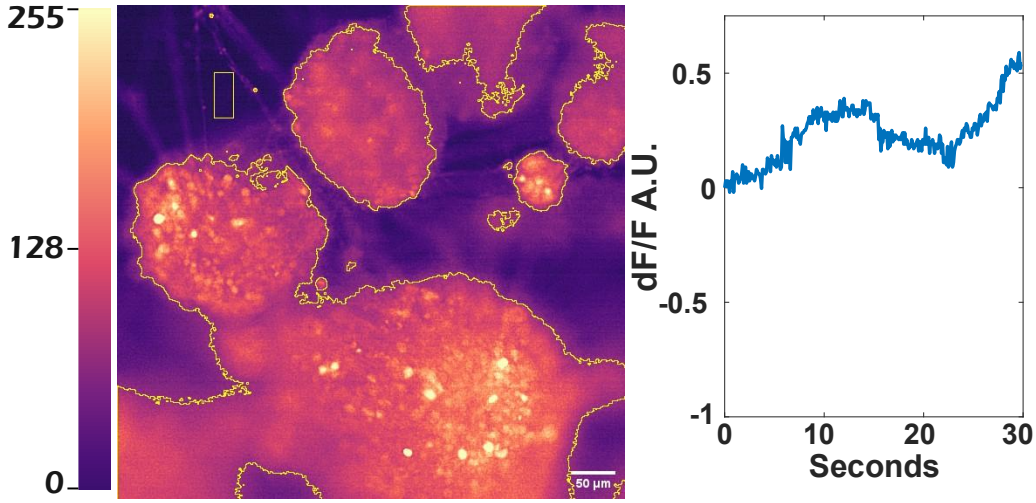

Figure 5-11. Axol bioscience protocol cells differentiated at DIV 10. Left indicates intensity normalized to background (yellow box) with arbitrary units. Intensity of calcium denoted by bright yellow (high intensity) to

deep purple (low intensity). Right is the timeline of the intensity of the calcium imaging normalized to the background.

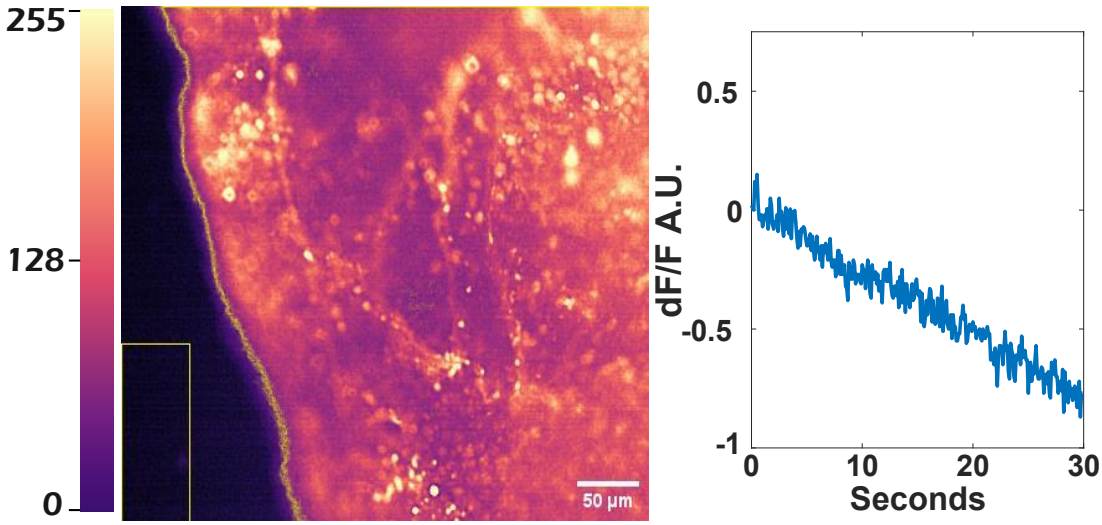

Figure 5-12. MNDM protocol cells differentiated at DIV10. Left indicates intensity normalized to background (yellow box) with arbitrary units. Intensity of calcium denoted by bright yellow (high intensity) to deep purple (low intensity). Right is the timeline of the intensity of the calcium imaging normalized to the background.

5.3 Discussion

5.3.1 Coating

Neuronal cell attachment is an active field of research, particularly due to the unreliability of adhesion on traditional culture materials [110]. Both substrate and coating choice have a profound impact on the attachment of the cells. While the coating goal was only to allow the MNPs to proliferate without differentiation taking place, it is important to address the detachment observed with the differentiated MNs. This effect was unfortunately seen quite commonly and threatened the MN characterization by making them quite vulnerable to the washing steps for calcium imaging and immunostaining, as seen in **Figure** 5-8 **Figure 5-9** and on the Differentiation protocol. This problem must be sufficiently solved, particularly for the electrophysiological recordings with MEAs.

On one hand, the properties of the substrate material (the labware used for culture, e.g. petri dish) affect the general culture of the cells and are usually glass or polymer-based (usually polystyrene), both of which were available for this thesis. Glass as a material is suited for microscopy and MEA technology, thanks to its optical properties; however, glass also has a great mechanical mismatch with native tissue, leading to detachment and aggregation issues. Meanwhile, polymer-based substrates are well demonstrated to be preferred by neuronal cultures and better suited for long term cultures, with tissue culture-treated polystyrene having detachment 5 weeks after plating compared to 1 week with standard glass [110]. Yet, they have suboptimal optical properties when compared to glass. Nevertheless, there are options for research, since multi-material substrates have been demonstrated to work and even other materials such as silicon and metals could be used for in vitro applications [111].

On the other hand, the selection for the coating is incredibly wide and broad, with extracellular matrix-derived peptides such as laminin, Matrigel, fibronectin, and Geltrex popular for culture along with other proteins with charge interactions such as poly-lysine . With so many materials that themselves can be further tuned and tweaked, it is no surprise that there is a great interest in this field to not only perfect the coatings for neural progenitors, but also for specific neuron types or more complex brain tissue

models. But one approach that is interesting for the themes touched in this thesis is the use of electroactive coatings by using conductive polymers such as polypyrrole, polyaniline, poly(vinylidene fluoride), and, of course, PEDOT:PSS, that can produce favourable adhesion and can guide axonal growth [112], [113], [114]. While not necessarily a perfect substrate for attachment, it just needs to be good enough for the differentiation and maturation of the MNs without detachment, while also serving as electrodes to record their electrophysiology.

While here is suggested to use these approaches as a launching pad for a coating optimization, ultimately, the results for this thesis are also affected by the training for and handling of the neuronal cultures themselves, which despite the best efforts might have inadvertently been suboptimal to not have them detach. Ultimately, optimizing coating for neuronal cultures is no quick side-research and requires a great deal of research and work to advance the field.

5.3.2 Cryopreservation

The cryopreservation approach used in this protocol is based on the cryoprotective agent dimethyl-sulfoxide (DMSO) along with a slow-freezing process (1-2°C cooling rate). Since the goal of this section was to *establish* a cryopreservation protocol in absence of one available for this specific cell line, there is room for optimization. This is evident with the results from **Figure 5-4**, showing clear differences in cell viability. Though the cryopreservation medium used by Axol Bioscience was not immediately available, it is also suspected to contain DMSO, as per the instructions given for the MNPs and its wide adoption. One way to assess the effectiveness of the freeze/thaw process is to see the recovery of the vial, as shown below:

$$Recovery = \frac{Cells_{alive}}{Cells_{frozen}}$$

Equation 3- Recovery from thawing equation [115]..

This method allows for the quantification of cryopreservation-induced apoptosis/death right after thawing the cryovial. A comparison was made between the recovery results of the Cryo-SFM and other cryopreservation media for stem cell-derived neuron progenitor cells [116]. The compared media are as follows: SCB (STEM-CELLBANKER®, Amsbio), SYF (Synth-a-Freeze™ Medium, Thermo Fisher), PSC (PSC Cryopreservation medium, Thermo Fisher), CS10 (CryoStor® CS10 Freeze Medium, BioLife Solutions), CS5 (CryoStor® CS5 Freeze Medium, BioLife Solutions), and CV (Cellvation Cryopreservation Medium, MP Biomedicals). These media were used as references because they contain DMSO as their cryoprotective agent, just as Cryo-SFM, except for CV, who still had a respectable recovery rate as seen in **Figure 5-13**.

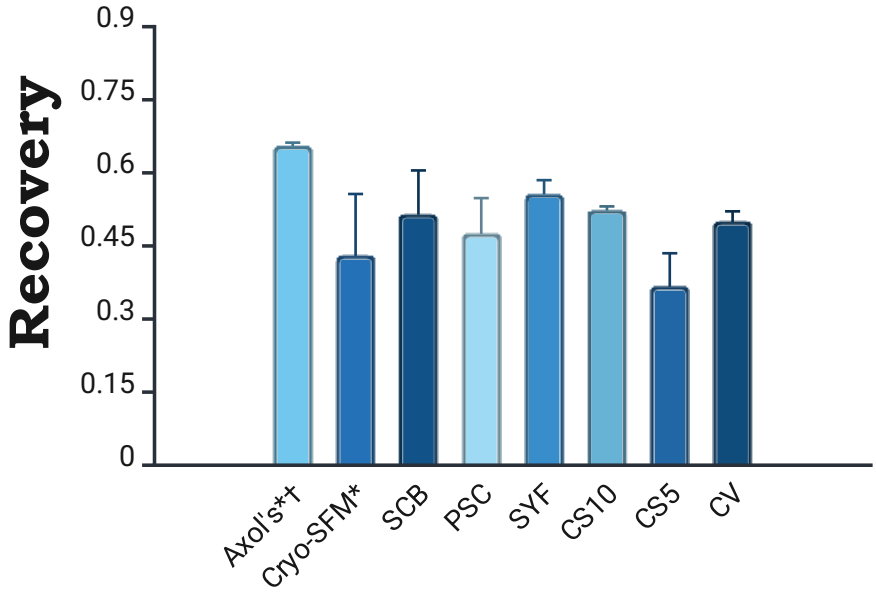

Figure 5-13. Recovery rates of different cryopreservation media. * this work. † viability (live cells/total cells) since initial seeding unknown.

This serves to illustrate the different options one has to optimize the cryopreservation protocol established, and it is worth noting that the viability values usually drop after 24 hours from plating (when attached to their substrate) [116]. This is a common effect for slow-freezing methods that contain cryoprotective agents, though not necessarily an absolute one for all cryopreservation methods. For example, vitrification uses a fast-freezing process (10,000°C cooling rate) by cooling the cells from room temperature to -196°C in ~2 seconds and can actually yield more cells in 24 hours after thawing than originally plated, for both iPSCs and MNPs [115], [117]. This method requires specialized equipment and training, and usually handles a much lower cell volume, preventing them from wider adoption. Finally, alternatives to DMSO, like ice recrystallization inhibitors, adding ROCK inhibitor, or tweaking the cooling rate present different strategies to optimize the present cryopreservation protocol, that could perhaps even work for matured MNs [116], [117], [118].

5.3.3 Differentiation

The differentiation protocol present achieved results that suggest MN differentiation from the MNPs using the present chemically defined media and methods compared to a commercially available protocol. This conclusion was reached due to the morphological changes, immunostaining for MN markers, and neuronal firing as observed with calcium imaging. In addition, the neurites of the present protocol grew thicker than their Axol Bioscience counterparts, and thicker neurites have been used to indicate robustness in MN development [119]. With the calcium imaging figures, it is possible to observe spontaneous activity of the neuronal culture, indicating functionalization of the neurons. Since calcium is used in many cellular processes, the best way to properly showcase the functionalization of the neurons is through electrical measurements, hence the need for MEA technology. Though neurons firing were recorded, *.gif* files found in the Differentiation protocol, the measurement can be improved upon by introducing controls, for example, introducing a bolus of KCl to achieve the highest signal possible by opening voltage-gated calcium channels and have a benchmark to compare the spontaneous activity to [120], or introducing drugs that prevent neuronal activity in vitro, such as tetrodotoxin [121].

Finally, the characterization of the MN differentiation can be further improved with techniques that can better quantify the extent of the differentiation. Following the paper which this protocol is based on [108], a first approach would be the inclusion of a polymerase chain reaction (PCR) assay or one of its derivatives, such as quantitative PCR or reverse transcription PCR. In short, PCR assays work by cyclically amplifying specific sections of DNA or RNA exponentially [122]. By selecting certain expressed genes, it is possible to verify the cell identity and function, that is, discern if cells are MNPs or MNs. It is hereby suggested to follow the selection made by [108] of gene-expression markers: *NANOG, SOX2* and *PAX6* for neural stem cells; *OLIG2* for MNPs; *ISL1, CHAT, RBFOX3, VACHT,* and *NFH* for MNs; and *SYN1/SYNAPSIN* and *MAP2* for mature MNs. Furthermore, these markers can also be used for immunostaining, just as was done on the **Figure** 5-8**, Figure** 5-9**, and Figure** 5-10 with the MAP2 marker. More interestingly, these markers can serve to more accurately quantify the number of differentiated MNs using a flow cytometer, that can have single-cell resolution for identification. As such, the differentiation yield can be extracted to better characterize the present protocol, along with the aforementioned improvements.

5.4 MNP protocol conclusion and future

The work done in this chapter resulted in an expansion, cryopreservation, and differentiation protocol for MNPs into MN cultures with success. Nevertheless, as always, there is room for improvements. Naturally, optimization is needed to find the optimal cell density, coating recipe, media change timeline, and/or differentiation factors parameters to bring about the most robust MN culture. None of these examples are trivial and each requires much effort and planning to produce the robust results. However, for the protocol established in this work, there needs to be an even more robust method for characterizing the MN cultures. This is further explained in the following bullet list.

- PCR and/or derivatives: polymerase chain reaction is great to establish if a cell has expressed a certain protein that can help identify how much potential proliferation a cell has. Furthermore, this technique allows the exploration of proteins that are only found in MNPs and MNs. Adding this assay to the current protocol will help quantify and clarify the properties of the cells as they change through time, passage, and freezing/thawing cycles.
- For calcium imaging, it is possible to stimulate the cells, see Differentiation protocol, to observe their response, but there needs to be rigorous controls. For a positive control, a bolus of KCl would help normalize the stimulus response to the maximum response possible of the tested cells. Meanwhile for a negative control it is possible to use tetrodotoxin as an inhibitor of neuronal activity.
- Keeping in the same line as electrophysiological characterization, it is no surprise that using an MEA to also observe the spontaneous activity is a relevant option for this protocol. With an MEA, it is possible to quantify the electrical activity directly instead of using calcium as a proxy for electrical activity.
- Introduce and explore PEDOT:PSS-based coatings that can affect the development of the neurons thanks to their neurogenic properties.

In conclusion, to better develop the current protocol, more robust characterization methods are preferred as a first step towards optimization since this would establish more repeatable and reproducible results.

6 Conclusions and future directions

6.1 Concluding remarks

PEDOT:PSS is a well-established organic conductive polymer that has a developing role for neural interface due to its mixed ionic-electronic conductivity that can bridge the gap between the tissue and the electronics, an excellent material for bioelectronics. The main objective of this thesis was to investigate this claim and answer: **How can PEDOT:PSS be used for the development of neuronal cultures?**

In short, PEDOT:PSS can be used for the culture of iPSC-derived neuronal cultures and recording the electrical activity of said cultures for assessing maturation. Throughout this thesis, lessons and insights were learned from working with and investigating PEDOT:PSS. First, the literature review served as a starting point to better understand the polymer and its working mechanisms, while presenting current trends in using such material. Then, practical experience was made by fabricating PEDOT:PSS and culturing cortical neurons to assess the biocompatibility of the polymer. Additionally, an acetic acid treatment was performed to demonstrate conductivity enhancements of the material. Next, in vitro recordings of cortical neurons were performed after maturation of the cells, though no stimulation was performed. In that chapter, it is delved into the analysis and interpretation of the recorded signals, to have a more rounded understanding in neuronal electrophysiology. Finally, a differentiation protocol of motor neurons was established using iPSC-derived motor neuron progenitors, though unfortunately PEDOT:PSS could not be integrated in the protocol.

As for the specific objectives:

- The electrochemical mechanisms that make PEDOT:PSS such a coveted material are thoroughly discussed in this thesis
- PEDOT:PSS films and electrodes were validated as a neuronal interface by showing biocompatibility and allowing for the maturation of neuronal cultures to generate action potentials that could be recorded with an MEA, though no stimulation of neuronal cells was achieved.
- Though a differentiation protocol was established, PEDOT:PSS could not be integrated in the protocol due to time constraints when developing the protocol.

In conclusion, this thesis has served to produce knowledge for PEDOT:PSS-based neuronal interfaces and electrophysiological recordings.

6.2 Future directions

Though discussed in each chapter, there are several directions to advance the work done here in a more cohesive way:

- Assessing the biocompatibility of acid treated PEDOT:PSS films.
    - This method can then serve to improve the electrochemical characteristics of MEAs with PEDOT:PSS electrodes, by assessing the impedance measurements at 1 kHz to improve sensitivity and the charge injection capacity for stimulation.
- Implementing PEDOT:PSS in the established motor neuron differentiation protocol to allow for the electrophysiological maturation of the cells.
    - For recordings, the spike detecting and sorting algorithms can be improved by implementing a normalized template method.

    - By implementing the polymer, it is also possible to explore the effect of electrical stimulation for the development of the neurons.
    - As discussed before, the protocol should also be improved by implementing more robust methods for differentiation and maturation, namely: PCR-based assays and normalization of calcium imaging.

These are recommendations made following the experiences had in this thesis, however, different approaches can be made to answer the main question that can serve to start new future works. Some possible examples include:

- 3D neuronal cultures by integrating PEDOT:PSS into a 3D structure.
- Integrating PEDOT:PSS in microfluidic devices to have a much more controlled environment for cell culture.

Bibliography

[1] B. Alberts, A. Johnson, J. Lewis, M. Raff, K. Roberts, and P. Walter, “Neural Development,” in *Molecular Biology of the Cell. 4th edition*, Garland Science, 2002. Accessed: June 28, 2025. [Online]. Available: https://www.ncbi.nlm.nih.gov/books/NBK26814/

[2] I. Chen and F. Lui, “Neuroanatomy, Neuron Action Potential,” in *StatPearls*, Treasure Island (FL): StatPearls Publishing, 2025. Accessed: July 21, 2025. [Online]. Available: http://www.ncbi.nlm.nih.gov/books/NBK546639/

[3] F. Bezanilla, “The action potential: From voltage-gated conductances to molecular structures,” *Biol. Res.*, vol. 39, no. 3, pp. 425–435, 2006, doi: 10.4067/S0716-97602006000300005.

[4] A. A. Galakhova *et al.*, “Evolution of cortical neurons supporting human cognition,” *Trends Cogn. Sci.*, vol. 26, no. 11, pp. 909–922, Nov. 2022, doi: 10.1016/j.tics.2022.08.012.

[5] K. Campbell, “Cortical Neuron Specification: It Has Its Time and Place,” *Neuron*, vol. 46, no. 3, pp. 373–376, May 2005, doi: 10.1016/j.neuron.2005.04.014.

[6] L. C. Zayia and P. Tadi, “Neuroanatomy, Motor Neuron,” in *StatPearls*, Treasure Island (FL): StatPearls Publishing, 2025. Accessed: Mar. 28, 2025. [Online]. Available: http://www.ncbi.nlm.nih.gov/books/NBK554616/

[7] A. D. Gitler, P. Dhillon, and J. Shorter, “Neurodegenerative disease: models, mechanisms, and a new hope,” *Dis. Model. Mech.*, vol. 10, no. 5, pp. 499–502, May 2017, doi: 10.1242/dmm.030205.

[8] P. Maresova, J. Hruska, B. Klimova, S. Barakovic, and O. Krejcar, “Activities of Daily Living and Associated Costs in the Most Widespread Neurodegenerative Diseases: A Systematic Review,” *Clin. Interv. Aging*, vol. 15, pp. 1841–1862, Oct. 2020, doi: 10.2147/CIA.S264688.

[9] J. D. Steinmetz *et al.*, “Global, regional, and national burden of disorders affecting the nervous system, 1990–2021: a systematic analysis for the Global Burden of Disease Study 2021,” *Lancet Neurol.*, vol. 23, no. 4, pp. 344–381, Apr. 2024, doi: 10.1016/S1474-4422(24)00038-3.

[10] J. Van Schependom and M. D’haeseleer, “Advances in Neurodegenerative Diseases,” *J. Clin. Med.*, vol. 12, no. 5, Art. no. 5, Jan. 2023, doi: 10.3390/jcm12051709.

[11] K. Takahashi and S. Yamanaka, “Induction of Pluripotent Stem Cells from Mouse Embryonic and Adult Fibroblast Cultures by Defined Factors,” *Cell*, vol. 126, no. 4, pp. 663–676, Aug. 2006, doi: 10.1016/j.cell.2006.07.024.

[12] S. Mitalipov and D. Wolf, “Totipotency, Pluripotency and Nuclear Reprogramming,” in *Engineering of Stem Cells*, U. Martin, Ed., Berlin, Heidelberg: Springer, 2009, pp. 185–199. doi: 10.1007/10_2008_45.

[13] T. Sen and R. P. Thummer, “CRISPR and iPSCs: Recent Developments and Future Perspectives in Neurodegenerative Disease Modelling, Research, and Therapeutics,” *Neurotox. Res.*, vol. 40, no. 5, pp. 1597–1623, Oct. 2022, doi: 10.1007/s12640-022-00564-w.

[14] J. Cerneckis, H. Cai, and Y. Shi, “Induced pluripotent stem cells (iPSCs): molecular mechanisms of induction and applications,” *Signal Transduct. Target. Ther.*, vol. 9, no. 1, pp. 1–26, Apr. 2024, doi: 10.1038/s41392-024-01809-0.

[15] G. H. Kim *et al.*, “Recent Progress on Microelectrodes in Neural Interfaces,” *Materials*, vol. 11, no. 10, Art. no. 10, Oct. 2018, doi: 10.3390/ma11101995.

[16] T. Nezakati, A. Seifalian, A. Tan, and A. M. Seifalian, “Conductive Polymers: Opportunities and Challenges in Biomedical Applications,” *Chem. Rev.*, vol. 118, no. 14, pp. 6766–6843, July 2018, doi: 10.1021/acs.chemrev.6b00275.

[17] G. J. Stuart, H. U. Dodt, and B. Sakmann, “Patch-clamp recordings from the soma and dendrites of neurons in brain slices using infrared video microscopy,” *Pflüg. Arch.*, vol. 423, no. 5, pp. 511–518, June 1993, doi: 10.1007/BF00374949.

[18] S. Song, F. Fallegger, A. Trouillet, K. Kim, and S. P. Lacour, “Deployment of an electrocorticography system with a soft robotic actuator,” *Sci. Robot.*, vol. 8, no. 78, p. eadd1002, May 2023, doi: 10.1126/scirobotics.add1002.

[19] E. L. Foldes, D. M. Ackermann, N. Bhadra, K. L. Kilgore, and N. Bhadra, “Design, fabrication and evaluation of a conforming circumpolar peripheral nerve cuff electrode for acute experimental use,” *J. Neurosci. Methods*, vol. 196, no. 1, pp. 31–37, Mar. 2011, doi: 10.1016/j.jneumeth.2010.12.020.
[20] B. L. Robinette, J. A. Harrill, W. R. Mundy, and T. J. Shafer, “In Vitro Assessment of Developmental Neurotoxicity: Use of Microelectrode Arrays to Measure Functional Changes in Neuronal Network Ontogeny1,” *Front. Neuroengineering*, vol. 4, Jan. 2011, doi: 10.3389/fneng.2011.00001.
[21] C. Ning, Z. Zhou, G. Tan, Y. Zhu, and C. Mao, “Electroactive polymers for tissue regeneration: Developments and perspectives,” *Prog. Polym. Sci.*, vol. 81, pp. 144–162, June 2018, doi: 10.1016/j.progpolymsci.2018.01.001.
[22] A. Keirouz *et al.*, “Conductive Polymer-Coated 3D Printed Microneedles: Biocompatible Platforms for Minimally Invasive Biosensing Interfaces,” *Small*, vol. 19, no. 14, p. 2206301, Apr. 2023, doi: 10.1002/smll.202206301.
[23] S. Song *et al.*, “Electrical stimulation of human neural stem cells via conductive polymer nerve guides enhances peripheral nerve recovery,” *Biomaterials*, vol. 275, p. 120982, Aug. 2021, doi: 10.1016/j.biomaterials.2021.120982.
[24] A. V. Volkov *et al.*, “Understanding the Capacitance of PEDOT:PSS,” *Adv. Funct. Mater.*, vol. 27, no. 28, p. 1700329, July 2017, doi: 10.1002/adfm.201700329.
[25] A. Sanchez-Sanchez, I. del Agua, G. G. Malliaras, and D. Mecerreyes, “Chapter 6 - Conductive Poly(3,4-Ethylenedioxythiophene) (PEDOT)-Based Polymers and Their Applications in Bioelectronics,” in *Smart Polymers and their Applications (Second Edition)*, M. R. Aguilar and J. San Román, Eds., in Woodhead Publishing in Materials. , Woodhead Publishing, 2019, pp. 191–218. doi: 10.1016/B978-0-08-102416-4.00006-5.
[26] F. Jiang, “Chapter 1 - Short history of thermoelectric conjugated PEDOT development,” in *Advanced PEDOT Thermoelectric Materials*, F. Jiang, C. Liu, and J. Xu, Eds., in Woodhead Publishing Series in Electronic and Optical Materials. , Woodhead Publishing, 2022, pp. 1–38. doi: 10.1016/B978-0-12-821550-0.00008-1.
[27] E. Stavrinidou *et al.*, “Direct Measurement of Ion Mobility in a Conducting Polymer,” *Adv. Mater.*, vol. 25, no. 32, pp. 4488–4493, 2013, doi: 10.1002/adma.201301240.
[28] B. D. Paulsen, K. Tybrandt, E. Stavrinidou, and J. Rivnay, “Organic mixed ionic–electronic conductors,” *Nat. Mater.*, vol. 19, no. 1, pp. 13–26, Jan. 2020, doi: 10.1038/s41563-019-0435-z.
[29] J. F. Cavanagh, “Electrophysiology as a theoretical and methodological hub for the neural sciences,” *Psychophysiology*, vol. 56, no. 2, p. e13314, 2019, doi: 10.1111/psyp.13314.
[30] V. L. Feigin *et al.*, “The global burden of neurological disorders: translating evidence into policy,” *Lancet Neurol.*, vol. 19, no. 3, pp. 255–265, Mar. 2020, doi: 10.1016/S1474-4422(19)30411-9.
[31] K. L. Levine, D. E. Tallman, and G. P. Bierwagen, “Mott–Schottky analysis of aluminium oxide formed in the presence of different mediators on the surface of aluminium alloy 2024-T3,” *J. Mater. Process. Technol.*, vol. 199, no. 1, pp. 321–326, Apr. 2008, doi: 10.1016/j.jmatprotec.2007.08.023.
[32] A. S. Bondarenko and G. A. Ragoisha, “Variable Mott-Schottky plots acquisition by potentiodynamic electrochemical impedance spectroscopy,” *J. Solid State Electrochem.*, vol. 9, no. 12, pp. 845–849, Dec. 2005, doi: 10.1007/s10008-005-0025-7.
[33] L. Guo, “Recording Electrodes,” in *Principles of Electrical Neural Interfacing: A Quantitative Approach to Cellular Recording and Stimulation*, L. Guo, Ed., Cham: Springer International Publishing, 2022, pp. 17–31. doi: 10.1007/978-3-030-77677-0_3.
[34] C. J. Schwiening, “A brief historical perspective: Hodgkin and Huxley,” *J. Physiol.*, vol. 590, no. Pt 11, pp. 2571–2575, June 2012, doi: 10.1113/jphysiol.2012.230458.
[35] A. C. Lazanas and M. I. Prodromidis, “Electrochemical Impedance Spectroscopy─A Tutorial,” *ACS Meas. Sci. Au*, Mar. 2023, doi: 10.1021/acsmeasuresciau.2c00070.
[36] N. Elgrishi, K. J. Rountree, B. D. McCarthy, E. S. Rountree, T. T. Eisenhart, and J. L. Dempsey, “A Practical Beginner’s Guide to Cyclic Voltammetry,” ACS Publications. Accessed: Apr. 16, 2025. [Online]. Available: https://pubs.acs.org/doi/full/10.1021/acs.jchemed.7b00361
[37] L. Guan, L. Yu, and G. Z. Chen, “Capacitive and non-capacitive faradaic charge storage,” *Electrochimica Acta*, vol. 206, pp. 464–478, July 2016, doi: 10.1016/j.electacta.2016.01.213.
[38] “Can anyone explain how area under the Cyclic Potentiodynamic polarization curve gives charge?,” ResearchGate. Accessed: June 29, 2025. [Online]. Available:

https://www.researchgate.net/post/Can_anyone_explain_how_area_under_the_Cyclic_Potentiodynamic_polarization_curve_gives_charge
[39] R. A. Green *et al.*, “Laser patterning of platinum electrodes for safe neurostimulation,” *J. Neural Eng.*, vol. 11, no. 5, p. 056017, Sept. 2014, doi: 10.1088/1741-2560/11/5/056017.
[40] S. Van Reenen, M. Scheepers, K. Van De Ruit, D. Bollen, and M. Kemerink, “Explaining the effects of processing on the electrical properties of PEDOT:PSS,” *Org. Electron.*, vol. 15, no. 12, pp. 3710–3714, Dec. 2014, doi: 10.1016/j.orgel.2014.10.029.
[41] C. Nick, C. Thielemann, and H. F. Schlaak, “PEDOT:PSS coated gold nanopillar microelectrodes for neural interfaces,” in *2014 International Conference on Manipulation, Manufacturing and Measurement on the Nanoscale (3M-NANO)*, Oct. 2014, pp. 160–165. doi: 10.1109/3M-NANO.2014.7057309.
[42] B. Lu *et al.*, “Pure PEDOT:PSS hydrogels,” *Nat. Commun.*, vol. 10, no. 1, p. 1043, Mar. 2019, doi: 10.1038/s41467-019-09003-5.
[43] Y. J. Lee, Y. H. Kim, and E. K. Lee, “PEDOT:PSS-Based Prolonged Long-Term Decay Synaptic OECT with Proton-Permeable Material, Nafion,” *Macromol. Rapid Commun.*, vol. 45, no. 17, p. 2400165, 2024, doi: 10.1002/marc.202400165.
[44] L. Groenendaal, F. Jonas, D. Freitag, H. Pielartzik, and J. R. Reynolds, “Poly(3,4-ethylenedioxythiophene) and Its Derivatives: Past, Present, and Future,” *Adv. Mater.*, vol. 12, no. 7, pp. 481–494, 2000, doi: 10.1002/(SICI)1521-4095(200004)12:7<481::AID-ADMA481>3.0.CO;2-C.
[45] E. Hosseini, V. Ozhukil Kollath, and K. Karan, “The key mechanism of conductivity in PEDOT:PSS thin films exposed by anomalous conduction behaviour upon solvent-doping and sulfuric acid post-treatment,” *J. Mater. Chem. C*, vol. 8, no. 12, pp. 3982–3990, 2020, doi: 10.1039/C9TC06311K.
[46] N. Ahmad Shahrim, Z. Ahmad, A. W. Azman, Y. F. Buys, and N. Sarifuddin, “Mechanisms for doped PEDOT:PSS electrical conductivity improvement,” *Mater. Adv.*, vol. 2, no. 22, pp. 7118–7138, 2021, doi: 10.1039/D1MA00290B.
[47] “Understanding the Capacitance of PEDOT:PSS - Volkov - 2017 - Advanced Functional Materials - Wiley Online Library.” Accessed: June 29, 2025. [Online]. Available: https://advanced.onlinelibrary.wiley.com/doi/full/10.1002/adfm.201700329
[48] Y. Li *et al.*, “Boosting the Performance of PEDOT:PSS Based Electronics Via Ionic Liquids,” *Adv. Mater.*, vol. 36, no. 13, p. 2310973, 2024, doi: 10.1002/adma.202310973.
[49] R. Green and M. R. Abidian, “Conducting Polymers for Neural Prosthetic and Neural Interface Applications,” *Adv. Mater.*, vol. 27, no. 46, pp. 7620–7637, 2015, doi: 10.1002/adma.201501810.
[50] M. C. Salvadori, A. R. Vaz, L. L. Melo, and M. Cattani, “Nanostructured Gold Thin Films: Young Modulus Measurement,” *Surf. Rev. Lett.*, vol. 10, no. 04, pp. 571–575, Aug. 2003, doi: 10.1142/S0218625X03005323.
[51] C. T. McKee, J. A. Last, P. Russell, and C. J. Murphy, “Indentation Versus Tensile Measurements of Young’s Modulus for Soft Biological Tissues,” *Tissue Eng. Part B Rev.*, vol. 17, no. 3, pp. 155–164, June 2011, doi: 10.1089/ten.teb.2010.0520.
[52] C. W. magazine Nature, “A Cubic Millimeter of a Human Brain Has Been Mapped in Spectacular Detail,” Scientific American. Accessed: June 29, 2025. [Online]. Available: https://www.scientificamerican.com/article/a-cubic-millimeter-of-a-human-brain-has-been-mapped-in-spectacular-detail/
[53] C. Stadelmann, S. Timmler, A. Barrantes-Freer, and M. Simons, “Myelin in the Central Nervous System: Structure, Function, and Pathology,” *Physiol. Rev.*, vol. 99, no. 3, pp. 1381–1431, July 2019, doi: 10.1152/physrev.00031.2018.
[54] J. Pas *et al.*, “Neurospheres on Patterned PEDOT:PSS Microelectrode Arrays Enhance Electrophysiology Recordings,” *Adv. Biosyst.*, vol. 2, no. 1, 2018, doi: 10.1002/adbi.201700164.
[55] D. A. Koutsouras *et al.*, “PEDOT:PSS microelectrode arrays for hippocampal cell culture electrophysiological recordings,” *MRS Commun.*, vol. 7, no. 2, pp. 259–265, June 2017, doi: 10.1557/mrc.2017.34.
[56] K. Wang *et al.*, “Electrodeposition of alginate with PEDOT/PSS coated MWCNTs to make an interpenetrating conducting hydrogel for neural interface,” *Compos. Interfaces*, vol. 26, no. 1, pp. 27–40, Jan. 2019, doi: 10.1080/09276440.2018.1465766.

[57] S. Asgarifar, P. M. C. Inácio, A. L. G. Mestre, and H. L. Gomes, “Ultrasensitive bioelectronic devices based on conducting polymers for electrophysiology studies,” *Chem. Pap.*, vol. 72, no. 7, pp. 1597–1603, July 2018, doi: 10.1007/s11696-018-0481-z.
[58] S. Carli *et al.*, “Single walled carbon nanohorns composite for neural sensing and stimulation,” *Sens. Actuators B Chem.*, vol. 271, pp. 280–288, Oct. 2018, doi: 10.1016/j.snb.2018.05.083.
[59] E. Tomaskovic-Crook *et al.*, “Human Neural Tissues from Neural Stem Cells Using Conductive Biogel and Printed Polymer Microelectrode Arrays for 3D Electrical Stimulation,” *Adv. Healthc. Mater.*, vol. 8, no. 15, 2019, doi: 10.1002/adhm.201900425.
[60] Z. Aqrawe *et al.*, “A simultaneous optical and electrical in-vitro neuronal recording system to evaluate microelectrode performance,” *PLoS ONE*, vol. 15, no. 8 August, 2020, doi: 10.1371/journal.pone.0237709.
[61] E. He *et al.*, “MWCNTs/PEDOT:PSS nanocomposites-modified microelectrode array for spatial dynamics recording of epileptic discharges in multi-subregion of hippocampal slice,” *Sens. Actuators B Chem.*, vol. 329, p. 129190, Feb. 2021, doi: 10.1016/j.snb.2020.129190.
[62] E. He *et al.*, “Sensitive detection of electrophysiology and dopamine vesicular exocytosis of hESC-derived dopaminergic neurons using multifunctional microelectrode array,” *Biosens. Bioelectron.*, vol. 209, p. 114263, Aug. 2022, doi: 10.1016/j.bios.2022.114263.
[63] T. L. Li *et al.*, “Stretchable mesh microelectronics for the biointegration and stimulation of human neural organoids,” *Biomaterials*, vol. 290, p. 121825, Nov. 2022, doi: 10.1016/j.biomaterials.2022.121825.
[64] P. D. Donaldson and S. L. Swisher, “Transparent, Low-Impedance Inkjet-Printed PEDOT:PSS Microelectrodes for Multimodal Neuroscience,” *Phys. Status Solidi Appl. Mater. Sci.*, vol. 219, no. 10, 2022, doi: 10.1002/pssa.202100683.
[65] A. Lunghi *et al.*, “Flexible Neural Interfaces Based on 3D PEDOT:PSS Micropillar Arrays,” *Adv. Mater. Interfaces*, vol. 9, no. 25, 2022, doi: 10.1002/admi.202200709.
[66] S. Xu *et al.*, “A Neural Sensor with a Nanocomposite Interface for the Study of Spike Characteristics of Hippocampal Neurons under Learning Training,” *Biosensors*, vol. 12, no. 7, 2022, doi: 10.3390/bios12070546.
[67] V. S. Vajrala, K. Elkhoury, S. Pautot, C. Bergaud, and A. Maziz, “Hollow ring-like flexible electrode architecture enabling subcellular multi-directional neural interfacing,” *Biosens. Bioelectron.*, vol. 227, p. 115182, May 2023, doi: 10.1016/j.bios.2023.115182.
[68] Z. Lu *et al.*, “Microelectrode Arrays Measure Blocking of Voltage-Gated Calcium Ion Channels on Supported Lipid Bilayers Derived from Primary Neurons,” *Adv. Sci.*, vol. 11, no. 27, 2024, doi: 10.1002/advs.202304301.
[69] G. Dijk, J. Pas, K. Markovic, J. Scancar, and R. P. O’Connor, “PEDOT:PSS-coated platinum electrodes for neural stimulation,” *APL Bioeng.*, vol. 7, no. 4, 2023, doi: 10.1063/5.0153094.
[70] J. P. Thomas, L. Zhao, D. McGillivray, and K. T. Leung, “High-efficiency hybrid solar cells by nanostructural modification in PEDOT:PSS with co-solvent addition,” *J. Mater. Chem. A*, vol. 2, no. 7, pp. 2383–2389, Jan. 2014, doi: 10.1039/C3TA14590E.
[71] Y. H. Kim, C. Sachse, M. L. Machala, C. May, L. Müller-Meskamp, and K. Leo, “Highly Conductive PEDOT:PSS Electrode with Optimized Solvent and Thermal Post-Treatment for ITO-Free Organic Solar Cells,” *Adv. Funct. Mater.*, vol. 21, no. 6, pp. 1076–1081, 2011, doi: 10.1002/adfm.201002290.
[72] X. Liu and W. Wu, “Stripping Superficial polystyrene sulfonate on PEDOT:PSS via dodecyl benzenesulfonic acid for high-performance double-crosslinked hydrogel in flexible supercapacitor,” *Electrochimica Acta*, vol. 467, p. 143080, Nov. 2023, doi: 10.1016/j.electacta.2023.143080.
[73] A. Håkansson *et al.*, “Effect of (3-glycidyloxypropyl)trimethoxysilane (GOPS) on the electrical properties of PEDOT:PSS films,” *J. Polym. Sci. Part B Polym. Phys.*, vol. 55, no. 10, pp. 814–820, 2017, doi: 10.1002/polb.24331.
[74] H. Yu, S.-S. Fu, Y.-L. Jiang, G.-D. Zhu, B.-Z. Li, and D. W. Zhang, “An automatic recoverable organic fuse based on Au/PEDOT:PSS/Au structure,” in *2012 IEEE 11th International Conference on Solid-State and Integrated Circuit Technology*, Oct. 2012, pp. 1–3. doi: 10.1109/ICSICT.2012.6467742.

[75] S. Möller, C. Perlov, W. Jackson, C. Taussig, and S. R. Forrest, “A polymer/semiconductor write-once read-many-times memory,” *Nature*, vol. 426, no. 6963, pp. 166–169, Nov. 2003, doi: 10.1038/nature02070.
[76] S. Yin *et al.*, “A cell–electrode interface signal-to-noise ratio model for 3D micro-nano electrode,” *J. Neural Eng.*, vol. 20, no. 4, p. 046034, Aug. 2023, doi: 10.1088/1741-2552/ace933.
[77] Y.-J. (林祐仲) Lin, W.-S. (倪維仕) Ni, and J.-Y. (李哲佑) Lee, “Effect of incorporation of ethylene glycol into PEDOT:PSS on electron phonon coupling and conductivity,” *J. Appl. Phys.*, vol. 117, no. 21, p. 215501, June 2015, doi: 10.1063/1.4921930.
[78] G. R. P., S. R. V., A. Kanwat, and J. Jang, “Enhanced organic photovoltaic properties via structural modifications in PEDOT:PSS due to graphene oxide doping,” *Mater. Res. Bull.*, vol. 74, pp. 346–352, Feb. 2016, doi: 10.1016/j.materresbull.2015.10.044.
[79] J. Li, J.-C. Liu, and C.-J. Gao, “On the mechanism of conductivity enhancement in PEDOT/PSS film doped with multi-walled carbon nanotubes,” *J. Polym. Res.*, vol. 17, no. 5, pp. 713–718, Sept. 2010, doi: 10.1007/s10965-009-9360-1.
[80] H. Yousefian, S. A. Hashemi, A. Babaei-Ghazvini, B. Acharya, A. Ghaffarkhah, and M. Arjmand, “Beyond acid treatment of PEDOT:PSS: decoding mechanisms of electrical conductivity enhancement,” *Mater. Adv.*, vol. 5, no. 11, pp. 4699–4714, June 2024, doi: 10.1039/D4MA00078A.
[81] J. Ouyang, “Solution-Processed PEDOT:PSS Films with Conductivities as Indium Tin Oxide through a Treatment with Mild and Weak Organic Acids,” *ACS Appl. Mater. Interfaces*, vol. 5, no. 24, pp. 13082–13088, Dec. 2013, doi: 10.1021/am404113n.
[82] L. Bießmann, N. Saxena, N. Hohn, M. A. Hossain, J. G. C. Veinot, and P. Müller-Buschbaum, “Highly Conducting, Transparent PEDOT:PSS Polymer Electrodes from Post-Treatment with Weak and Strong Acids,” *Adv. Electron. Mater.*, vol. 5, no. 2, p. 1800654, 2019, doi: 10.1002/aelm.201800654.
[83] B. Adilbekova *et al.*, “Enhancing the Electrical Conductivity and Long-Term Stability of PEDOT:PSS Electrodes through Sequential Treatment with Nitric Acid and Cesium Chloride,” *Adv. Mater.*, vol. 36, no. 41, p. 2405094, Oct. 2024, doi: 10.1002/adma.202405094.
[84] A. Chakraborty, A. DiFilippo, S. Deivasigamani, C. Hong, A. Madwesh, and M. Orlowski, “Methods to Enhance Electrical Conductivity of PEDOT:PSS-based Electrodes,” Feb. 13, 2024, *In Review*. doi: 10.21203/rs.3.rs-3911736/v1.
[85] J. Kim, J. G. Jang, J.-I. Hong, S. H. Kim, and J. Kwak, “Sulfuric acid vapor treatment for enhancing the thermoelectric properties of PEDOT:PSS thin-films,” *J. Mater. Sci. Mater. Electron.*, vol. 27, no. 6, pp. 6122–6127, June 2016, doi: 10.1007/s10854-016-4538-x.
[86] J. H. Lee *et al.*, “Highly Conductive, Stretchable, and Transparent PEDOT:PSS Electrodes Fabricated with Triblock Copolymer Additives and Acid Treatment,” *ACS Appl. Mater. Interfaces*, July 2018, doi: 10.1021/acsami.8b07287.
[87] H. Shi, C. Liu, Q. Jiang, and J. Xu, “Effective Approaches to Improve the Electrical Conductivity of PEDOT:PSS: A Review,” *Adv. Electron. Mater.*, vol. 1, no. 4, p. 1500017, 2015, doi: 10.1002/aelm.201500017.
[88] “Significant Conductivity Enhancement of Conductive Poly(3,4-ethylenedioxythiophene): Poly(styrenesulfonate) Films through a Treatment with Organic Carboxylic Acids and Inorganic Acids | ACS Applied Materials & Interfaces.” Accessed: June 07, 2025. [Online]. Available: https://pubs.acs.org/doi/full/10.1021/am900708x?casa_token=CHo73tgaur8AAAAA%3AsWWoJDlVixKyWSBcxXKgTJR1qY55z7x1K68lebT8inxEVIY-BPZO7pVyQ6VWAmQFRgT_Ob1Qxl7t_eNQ
[89] “Single-step treatment to improve conductivity of PEDOT:PSS by hydrobromic acid solution for application of transparent electrode,” *Org. Electron.*, vol. 110, p. 106643, Nov. 2022, doi: 10.1016/j.orgel.2022.106643.
[90] “Conductivity Enhancement of PEDOT:PSS via Addition of Chloroplatinic Acid and Its Mechanism - Wu - 2017 - Advanced Electronic Materials - Wiley Online Library.” Accessed: June 07, 2025. [Online]. Available: https://advanced.onlinelibrary.wiley.com/doi/full/10.1002/aelm.201700047?casa_token=u6xbHuvxExYAAAAA%3AA_esxUM06rlENViFUBaujG8zS4VmizZ2HzoGS0sMB0U0Msvx7T6iK1iykfqztPJCaY4MzbR2A_QuSohG

[91] A. Pisciotta *et al.*, “PEDOT: PSS promotes neurogenic commitment of neural crest-derived stem cells,” *Front. Physiol.*, vol. 13, Aug. 2022, doi: 10.3389/fphys.2022.930804.
[92] G. Cellot *et al.*, “PEDOT:PSS Interfaces Support the Development of Neuronal Synaptic Networks with Reduced Neuroglia Response In vitro,” *Front. Neurosci.*, vol. 9, p. 521, Jan. 2016, doi: 10.3389/fnins.2015.00521.
[93] N. Hong, B. Kim, J. Lee, H. K. Choe, K. H. Jin, and H. Kang, “Machine learning-based high-frequency neuronal spike reconstruction from low-frequency and low-sampling-rate recordings,” *Nat. Commun.*, vol. 15, no. 1, p. 635, Jan. 2024, doi: 10.1038/s41467-024-44794-2.
[94] G. Ellis, “Chapter 9 - Filters in Control Systems,” in *Control System Design Guide (Fourth Edition)*, G. Ellis, Ed., Boston: Butterworth-Heinemann, 2012, pp. 165–183. doi: 10.1016/B978-0-12-385920-4.00009-6.
[95] “A novel algorithm for precise identification of spikes in extracellularly recorded neuronal signals,” *J. Neurosci. Methods*, vol. 177, no. 1, pp. 241–249, Feb. 2009, doi: 10.1016/j.jneumeth.2008.09.026.
[96] M. S. Fee, P. P. Mitra, and D. Kleinfeld, “Variability of extracellular spike waveforms of cortical neurons,” *J. Neurophysiol.*, vol. 76, no. 6, pp. 3823–3833, Dec. 1996, doi: 10.1152/jn.1996.76.6.3823.
[97] Y. Nam and B. C. Wheeler, “In Vitro Microelectrode Array Technology and Neural Recordings,” *Crit. Rev. Biomed. Eng.*, vol. 39, no. 1, 2011, doi: 10.1615/CritRevBiomedEng.v39.i1.40.
[98] K. J. Laboy-Juárez, S. Ahn, and D. E. Feldman, “A normalized template matching method for improving spike detection in extracellular voltage recordings,” *Sci. Rep.*, vol. 9, no. 1, p. 12087, Aug. 2019, doi: 10.1038/s41598-019-48456-y.
[99] S. Someck, A. Levi, H. E. Sloin, L. Spivak, R. Gattegno, and E. Stark, “Positive and biphasic extracellular waveforms correspond to return currents and axonal spikes,” *Commun. Biol.*, vol. 6, no. 1, p. 950, Sept. 2023, doi: 10.1038/s42003-023-05328-6.
[100] Y. J. Jung, S. H. Sun, A. Almasi, M. Yunzab, H. Meffin, and M. R. Ibbotson, “Characterization of extracellular spike waveforms recorded in wallaby primary visual cortex,” *Front. Neurosci.*, vol. 17, p. 1244952, Sept. 2023, doi: 10.3389/fnins.2023.1244952.
[101] G. Czanner *et al.*, “Measuring the signal-to-noise ratio of a neuron,” *Natl. Acad. Sci. US*, June 2015, Accessed: Aug. 06, 2025. [Online]. Available: https://dspace.mit.edu/handle/1721.1/100795
[102] V. Dimakopoulos, G. Selmin, L. Regli, and J. Sarnthein, “Optimization of signal-to-noise ratio in short-duration SEP recordings by variation of stimulation rate,” *Clin. Neurophysiol.*, vol. 150, pp. 89–97, June 2023, doi: 10.1016/j.clinph.2023.03.008.
[103] P. G. Musial, S. N. Baker, G. L. Gerstein, E. A. King, and J. G. Keating, “Signal-to-noise ratio improvement in multiple electrode recording,” *J. Neurosci. Methods*, vol. 115, no. 1, pp. 29–43, Mar. 2002, doi: 10.1016/S0165-0270(01)00516-7.
[104] T. Feng, Q. Chen, M. Yi, and Z. Xiao, “Improvement of signal-to-noise ratio in parallel neuron arrays with spatially nearest neighbor correlated noise,” *PLOS ONE*, vol. 13, no. 7, p. e0200890, July 2018, doi: 10.1371/journal.pone.0200890.
[105] A. Suarez-Perez *et al.*, “Quantification of Signal-to-Noise Ratio in Cerebral Cortex Recordings Using Flexible MEAs With Co-localized Platinum Black, Carbon Nanotubes, and Gold Electrodes,” *Front. Neurosci.*, vol. 12, p. 862, Nov. 2018, doi: 10.3389/fnins.2018.00862.
[106] D. Khodagholy *et al.*, “In vivo recordings of brain activity using organic transistors,” *Nat. Commun.*, vol. 4, no. 1, p. 1575, Mar. 2013, doi: 10.1038/ncomms2573.
[107] V. M. Eisenkolb *et al.*, “Human acute microelectrode array recordings with broad cortical access, single-unit resolution, and parallel behavioral monitoring,” *Cell Rep.*, vol. 42, no. 5, p. 112467, May 2023, doi: 10.1016/j.celrep.2023.112467.
[108] X. M. Spijkers, S. Pasteuning-Vuhman, J. C. Dorleijn, P. Vulto, N. R. Wevers, and R. J. Pasterkamp, “A directional 3D neurite outgrowth model for studying motor axon biology and disease,” *Sci. Rep.*, vol. 11, no. 1, p. 2080, Jan. 2021, doi: 10.1038/s41598-021-81335-z.
[109] M. H. Soltani *et al.*, “Microtubule-Associated Protein 2, a Marker of Neuronal Differentiation, Induces Mitotic Defects, Inhibits Growth of Melanoma Cells, and Predicts Metastatic Potential of Cutaneous Melanoma,” *Am. J. Pathol.*, vol. 166, no. 6, pp. 1841–1850, June 2005, doi: 10.1016/S0002-9440(10)62493-5.

[110] B. Milky *et al.*, “Long-term adherence of human brain cells *in vitro* is enhanced by charged amine-based plasma polymer coatings,” *Stem Cell Rep.*, vol. 17, no. 3, pp. 489–506, Mar. 2022, doi: 10.1016/j.stemcr.2022.01.013.
[111] S. Khan and G. Newaz, “A comprehensive review of surface modification for neural cell adhesion and patterning,” *J. Biomed. Mater. Res. A*, vol. 93A, no. 3, pp. 1209–1224, June 2010, doi: 10.1002/jbm.a.32698.
[112] P. Roach, T. Parker, N. Gadegaard, and M. R. Alexander, “Surface strategies for control of neuronal cell adhesion: A review,” *Surf. Sci. Rep.*, vol. 65, no. 6, pp. 145–173, June 2010, doi: 10.1016/j.surfrep.2010.07.001.
[113] T. Marques-Almeida *et al.*, “Electroactive Materials Surface Charge Impacts Neuron Viability and Maturation in 2D Cultures,” *ACS Appl. Mater. Interfaces*, vol. 15, no. 26, pp. 31206–31213, July 2023, doi: 10.1021/acsami.3c04055.
[114] Y. Furukawa, A. Shimada, K. Kato, H. Iwata, and K. Torimitsu, “Monitoring neural stem cell differentiation using PEDOT–PSS based MEA,” *Biochim. Biophys. Acta BBA - Gen. Subj.*, vol. 1830, no. 9, pp. 4329–4333, Sept. 2013, doi: 10.1016/j.bbagen.2013.01.022.
[115] S. Alasmar *et al.*, “Improved Cryopreservation of Human Induced Pluripotent Stem Cell (iPSC) and iPSC-derived Neurons Using Ice-Recrystallization Inhibitors,” *Stem Cells*, vol. 41, no. 11, pp. 1006–1021, Nov. 2023, doi: 10.1093/stmcls/sxad059.
[116] N. J. Drummond, K. Singh Dolt, M. A. Canham, P. Kilbride, G. J. Morris, and T. Kunath, “Cryopreservation of Human Midbrain Dopaminergic Neural Progenitor Cells Poised for Neuronal Differentiation,” *Front. Cell Dev. Biol.*, vol. 8, Nov. 2020, doi: 10.3389/fcell.2020.578907.
[117] J. Kaindl *et al.*, “Zooming in on Cryopreservation of hiPSCs and Neural Derivatives: A Dual-Center Study Using Adherent Vitrification,” *Stem Cells Transl. Med.*, vol. 8, no. 3, pp. 247–259, Mar. 2019, doi: 10.1002/sctm.18-0121.
[118] S. Alasmar *et al.*, “Improved Cryopreservation of Human Induced Pluripotent Stem Cell (iPSC) and iPSC-derived Neurons Using Ice-Recrystallization Inhibitors,” *Stem Cells*, vol. 41, no. 11, pp. 1006–1021, Nov. 2023, doi: 10.1093/stmcls/sxad059.
[119] T. Osaki, S. G. M. Uzel, and R. D. Kamm, “Microphysiological 3D model of amyotrophic lateral sclerosis (ALS) from human iPS-derived muscle cells and optogenetic motor neurons,” *Sci. Adv.*, vol. 4, no. 10, p. eaat5847, Oct. 2018, doi: 10.1126/sciadv.aat5847.
[120] K. D. A. Rienecker, R. G. Poston, and R. N. Saha, “Merits and Limitations of Studying Neuronal Depolarization-Dependent Processes Using Elevated External Potassium,” *ASN NEURO*, vol. 12, p. 1759091420974807, Nov. 2020, doi: 10.1177/1759091420974807.
[121] E. E. J. Kasteel and R. H. S. Westerink, “Comparison of the acute inhibitory effects of Tetrodotoxin (TTX) in rat and human neuronal networks for risk assessment purposes,” *Toxicol. Lett.*, vol. 270, pp. 12–16, Mar. 2017, doi: 10.1016/j.toxlet.2017.02.014.
[122] S. Aryal and PhD, “Polymerase Chain Reaction (PCR)- Principle, Steps, Applications.” Accessed: July 29, 2025. [Online]. Available: https://microbenotes.com/polymerase-chain-reaction-pcr-principle-steps-applications/

Supplementary information: MEA design

A design developed and produced by Mustafeez Shah was used for the MEA, as seen on the figure below. It is made of hybrid tracks that are made of gold and PEDOT:PSS deposited on top of a glass substrate. A glass well was bonded to the MEA using PDMS (SYLGARD™ 184) and biocompatible epoxy (EPO-TEK MED-301-2, Sigma Aldrich) was used to encapsulate outside the well.

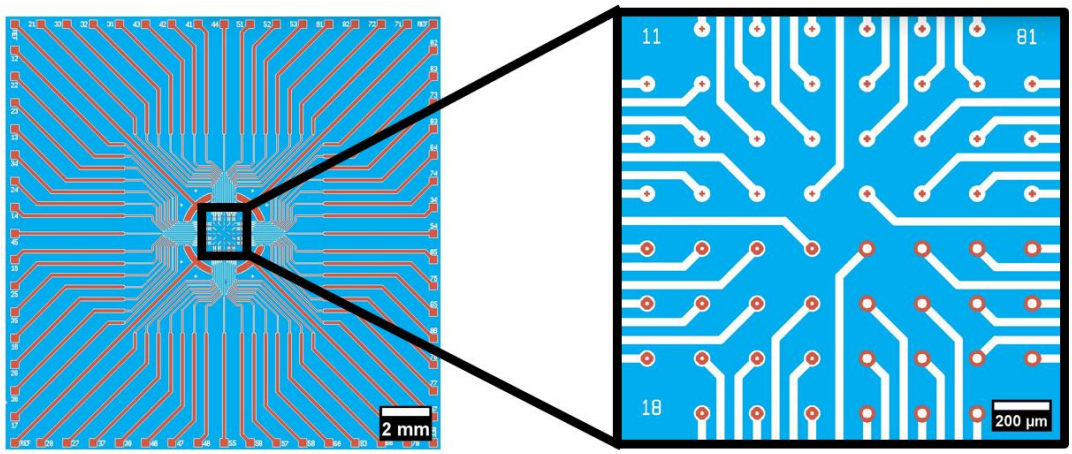

Figure. PEDOT:PSS MEA. On the close-up, four different electrode opening sizes from top left clockwise: 5 µm, 10 µm, 50 µm, and 30 µm.

Supplementary Information: MATLAB® code

Spike retrieval

Loading file

```
clear all
File_path = ""; %Path of the file containing the recording
load(File_path)
%Modified from open source code available at:
%http://www.mathworks.com/matlabcentral/fileexchange/54277-joint-analysis-of-extracellular-spike-waveforms-and-neuronal-network-bursts
%Spike waveforms are defined as the ones spanning 1 ms prior and 2.2 ms after the maximum of the spike
%according to https://www.sciencedirect.com/science/article/pii/S0165027015004240#fig0005

ms = round(fs.filtersettings.sampling_frequency/1000); %10x10^-4 s = 1 ms
Filtered_data_array = cell(1,length(M2));
for i=1:length(M2)
%     Filtered_data_array{i}=[filteredData1(i,302250:end)];

Filtered_data_array{i}=[filteredData1(i,1:1850000),filteredData1(i,1920001:end)];
end
%only negative spikes
M20 = {};
for i = 1:length(filteredData1(:,1))
   [~,temp_spike_index] =intersect(X2,M66{i,1},'stable'); % returns the values of index vectors in the same order that they appear in X2
   M20{i} = temp_spike_index;
end
M20 =M20';      %contains all the indices of the spike timings
M21 = {};
M22 = {};
for i =1:length(filteredData1(:,1))
   IDX80 = M20{i,1} - (ms);    %should be around 1 ms
   IDX90 = M20{i,1} + round(ms*2.2);  %should be around 2.2 ms (it used to be 2.2)
   valid_spike_index2 = [];
   for t = 1:length(IDX90)
      if IDX90(t) < 1850000
         valid_spike_index2 = [valid_spike_index2;IDX90(t)];
      elseif IDX90(t) > 1920023
         valid_spike_index2 = [valid_spike_index2;IDX90(t)];
      else
         continue
      end
   end
   valid_spike_index1 = [];
   for y = 1:length(IDX80)
      if IDX80(y) < 1849990
         valid_spike_index1 = [valid_spike_index1;IDX80(y)];
      elseif IDX80(y) > 1920001
         valid_spike_index1 = [valid_spike_index1;IDX80(y)];
      else
         continue
      end
   end
   IDX80 = valid_spike_index1;
   IDX90 = valid_spike_index2;
   M21{i} = IDX80;
   M22{i} = IDX90;
end
% check if indices are not lower than 1 and not higher than the
% max amount of samples
for i =1:length(M22)
   for j = 1:length(M22{i})
      if length(M22{i}) < 10
         continue
      else
         if M22{i}(j) < 1
            M22{i}(j) = 1;
         end
      end
   end
end
for i =1:length(M22)
   for j = 1:length(M22{i})
      if length(M22{i}) < 10
         continue
      else
         if M22{i}(j) > length(Filtered_data_array{1})
            M22{i}(j) = length(Filtered_data_array{1});
         end
      end
   end
end
for i =1:length(M21)
   for j = 1:length(M21{i})
      if length(M21{i}) < 10
         continue
      else
         if M21{i}(j) < 1
            M21{i}(j) = 1;
         end
      end
   end
end
for i =1:length(M21)
   for j = 1:length(M21{i})
      if length(M21{i}) < 10
         continue
      else
         if M21{i}(j) > length(Filtered_data_array{1})
            M21{i}(j) = length(Filtered_data_array{1});
         end
      end
   end
end
clear Data2 M19 M20 temp_spike_index IDX80 IDX90 valid_spike_index2 valid_spike_index1
%Analysis starts later and ends earlier to prevent indices going out of reach
% idx5869 = cellfun(@isempty, M21);
% idx5869 = (idx5869 < 10); % channels with less than 10 spikes are also removed
% M21(idx5869) = {1}; %to fill the empty spaces with 1
% idx5869 = cellfun(@isempty, M22); %remove the empty arrays (Lose channel information)
% idx5869 = (idx5869 < 10); % channels with less than 10 spikes are also removed
% M22(idx5869) = {1};
% clear idx5869
Spikeform3={};
for j =1:length(M22)
   Spikeform2={};
   for i =1:length(M22{j})
      Spikeform = Filtered_data_array{j}(M21{j}(i):M22{j}(i));
      if length(Spikeform) < (ms*2.2+ms+1)
         Spikeform((ms*2.2+ms+1)) = 0;
      end
      Spikeform2{i} = Spikeform;
   end
   Spikeform2 = vertcat(Spikeform2{:});
   Spikeform3{j}=Spikeform2;
end
Spikeform3 =Spikeform3'; %contains all the unit waveforms of all the channels that had activity
```

```
for i=1:length(Spikeform3)
    Spikeform3{i,1}=Spikeform3{i}';
end
clear i j k
clear M21 M22 Spikeform2 Spikeform
%only positive spikes
M20 = {};
for i = 1:length(filteredData1(:,1))
    [~,temp_spike_index] =intersect(X2,M111{i,1},'stable');
    M20{i} = temp_spike_index;
end
M20 =M20';        %contains all the indices of the spike timings
M21 = {};
M22 = {};
for i =1:length(filteredData1(:,1))
    IDX80 = M20{i,1} - ms;      %should be around 1 ms
    IDX90 = M20{i,1} + round(ms*2.2);   %should be around 2.2
ms
    valid_spike_index2 = [];
    for t = 1:length(IDX90)
        if IDX90(t) < 1850000
            valid_spike_index2 = [valid_spike_index2;IDX90(t)];
        elseif IDX90(t) > 1920023
            valid_spike_index2 = [valid_spike_index2;IDX90(t)];
        else
            continue
        end
    end
    valid_spike_index1 = [];
    for y = 1:length(IDX80)
        if IDX80(y) < 1849990
            valid_spike_index1 = [valid_spike_index1;IDX80(y)];
        elseif IDX80(y) > 1920001
            valid_spike_index1 = [valid_spike_index1;IDX80(y)];
        else
            continue
        end
    end
    IDX80 = valid_spike_index1;
    IDX90 = valid_spike_index2;
    M21{i} = IDX80;
    M22{i} = IDX90;
end
% check if indices are not lower than 1 and not higher than the
% max amount of samples
for i =1:length(M22)
    for j = 1:length(M22{i})
        if length(M22{i}) < 10
            continue
        else
            if M22{i}(j) < 1
                M22{i}(j) = 1;
            end
        end
    end
end

for i =1:length(M22)
    for j = 1:length(M22{i})
        if length(M22{i}) < 10
            continue
        else
            if M22{i}(j) > length(Filtered_data_array{1})
                M22{i}(j) = length(Filtered_data_array{1});
            end
        end
    end
end

for i =1:length(M21)
    for j = 1:length(M21{i})
        if length(M21{i}) < 10
            continue
        else
            if M21{i}(j) < 1
                M21{i}(j) = 1;
            end
        end
    end
end

for i =1:length(M21)
    for j = 1:length(M21{i})
        if length(M21{i}) < 10
            continue
        else
            if M21{i}(j) > length(Filtered_data_array{1})
                M21{i}(j) = length(Filtered_data_array{1});
            end
        end
    end
end

clear Data2 M19 M20 temp_spike_index IDX80 IDX90
valid_spike_index2 valid_spike_index1

idx5869 = cellfun(@length, M21);
idx5869 = (idx5869 < 1); % channels without spikes are also
removed
M21(idx5869) = {1}; %to fill the empty spaces with 1
idx5869 = cellfun(@length, M22); %remove the empty arrays
(Lose channel information)
idx5869 = (idx5869 < 1); % channels without spikes are also
removed
M22(idx5869) = {1};
clear idx5869
Spikeform4={};
for j =1:length(M22)
    Spikeform2=[];
    for i =1:length(M22{j})
        Spikeform = Filtered_data_array{j}(M21{j}(i):M22{j}(i));
        if length(Spikeform) < (ms*2.2+ms+1)
            Spikeform((ms*2.2+ms+1)) = 0;
        end
        %              Spikeform2 =[Spikeform2;Spikeform];
        Spikeform2{i} = Spikeform;
    end
    Spikeform2 = vertcat(Spikeform2{:});
    Spikeform4{j}=Spikeform2;
end
Spikeform4 =Spikeform4'; %contains all the unit waveforms of
all the channels that had activity
for i=1:length(Spikeform4)
    Spikeform4{i,1}=Spikeform4{i}';
end
clear i j k t y
clear M21 M22 Spikeform2 Filtered_data_array Spikeform ms
Truly obtaining the data
%run spikeform extraction above
close all
x_axis = 0:0.1:3.2;
[~, counter_1] = size(Spikeform3{34});
for loop_count_1 = 1:counter_1
    vec = isnan(Spikeform3{34}(:,loop_count_1));
    if sum(vec) > 0
        Spikeform3{34}(:,loop_count_1)                    =
zeros(size(Spikeform3{34}(:,loop_count_1)));
    end
end
[~,counter_2] = size(Spikeform3{42});
spike_form_holder_1 = [];
for loop_count_2 = 1:counter_2
    if    -3    >    min(Spikeform3{42}(11,loop_count_2))    &&
min(Spikeform3{42}(11,loop_count_2)) > -150
        continue
    else
        spike_form_holder_1                                 =
[spike_form_holder_1,Spikeform3{42}(:,loop_count_2)];
    end
end
Spikeform3{42} = spike_form_holder_1;
[~, counter_3] = size(Spikeform4{34});
for loop_count_3 = 1:counter_3
    if min(Spikeform4{34}(:,loop_count_3)) < -1000
        Spikeform4{34}(:,loop_count_3)                    =
zeros(size(Spikeform4{34}(:,loop_count_3)));
    end
end
[~,counter_4] = size(Spikeform4{42});
spike_form_holder_2 = [];
for loop_count_4 = 1:counter_4
    if    100    >    min(Spikeform4{42}(11,loop_count_4))    &&
min(Spikeform4{42}(11,loop_count_4)) > 0
        continue
```

```
    else
        spike_form_holder_2                                    =
[spike_form_holder_2,Spikeform4{42}(:,loop_count_4)];
    end
end
Spikeform4{42} = spike_form_holder_2;
% Unfiltered 5 um
% figure
%                                                       plot(x_axis,
Spikeform3{1},x_axis,Spikeform3{2},x_axis,Spikeform3{3},x_ax
is,Spikeform3{4},x_axis,Spikeform3{5})
% hold on
%                                                       plot(x_axis,
Spikeform3{6},x_axis,Spikeform3{7},x_axis,Spikeform3{8},x_ax
is,Spikeform3{9},x_axis,Spikeform3{10})
% hold on
%                                                       plot(x_axis,
Spikeform3{11},x_axis,Spikeform3{12},x_axis,Spikeform3{13},
x_axis,Spikeform3{14},x_axis,Spikeform3{15})
% hold on
%                                                       plot(x_axis,
Spikeform3{16},x_axis,Spikeform3{17},x_axis,Spikeform3{18},
x_axis,Spikeform3{19},x_axis,Spikeform3{20})
% hold on
%                                                       plot(x_axis,
Spikeform3{21},x_axis,Spikeform3{22},x_axis,Spikeform3{23},
x_axis,Spikeform3{24},x_axis,Spikeform3{25})
% hold on
%                                                       plot(x_axis,
Spikeform3{26},x_axis,Spikeform3{27},x_axis,Spikeform3{28},
x_axis,Spikeform3{29},x_axis,Spikeform3{30})
% hold on
%                                                       plot(x_axis,
Spikeform3{31},x_axis,Spikeform3{32},x_axis,Spikeform3{33},
x_axis,Spikeform3{34},x_axis,Spikeform3{35})
% hold on
%                                                       plot(x_axis,
Spikeform3{36},x_axis,Spikeform3{37},x_axis,Spikeform3{38},
x_axis,Spikeform3{39},x_axis,Spikeform3{40})
% hold on
%                                                       plot(x_axis,
Spikeform3{41},x_axis,Spikeform3{42},x_axis,Spikeform3{43},
x_axis,Spikeform3{44},x_axis,Spikeform3{45})
% hold on
%                                                       plot(x_axis,
Spikeform3{46},x_axis,Spikeform3{47},x_axis,Spikeform3{48},
x_axis,Spikeform3{49},x_axis,Spikeform3{50})
% hold on
%                                                       plot(x_axis,
Spikeform3{51},x_axis,Spikeform3{52},x_axis,Spikeform3{53},
x_axis,Spikeform3{54},x_axis,Spikeform3{55})
% hold on
%                                                       plot(x_axis,
Spikeform3{56},x_axis,Spikeform3{57},x_axis,Spikeform3{58},
x_axis,Spikeform3{59},x_axis,Spikeform3{60})

negmono = []; %waveforms that have a negative monophasic
shape
posmono = []; %waveforms that have a positive monophasic
shape
negbi = [];   %waveforms that have a large negative peak then a
small positive peak
posbi = [];   %waveforms that have a large positive peak then a
small negative peak
negtri = [];  %waveforms that have a small positive peak then a
large negative peak then a small positive peak
postri = [];  %waveforms that have a small negative peak then a
large positive peak then a small negative peak
Potential_noiseneg = [];
Potential_noisepos = [];

for i = 1:60
    [~, cellsz1] = size(Spikeform3{i,1});
    [~, cellsz2] = size(Spikeform4{i,1});
    for j = 1:cellsz1
        if                max(abs(Spikeform3{i,1}(:,j)))                ~=
abs(Spikeform3{i,1}(11,j))
            Potential_noiseneg                                         =
[Potential_noiseneg,Spikeform3{i,1}(:,j)];
            continue
        elseif Spikeform3{i,1}(11,j) < -RMS7(i)
            if max(Spikeform3{i,1}(1:10,j)) > RMS7(i) &&
max(Spikeform3{i,1}(12:32,j)) > RMS7(i)
                negtri = [negtri,Spikeform3{i,1}(:,j)];
                continue
%                 elseif max(Spikeform3{i,1}(1:10,j)) > RMS7(i) ||
max(Spikeform3{i,1}(12:32,j)) > RMS7(i)
            elseif max(Spikeform3{i,1}(12:32,j)) > RMS7(i)
                negbi = [negbi,Spikeform3{i,1}(:,j)];
                continue
            elseif mean(Spikeform3{i,1}(1:10,j)) < -RMS7(i) ||
mean(Spikeform3{i,1}(12:32,j)) < -RMS7(i)
                Potential_noiseneg                                     =
[Potential_noiseneg,Spikeform3{i,1}(:,j)];
                continue
            else
                negmono = [negmono, Spikeform3{i,1}(:,j)];
                continue
            end
        end
    end
    for j = 1:cellsz2
%             if not(isempty(find(floor(min(Spikeform4{i,1}(:,j))) <
min(Spikeform3{i,1}) < ceil(min(Spikeform4{i,1}(:,j)))))
        if                max(abs(Spikeform4{i,1}(:,j)))                ~=
abs(Spikeform4{i,1}(11,j))
            Potential_noisepos                                         =
[Potential_noisepos,Spikeform4{i,1}(:,j)];
            continue
        elseif Spikeform4{i,1}(11,j) > RMS7(i)
            if max(Spikeform4{i,1}(1:10,j)) > RMS7(i) &&
max(Spikeform4{i,1}(12:32,j)) < -RMS7(i)
                postri = [postri,Spikeform4{i,1}(:,j)];
                continue
            elseif max(Spikeform4{i,1}(1:10,j)) > RMS7(i) ||
max(Spikeform4{i,1}(12:32,j)) < -RMS7(i)
                posbi = [posbi,Spikeform4{i,1}(:,j)];
                continue
            elseif mean(Spikeform4{i,1}(1:10,j)) > RMS7(i) &&
mean(Spikeform4{i,1}(12:32,j)) > RMS7(i)
                Potential_noisepos                                     =
[Potential_noisepos,Spikeform4{i,1}(:,j)];
                continue
            else
                posmono = [posmono, Spikeform4{i,1}(:,j)];
                continue
            end
        end
    end
end
figure
subplot(2,2,1)
plot(x_axis,posmono)
subplot(2,2,2)
plot(x_axis,posbi)
subplot(2,2,3)
plot(x_axis,Potential_noiseneg)
subplot(2,2,4)
plot(x_axis,Potential_noisepos)

avg_negmono = mean(negmono,2);
std_negmono = std(negmono,0,2);
avg_posmono = mean(posmono,2);
std_posmono = std(posmono,0,2);
avg_negbi = mean(negbi,2);
std_negbi = std(negbi,0,2);
avg_posbi = mean(posbi,2);
std_posbi = std(posbi,0,2);
avg_negtri = mean(negtri,2);
std_negtri = std(negtri,0,2);
avg_postri = mean(postri,2);
std_postri = std(postri,0,2);
avg_noise_neg = mean(Potential_noiseneg,2);
std_noise_neg = std(Potential_noiseneg,0,2);
avg_noise_pos = mean(Potential_noisepos,2);
std_noise_pos = std(Potential_noisepos,0,2);

figure
subplot(1,3,1)
fill([x_axis,      flip(x_axis)],      [avg_negmono+std_negmono;
flip(avg_negmono-std_negmono)],              [0.8              0.8
0.8],'LineStyle',"none")
hold on
```

```
plot(x_axis, avg_negmono, 'k')
ax = gca;
% ax.XColor = [1,1,1];
% ax.YColor = [1,1,1];
subplot(1,3,2)
fill([x_axis, flip(x_axis)], [avg_negbi+std_negbi; flip(avg_negbi-
std_negbi)], [0.5 0.8 0.8],'LineStyle',"none")
hold on
plot(x_axis, avg_negbi, 'k')
ax = gca;
% ax.XColor = [1,1,1];
% ax.YColor = [1,1,1];
ylim([-500 300])
if not(isempty(avg_negtri))
subplot(1,3,3)
fill([x_axis, flip(x_axis)], [avg_negtri+std_negtri; flip(avg_negtri-
std_negtri)], [0.8 0.5 0.8],'LineStyle',"none")
hold on
plot(x_axis, avg_negtri, 'k')
ax = gca;
ax.XColor = [1,1,1];
ax.YColor = [1,1,1];
end
if not(isempty(avg_posmono)) || not(isempty(avg_posbi)) ||
not(isempty(avg_postri))
figure
subplot(1,3,1)
fill([x_axis, flip(x_axis)], [avg_posmono+std_posmono;
flip(avg_posmono-std_posmono)], [0.8 0.8
0.8],'LineStyle',"none")
hold on
plot(x_axis, avg_posmono, 'k')
ax = gca;
% ax.XColor = [1,1,1];
% ax.YColor = [1,1,1];
subplot(1,3,2)
fill([x_axis, flip(x_axis)], [avg_posbi+std_posbi; flip(avg_posbi-
std_posbi)], [0.5 0.8 0.8],'LineStyle',"none")
hold on
plot(x_axis, avg_posbi, 'k')
ax = gca;
% ax.XColor = [1,1,1];
% ax.YColor = [1,1,1];
ylim([-500 300])
if not(isempty(postri))
subplot(1,3,3)
fill([x_axis, flip(x_axis)], [avg_postri+std_postri; flip(avg_postri-
std_postri)], [0.8 0.5 0.8],'LineStyle',"none")
hold on
plot(x_axis, avg_postri, 'k')
ax = gca;
ax.XColor = [1,1,1];
ax.YColor = [1,1,1];
end
end

if not(isempty(Potential_noiseneg)) &&
not(isempty(Potential_noisepos))
figure
subplot(1,3,1)
fill([x_axis, flip(x_axis)], [avg_noise_neg+std_noise_neg;
flip(avg_noise_neg-std_noise_neg)], [0.8 0.5
0.8],'LineStyle',"none")
hold on
plot(x_axis, avg_noise_neg, 'k')
ax = gca;
ylim([-500 300])
% ax.XColor = [1,1,1];
% ax.YColor = [1,1,1];
subplot(1,3,2)
fill([x_axis, flip(x_axis)], [avg_noise_pos+std_noise_pos;
flip(avg_noise_pos-std_noise_pos)], [0.8 0.5
0.8],'LineStyle',"none")
hold on
plot(x_axis, avg_noise_pos, 'k')
ax = gca;
ylim([-500 300])
% ax.XColor = [1,1,1];
% ax.YColor = [1,1,1];
end
```

Detailed waveform analysis

```
negmono1 = [];
negmono2 = [];
negmono3 = [];
negmono4 = [];
negbi1 = [];
negbi2 = [];
negbi3 = [];
negbi4 = [];
negtri1 = [];
negtri2 = [];
negtri3 = [];
negtri4 = [];

posmono1 = [];
posmono2 = [];
posmono3 = [];
posmono4 = [];
posbi1 = [];
posbi2 = [];
posbi3 = [];
posbi4 = [];
postri1 = [];
postri2 = [];
postri3 = [];
postri4 = [];

[~,cols] = size(negmono);
for i = 1:cols
   if negmono(11,i) < avg_negmono-std_negmono
      negmono1 = [negmono1,negmono(:,i)];
      continue
   elseif negmono(11,i) < avg_negmono
      negmono2 = [negmono2,negmono(:,i)];
      continue
   elseif negmono(11,i) < avg_negmono+std_negmono
      negmono3 = [negmono3,negmono(:,i)];
      continue
   else
      negmono4 = [negmono4,negmono(:,i)];
   end
end
[~,cols] = size(negbi);
for i = 1:cols
   if negbi(11,i) < avg_negbi-std_negbi
      negbi1 = [negbi1,negbi(:,i)];
      continue
   elseif negbi(11,i) < avg_negbi
      negbi2 = [negbi2,negbi(:,i)];
      continue
   elseif negbi(11,i) < avg_negbi+std_negbi
      negbi3 = [negbi3,negbi(:,i)];
      continue
   else
      negbi4 = [negbi4,negbi(:,i)];
   end
end
[~,cols] = size(negtri);
for i = 1:cols
   if negtri(11,i) < avg_negtri-std_negtri
      negtri1 = [negtri1,negtri(:,i)];
      continue
   elseif negtri(11,i) < avg_negtri
      negtri2 = [negtri2,negtri(:,i)];
      continue
   elseif negtri(11,i) < avg_negtri+std_negtri
      negtri3 = [negtri3,negtri(:,i)];
      continue
   else
      negtri4 = [negtri4,negtri(:,i)];
   end
end

[~,cols] = size(posmono);
for i = 1:cols
   if posmono(11,i) > avg_posmono+std_posmono
      posmono1 = [posmono1,posmono(:,i)];
      continue
   elseif posmono(11,i) > avg_posmono
      posmono2 = [posmono2,posmono(:,i)];
      continue
   elseif posmono(11,i) > avg_posmono-std_posmono
      posmono3 = [posmono3,posmono(:,i)];
```

```
        continue
    else
        posmono4 = [posmono4,posmono(:,i)];
    end
end
[~,cols] = size(posbi);
for i = 1:cols
    if posbi(11,i) > avg_posbi+std_posbi
        posbi1 = [posbi1,posbi(:,i)];
        continue
    elseif posbi(11,i) > avg_posbi
        posbi2 = [posbi2,posbi(:,i)];
        continue
    elseif posbi(11,i) > avg_posbi-std_posbi
        posbi3 = [posbi3,posbi(:,i)];
        continue
    else
        posbi4 = [posbi4,posbi(:,i)];
    end
end
[~,cols] = size(postri);
for i = 1:cols
    if postri(11,i) > avg_postri+std_postri
        postri1 = [postri1,postri(:,i)];
        continue
    elseif postri(11,i) > avg_postri
        postri2 = [postri2,postri(:,i)];
        continue
    elseif postri(11,i) > avg_postri-std_postri
        postri3 = [postri3,postri(:,i)];
        continue
    else
        postri4 = [postri4,postri(:,i)];
    end
end



avg_nm = [];
std_nm = [];
if any(negmono1)
avg_nm1 = mean(negmono1,2);
std_nm1 = std(negmono1,0,2);
avg_nm(:,1) = avg_nm1;
std_nm(:,1) = std_nm1;
else
avg_nm(:,1) = zeros([33,1]);
std_nm(:,1) = zeros([33,1]);
end
if any(negmono2)
avg_nm2 = mean(negmono2,2);
std_nm2 = std(negmono2,0,2);
avg_nm(:,2) = avg_nm2;
std_nm(:,2) = std_nm2;
else
avg_nm(:,2) = zeros([33,1]);
std_nm(:,2) = zeros([33,1]);
end
if any(negmono3)
avg_nm3 = mean(negmono3,2);
std_nm3 = std(negmono3,0,2);
avg_nm(:,3) = avg_nm3;
std_nm(:,3) = std_nm3;
else
avg_nm(:,3) = zeros([33,1]);
std_nm(:,3) = zeros([33,1]);
end
if any(negmono4)
avg_nm4 = mean(negmono4,2);
std_nm4 = mean(negmono4,2);
avg_nm(:,4) = avg_nm4;
std_nm(:,4) = std_nm4;
else
avg_nm(:,4) = zeros([33,1]);
std_nm(:,4) = zeros([33,1]);
end

avg_nb = [];
std_nb = [];
if any(negbi1)
avg_nb1 = mean(negbi1,2);
std_nb1 = std(negbi1,0,2);
avg_nb(:,1) = avg_nb1;
std_nb(:,1) = std_nb1;
else
    avg_nb(:,1) = zeros([33,1]);
std_nb(:,1) = zeros([33,1]);
end
if any(negbi2)
avg_nb2 = mean(negbi2,2);
std_nb2 = std(negbi2,0,2);
avg_nb(:,2) = avg_nb2;
std_nb(:,2) = std_nb2;
else
    avg_nb(:,2) = zeros([33,1]);
std_nb(:,2) = zeros([33,1]);
end
if any(negbi3)
avg_nb3 = mean(negbi3,2);
std_nb3 = std(negbi3,0,2);
avg_nb(:,3) = avg_nb3;
std_nb(:,3) = std_nb3;
else
    avg_nb(:,3) = zeros([33,1]);
std_nb(:,3) = zeros([33,1]);
end
if any(negbi4)
avg_nb4 = mean(negbi4,2);
std_nb4 = mean(negbi4,2);
avg_nb(:,4) = avg_nb4;
std_nb(:,4) = std_nb4;
else
    avg_nb(:,4) = zeros([33,1]);
std_nb(:,4) = zeros([33,1]);
end

avg_nt = [];
std_nt = [];
if any(negtri1)
avg_nt1 = mean(negtri1,2);
std_nt1 = std(negtri1,0,2);
avg_nt(:,1) = avg_nt1;
std_nt(:,1) = std_nt1;
else
    avg_nt(:,3) = zeros([33,1]);
std_nt(:,3) = zeros([33,1]);
end
if any(negtri2)
avg_nt2 = mean(negtri2,2);
std_nt2 = std(negtri2,0,2);
avg_nt(:,2) = avg_nt2;
std_nt(:,2) = std_nt2;
else
    avg_nt(:,3) = zeros([33,1]);
std_nt(:,3) = zeros([33,1]);
end
if any(negtri3)
avg_nt3 = mean(negtri3,2);
std_nt3 = std(negtri3,0,2);
avg_nt(:,3) = avg_nt3;
std_nt(:,3) = std_nt3;
else
    avg_nt(:,3) = zeros([33,1]);
std_nt(:,3) = zeros([33,1]);
end
if any(negtri4)
avg_nt4 = mean(negtri4,2);
std_nt4 = mean(negtri4,2);
avg_nt(:,4) = avg_nt4;
std_nt(:,4) = std_nt4;
else
    avg_nt(:,4) = zeros([33,1]);
std_nt(:,4) = zeros([33,1]);
end


avg_pm = [];
std_pm = [];
if any(posmono1)
avg_pm1 = mean(posmono1,2);
std_pm1 = std(posmono1,0,2);
avg_pm(:,1) = avg_pm1;
std_pm(:,1) = std_pm1;
else
```

```
avg_pm(:,1) = zeros([33,1]);
std_pm(:,1) = zeros([33,1]);
end
if any(posmono2)
avg_pm2 = mean(posmono2,2);
std_pm2 = std(posmono2,0,2);
avg_pm(:,2) = avg_pm2;
std_pm(:,2) = std_pm2;
else
avg_pm(:,2) = zeros([33,1]);
std_pm(:,2) = zeros([33,1]);
end
if any(posmono3)
avg_pm3 = mean(posmono3,2);
std_pm3 = std(posmono3,0,2);
avg_pm(:,3) = avg_pm3;
std_pm(:,3) = std_pm3;
else
avg_pm(:,3) = zeros([33,1]);
std_pm(:,3) = zeros([33,1]);
end
if any(posmono4)
avg_pm4 = mean(posmono4,2);
std_pm4 = mean(posmono4,2);
avg_pm(:,4) = avg_pm4;
std_pm(:,4) = std_pm4;
else
avg_pm(:,4) = zeros([33,1]);
std_pm(:,4) = zeros([33,1]);
end

avg_pb = [];
std_pb = [];
if any(posbi1)
avg_pb1 = mean(posbi1,2);
std_pb1 = std(posbi1,0,2);
avg_pb(:,1) = avg_pb1;
std_pb(:,1) = std_pb1;
else
   avg_pb(:,3) = zeros([33,1]);
std_pb(:,3) = zeros([33,1]);
end
if any(posbi2)
avg_pb2 = mean(posbi2,2);
std_pb2 = std(posbi2,0,2);
avg_pb(:,2) = avg_pb2;
std_pb(:,2) = std_pb2;
else
   avg_pb(:,3) = zeros([33,1]);
std_pb(:,3) = zeros([33,1]);
end
if any(posbi3)
avg_pb3 = mean(posbi3,2);
std_pb3 = std(posbi3,0,2);
avg_pb(:,3) = avg_pb3;
std_pb(:,3) = std_pb3;
else
   avg_pb(:,3) = zeros([33,1]);
std_pb(:,3) = zeros([33,1]);
end
if any(posbi4)
avg_pb4 = mean(posbi4,2);
std_pb4 = mean(posbi4,2);
avg_pb(:,4) = avg_pb4;
std_pb(:,4) = std_pb4;
else
   avg_pb(:,4) = zeros([33,1]);
std_pb(:,4) = zeros([33,1]);
end

avg_pt = [];
std_pt = [];
if any(postri1)
avg_pt1 = mean(postri1,2);
std_pt1 = std(postri1,0,2);
avg_pt(:,1) = avg_pt1;
std_pt(:,1) = std_pt1;
else
   avg_pt(:,1) = zeros([33,1]);
std_pt(:,1) = zeros([33,1]);
end
if any(postri2)
avg_pt2 = mean(postri2,2);
std_pt2 = std(postri2,0,2);
avg_pt(:,2) = avg_pt2;
std_pt(:,2) = std_pt2;
else
   avg_pt(:,3) = zeros([33,1]);
std_pt(:,3) = zeros([33,1]);
end
if any(postri3)
avg_pt3 = mean(postri3,2);
std_pt3 = std(postri3,0,2);
avg_pt(:,3) = avg_pt3;
std_pt(:,3) = std_pt3;
else
   avg_pt(:,3) = zeros([33,1]);
std_pt(:,3) = zeros([33,1]);
end
if any(postri4)
avg_pt4 = mean(postri4,2);
std_pt4 = mean(postri4,2);
avg_pt(:,4) = avg_pt4;
std_pt(:,4) = std_pt4;
else
   avg_pt(:,4) = zeros([33,1]);
std_pt(:,4) = zeros([33,1]);
end

Obtaining spikes
truespikes = [];
negspikes = [];
% M2 is a variable that contains information about
% the number of detected spikes on each channel
% and when they occurred. The rows represent the channels.
for i = 1:60
   spikecounter = 0;
   negspikecounter = -1;
   for k = 1:length(M2{i})
      if M2{i}(k) < 185 %time when the noise event happened
         spikecounter = spikecounter + 1;
      elseif M2{i}(k) > 192 %time when the noise event ended
         negspikecounter = negspikecounter + 1;
      else
         continue
      end
   end
   truespikes(i) = spikecounter;
   if negspikecounter ~= -1
      negspikes(i) = negspikecounter;
   else
      negspikes(i) = nan;
   end
end
neg_signal = [];
M88{34}(356) = 0; %removing outlier
M88{34}(357) = 0; %removing outlier
M88{34}(358) = 0; %removing outlier
for m = 1:60
   if truespikes(m) == 0 && isnan(negspikes(m))
      continue
   end
   negsignals = [min(M88{m}(1:truespikes(m)))];
   possignals = [max(M88{m}(1:truespikes(m)))];
   if not(isnan(negspikes))
      negsignals = [min(M88{m}(end:end-
negspikes(m))),min(M88{m}(1:truespikes(m)))];
      possignals = [max(M88{m}(end:end-
negspikes(m))),max(M88{m}(1:truespikes(m)))];
%       negmaxis = abs(max(M88{m}(end:end-negspikes(m)))) +
abs(min(M88{m}(end:end-negspikes(m))))
   end

%       maxis = abs(max(M88{m}(1:truespikes(m)))) +
abs(min(M88{m}(1:truespikes(m))));
   meannegsignals = mean(negsignals);
   meanpossignals = mean(possignals);
   neg_signal(m) =
sqrt(sum(abs(negsignals).^2)/abs(meannegsignals));
%max([maxis,negmaxis]);
   pos_signal(m) =
sqrt(sum(abs(negsignals).^2)/abs(meanpossignals));
end
% signales(120) = 0;
```

```
%Final snr
show_neg_signal = 20*log10(transpose(neg_signal)./(RMS7/7));
show_pos_signal = 20*log10(transpose(pos_signal)./(RMS7/7));
show_final = max(show_neg_signal,show_pos_signal,"omitnan")
```

Supplementary Information: Protocol

Differentiation protocol

6.2.1 005 – First Motor Neuron Progenitors run.

The following experiments are derived from the same cell vial from Axol, with 005 being the passage directly from the vial.

005-01 – Axol's differentiation protocol of MNPs

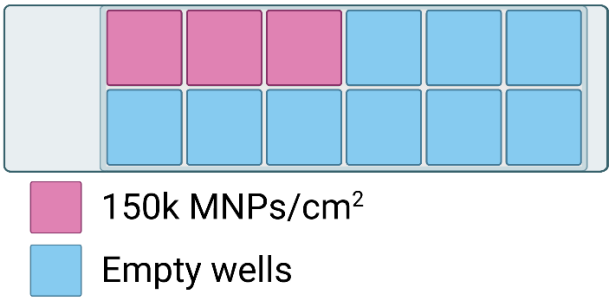

Figure 1. BioRender illustration of the seeding of MNPs in a 12-chamber Ibidi glass slide (81201).

Figure 1 shows a 12-well slide coated with PDL-VTN per the specifications of the Axol protocol, see **here**. This experimental run had two identical 12-well Ibidi slides. Most of the times a differentiation protocol was performed, this experimental set-up served as the reference group to compare to, unless otherwise noted. The meaning of the experimental run nomenclature is as follows: **0##**-## the first part refers to a particular cell passage and the second part, 00#-**##** refers to the parallel experiments for that particular passage.

Objective: Differentiate successfully the MNPs to MNs for 15 days. The success is determined by morphological changes using the single reference image Axol has and positive staining for MNs, e.g. TUJ1 or MAP2.

005-02 – Expansion of MNPs with MNMM4P on D0

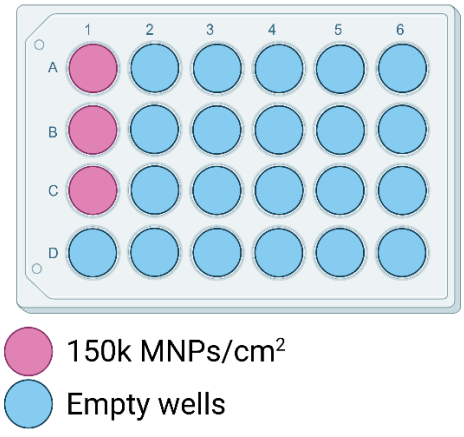

Figure 2. BioRender illustration of the seeding of MNPs in a 24-well plate.

Figure 2 shows a 24-well plate coated with Geltrex. This group was seeded with Motor Neuron Maintenance Medium for Plating that is used by the Axol differentiation protocol to plate the cells. On the day 1 media change, MNEMi was added and continued for the rest of the experiment. Only C1 was

passaged on day 7, as A1 underwent another experiment and B1 continued the expansion to see how it develops with time.

Objective: Increase the number of MNPs and maintain their differentiation potential, which can be seen with a differentiation run after passaging.

005-03 – Differentiation induction of the 005-02's A1

Using the A1 well of **figure 2**, a little experiment was done by changing the MNEMi to CMNMM to assess if the MNPs can be differentiated without the need of passaging.

Objective: Through morphological changes, assess if the MNPs change into MNs.

005-04 – Expansion of MNPs with MNEMi

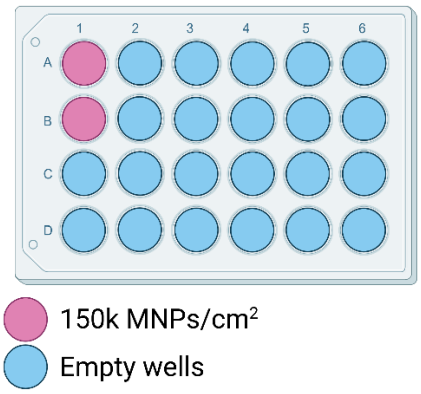

Figure 3. BioRender illustration of the seeding of MNPs in a 24-well plate.

Figure 3 shows a 24-well plate coated with Geltrex. This group was seeded with MNEMi from day 0 and follows the same Expansion Protocol stated before. All the wells for this condition were passaged after seven days of expansion.

Objective: Assess whether MNEMi is a viable plating medium compared to MNMM4P in increasing the number of MNPs and maintaining their differentiation potential.

6.2.2 006 – First Passaging

In this first passaging of the MNPs to the culture passage the experiments of the XXX and the experimental set-up 005-01 of Axol's differentiation protocol was repeated for this passage as well.

006-01 - Passaging protocol validation

From the wells of **Figure 3**, the cells were passaged initially using Accutase's own protocol for cell detachment and suspension. From this experiment the current protocol was established. The cells were seeded following the usual plating protocol.

Objective: Passage cells successfully from one culture vessel to another. Success is determined by cell attachment on day 1 after passaging.

006-02 – Second run differentiation of MNPs to MNs

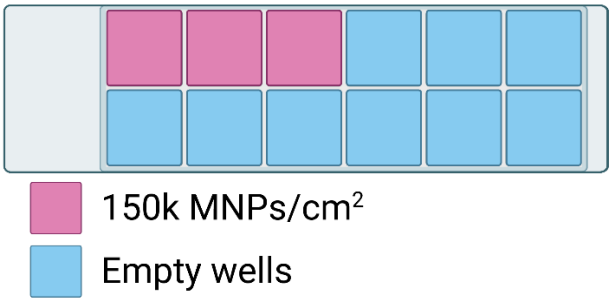

Figure 4. BioRender illustration of a 12-well ibidi slide.

Figure 4 shows a 12-well slide coated with PDL-VTN. This differentiation is the one described by the differentiation protocol of Axol done earlier.

Objective: Differentiate successfully the MNPs to MNs for 15 days. The success is determined by morphological changes using the single reference image Axol has and positive staining for MNs, e.g. TUJ1.

6.2.3 007 – First thawed cryovial

This experiment mainly showcased the validation of the cryopreservation and thawing protocols working for the MNPs.

007-01 – MNPs successfully survive after cryopreservation

The cells are thawed following the established protocol and during the cell counter they are assessed if their alive or not.

Objective: Have enough living cells to seed wells at 150k cells/cm^2 for both 24-well plates and 12-well Ibidi slides. The cells are assessed as living through the cell counter results and cell attachment on day 1 after thawing and seeding.

007-02 – MNPs maintained differentiation potential after cryopreservation with Axol and MNDM

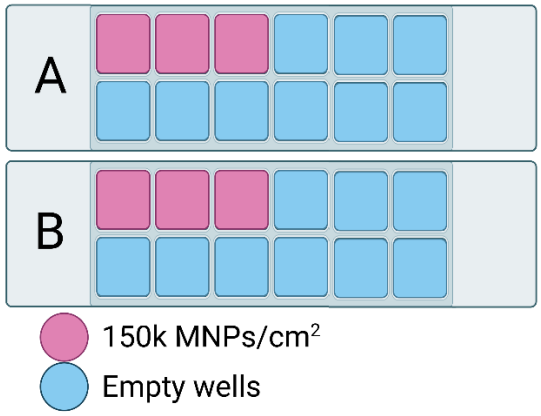

Figure 5. BioRender illustration of a 12-well ibidi slide, for both A) the axol protocol and B) the MNDM protocol.

Figure 5 shows the two 12-well Ibidi slides posed for differentiation, (A) following the same experimental set-up as 005-01 and (B) following the Differentiation protocol from this report. The cells were extracted from one single cryovial and the seeding density accounted only for the live cells from the cell counting results.

Objective 1: Demonstrate that after the cryopreservation protocol the MNPs can differentiate successfully to MNs for 15 days. The success is determined by morphological changes using the single reference image Axol has and positive staining for MNs, e.g. TUJ1.

Objective 2: Have comparable results with the same assays as objective 1 using the MNDM differentiation protocol and Geltrex as the differentiation substrate.

007-03 – MNPs maintained expansion potential after cryopreservation

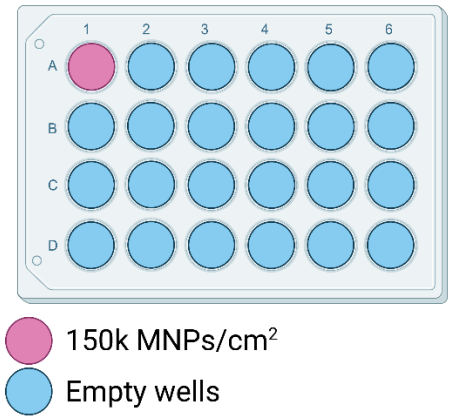

Figure 6. BioRender illustration of the seeding of MNPs in a 24-well plate.

Figure 6 shows a 24-well plate seeded with thawed MNPs from the cryopreservation protocol. The same coating, seeding, and culture conditions as experimental set-up 005-02 were to be followed.

Objective: Demonstrate that the MNPs can increase their number after undergoing the cryopreservation and thawing protocols.

6.2.4 008 – Second thawed cryovial

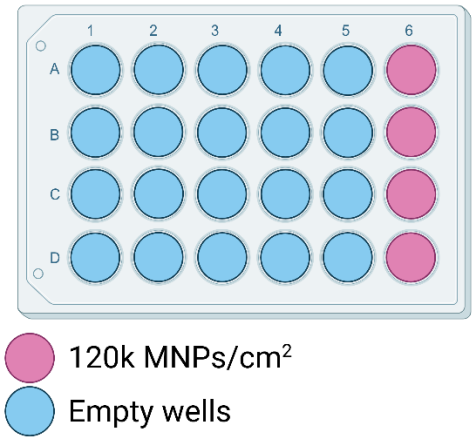

Figure 7. BioRender illustration of the seeding of MNPs in a 24-well plate.

Figure 7 shows the 24-well plate for expansion of the MNPs after another thawed cryovial. The same protocols for expansion and thawing were applied. Only the expansion was pursued for this passage to focus on getting more cells.

Objective: Demonstrate that the MNPs after cryopreservation maintain their expansion potential by their increase in number.

6.2.5 009 – Passage of the second thawed cryovial

009-01 – Comparison of PDL-VTN and Geltrex as coatings for the expansion protocol

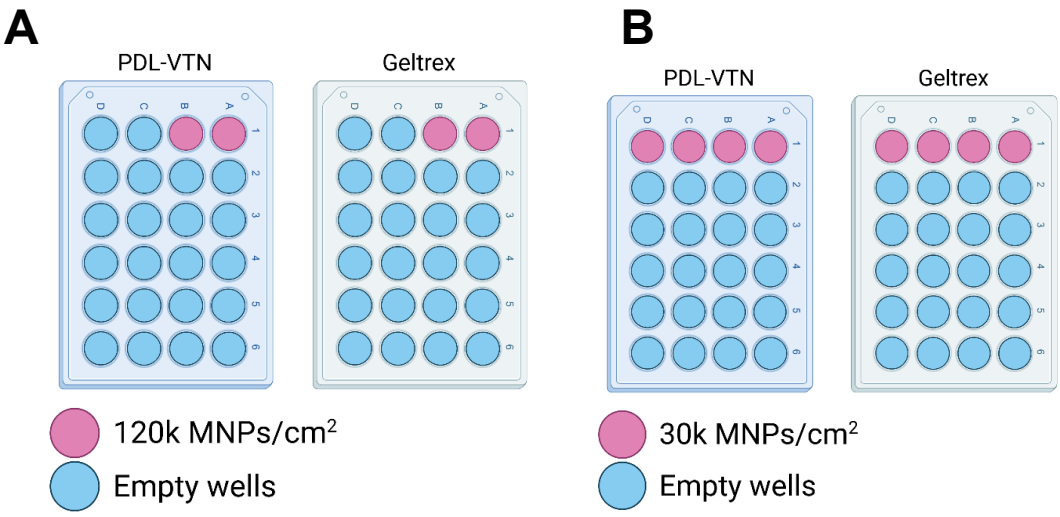

Figure 8. BioRender illustration of the seeding of MNPs in two 24-well plates.

Figure 8A shows two almost identical 24-well plates with the only difference in coating substrates: PDL-VTN recommended by Axol for differentiation, and Geltrex that has insofar worked for expansion. As such, it will be evaluated whether PDL-VTN can yield better results for proliferation than Geltrex. Since the protocol for coating with PDL-VTN is more laborious and takes longer than the Geltrex protocol, it has been decided that PDL-VTN needs to be significantly better than Geltrex for it to be a better alternative. The experiment was repeated with a new passage from the previous experiment but with the experimental set-up shown in **Figure 8B**

Objective: Demonstrate if there is a difference in expansion with different coatings with an increase in number of cells on the day of passage.

009-02 – Alternative differentiation protocol

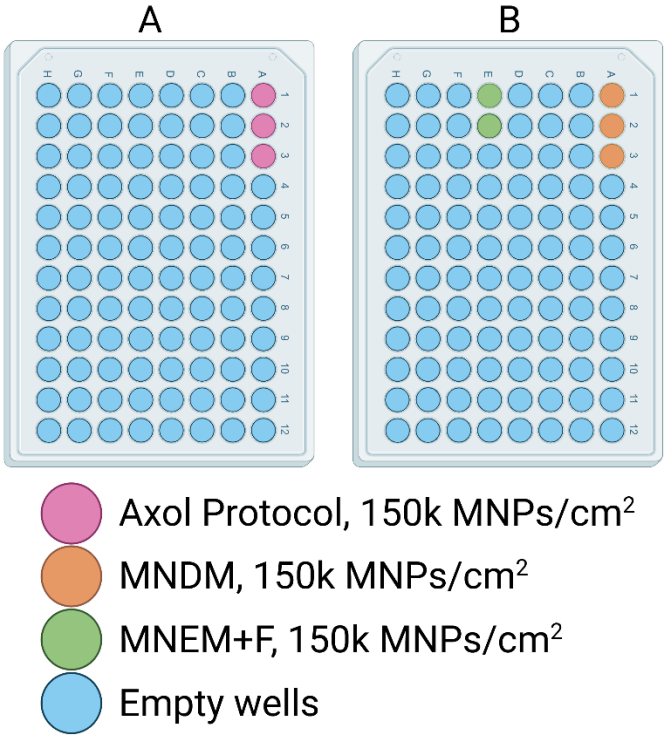

Figure 9. BioRender illustration of two 96-well plates for the second passage.

Figure 9 shows two different 96-well plates with seeded MNPs undergoing different differentiation protocols. One well plate only has the Axol protocol and is used as reference, along with the differentiation protocol established in this report (MNDM) on the other well plate. I wondered if adding the factors that Axol protocol adds to its MNMM medium to induce differentiation will have the same effect if I add them to MNEM, thus MNEM+F stands for MNEM and neurotrophic factors under the same concentrations as established by Axol: brain-derived neurotrophic factor (BDNF), ciliary neurotrophic factor (CNTF), and glial-derived neurotrophic factor (GDNF).

Objective: Demonstrate whether there is potential of using MNEM also as a differentiation medium with the addition of factors that induce motor neuron differentiation. This is assessed by morphological changes.

6.2.6 010 – Third passage of the second thawed cryovial

The third passage is derived from the Geltrex group from the second run of experiment 009-01 (which is the second passage for these cells).

010-01 – Differences in cell density for differentiation

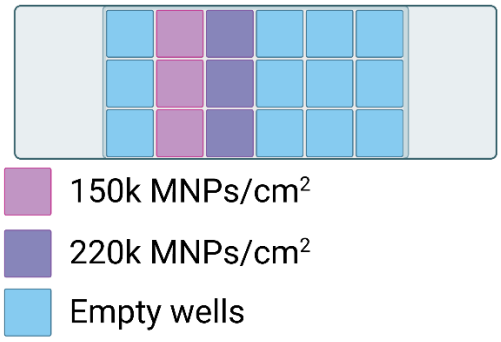

Figure 10. BioRender illustration of the seeding of MNPs in an 18-chamber Ibidi glass slide (81816).

Figure 10 shows the differentiation conditions for the MNPs at different seeding densities. The wells were coated with Geltrex and the differentiation medium from Axol was followed per its protocol. Two identical slides were seeded with these specifications.

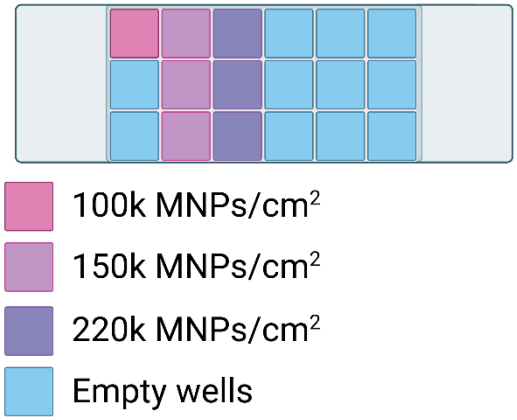

Figure 11. BioRender illustration of the seeding of MNPs in an 18-chamber Ibidi glass slide.

Figure 11 shows the differentiation conditions for the MNPs at different seeding densities. The cells were seeded on a Geltrex coating and differentiated using MNDM and MNDM+E. There are two of these slides and unfortunately the lowest density condition was only enough for one well, as the volume of the cell suspension ran short, and the seeding started from the highest condition to the lowest.

Objective: Observe if higher seeding densities have an earlier differentiation than lower seeding densities, through morphological cues.

010-02 – Calcium imaging with the 010-01 cells

Calcium imaging was done to gauge the functionality of the neurons after 7 and 15 days of differentiating. The cells were imaged after following the calcium imaging protocol for 1 minute at different exposure times: 5 milliseconds for the first time point and 100 milliseconds for the latter one. Although the cells were still alive after imaging, this served as an endpoint assay and were subsequently discarded. Furthermore, the cells were stimulated using Biond's in-house muscle stimulator.

Objective: Observe spontaneous firing of the cells as understood by the intensity of calcium concentration. "Firing" is considered to be occurring when the intensity of the calcium signal is larger than both a previous moment in time in the same cell and relative to the background intensity.

6.2.7 011 –Third thawed cryovial

Every passage had in parallel cells in the proliferation stage following the expansion protocol, but no experiments were made in regards of expansion.

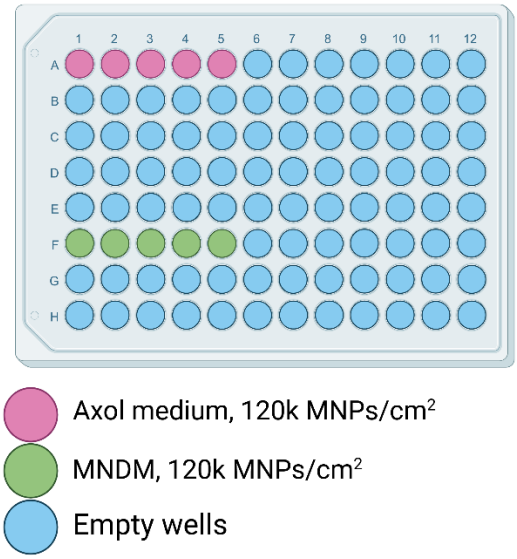

Figure 12. BioRender illustration of the seeding of MNPs in a 96-well plate.

Figure 12 shows a 96-well plate with two rows with different differentiation media, the cells seeded were directly from the cryovial thawing.

Objective: Continue to observe the robustness of the differentiation protocol compared to Axol's.

6.2.8 012 – First passage of the third thawed cryovial

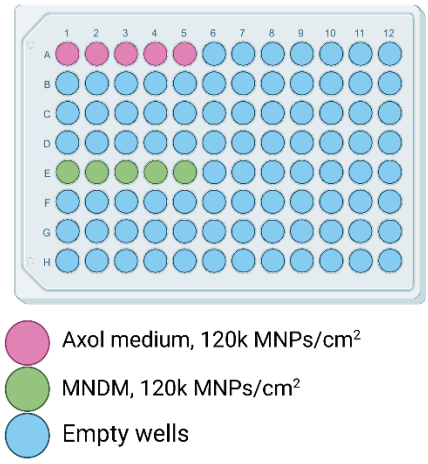

Figure 13. BioRender illustration of the seeding of MNPs in a 96-well plate.

Figure 13 shows a 96-well plate with two rows with different differentiation media of this passage. The cells were cultured until day 10 after seeding and subsequently imaged following the calcium imaging protocol, the exposure time was 100 milliseconds and imaged for 30 seconds at 10 frames per second. Only the columns 3, 4, and 5 were calcium imaged, the rest were sent to LUMC for immunostaining for nuclei (DAPI) and neurofilaments (MAP2 or TUJ1).

Objective: Demonstrate a more complete differentiation profile of the MNPs through electrical activity as seen by calcium imaging and immunostaining for neurofilaments.

6.2.9 013 – Second passage of the third thawed cryovial

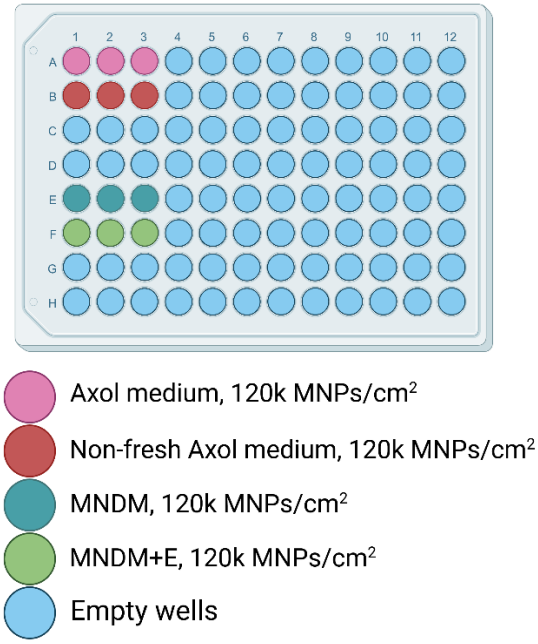

Figure 14. BioRender illustration of the seeding of MNPs in a 96-well plate.

Figure 14 shows a 96-well plate with different differentiation media defined as follows: Axol, following Axol's protocol where fresh media is prepared each media-changing day; AxolnF, which is Axol media prepared on day 1 and continued being used for following media changes despite not being fresh; MNDM, which follows the differentiation protocol outlined in here; and MNDME, which has compound

E added since day 0 to the medium instead until day 6. The cells were also stained for actin (Phalloidin) and nuclei (DAPI).

Objective 1: Determine if non-fresh media still has a differentiation effect as compared to freshly made.

Objective 2: Determine if the addition of compound E helps accelerate the differentiation as compared to the established protocol.

6.3 005 – First Motor Neuron Progenitors run

6.3.1 005-01 – Axol's differentiation protocol of MNPs

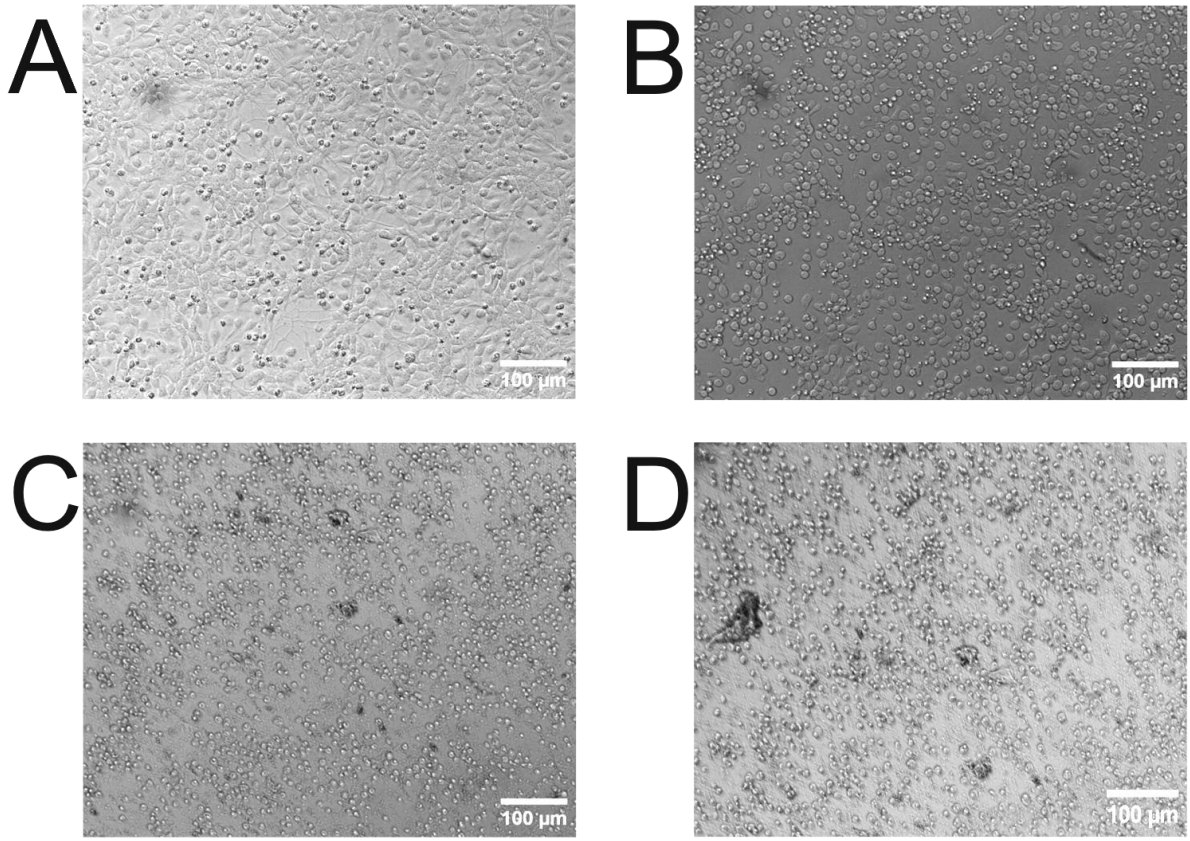

Figure 15. MNPs undergoing Axol's protocol differentiation in 12-well Ibidi glass slides for days A) 1, B) 2, C) 5, and D) 7.

Figure 15 shows the differentiation of the MNPs following Axol's protocol on 3 wells of two 12-well Ibidi slides with one key difference explained shortly. The cell viability started to decline on day 2 (B), with widespread death starting on day 5 (C). At the time, unsure how the MNPs should look like as they grow, the cells were imaged for later days. Though most cells died and started to explode, single digits of cells were found across all 6 wells that exhibited some neurite growth. Evidently, this differentiation run was a dud and stands as an example of what happens when something goes wrong. The culprit is most likely the overdosing of retinoic acid, as a miscalculation led the Axol differentiation medium to have 50x more retinoic acid than it should have. This was corrected for later passages. Alas, it will not be the only example of what not to do with the MNPs.

Objective: Differentiate successfully the MNPs to MNs for 15 days. The success is determined by morphological changes using the single reference image Axol has and positive staining for MNs, e.g. TUJ1. **Results**: MNPs were not differentiated and died due to an overdose of retinoic acid. Failure.

6.3.2 005-02 – Expansion of MNPs with MNMM4P on D0

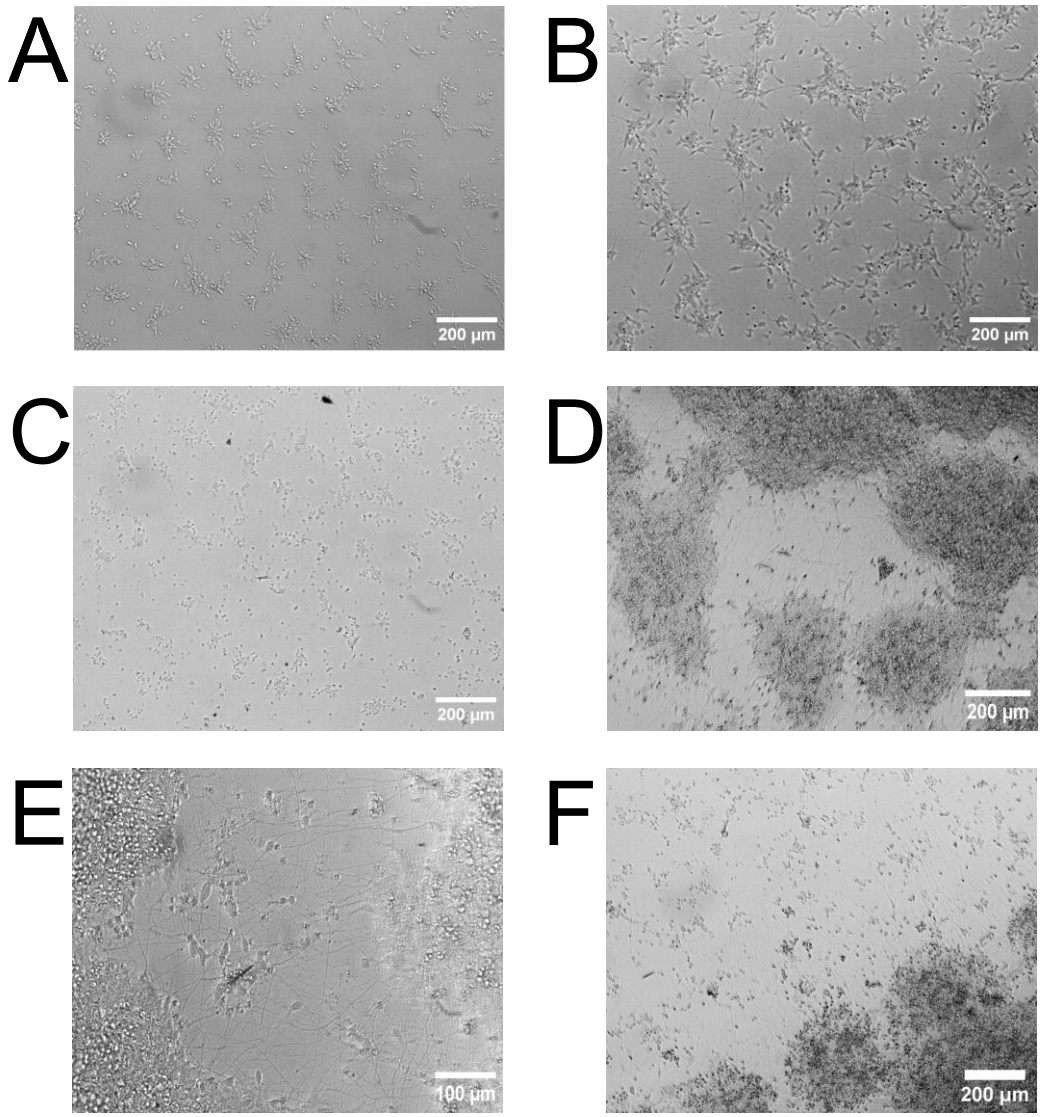

Figure 16. MNPs seeded with MNMM4P and then cultured with MNEM on Geltrex coating for days A) 1, B) 2, C) 6, D) 7, E) 8, and F) 11.

Figure 16 shows the evolution of MNPs seeded for expansion of the B1 well, other wells were cultured until day 7 (D). This condition started with day 0 using the Motor Neuron Maintenance Medium for Plating as described by Axol and then changed to MNEM on day 1. It was observed that the growth of the MNPs is apparently slower than the condition which plated the MNPs with MNEMi on day 0 and other wells of the same condition. However, the key morphology was still present: MNPs forming colonies while also extruding neurites.

Objective: Increase the number of MNPs and maintain their differentiation potential, which can be seen with a differentiation run after passaging. **Results**: MNPs were expanded, but differentiation was not confirmed. Partial success.

6.3.3 005-03 – Differentiation induction of the 005-02's A1

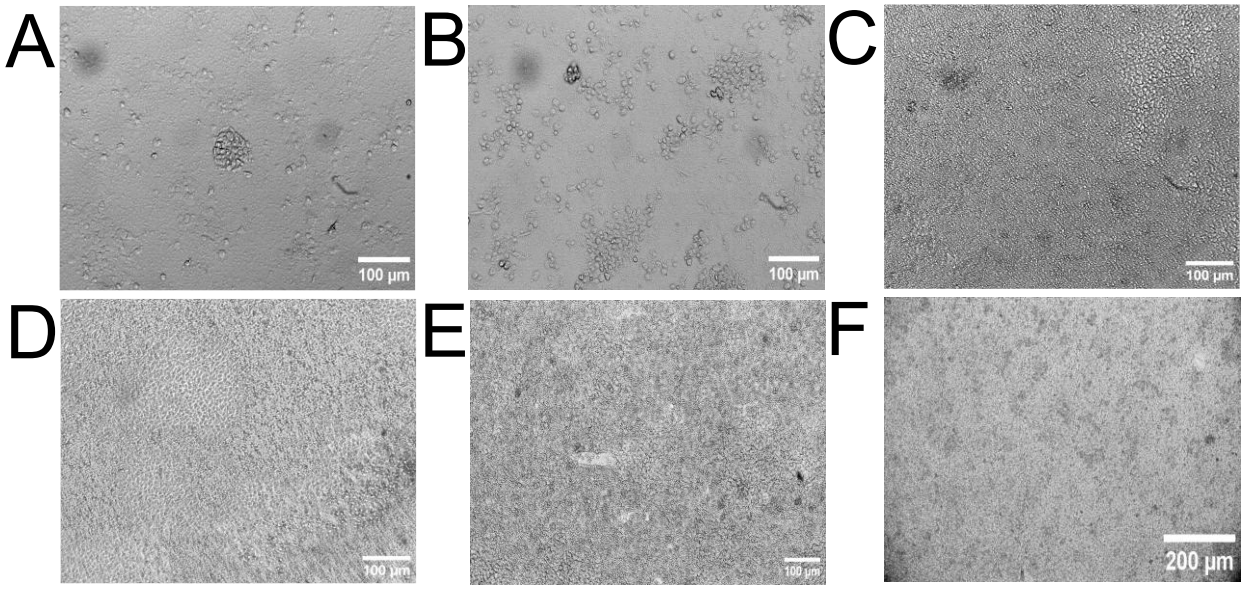

Figure 17. MNPs seeded originally under MNEM on Geltrex coating and then differentiated with Axol's protocol for days A) 1, B) 2, C) 5, D) 7, E) 9 and F) 10 after starting the differentiation.

Figure 17 shows what would happen if the medium of the MNPs culture was changed from expansion to differentiation. The results show that the cells did not undergo significant morphological changes and continued proliferating eventually creating a cellular monolayer, as seen from day 5 (C). This result suggests that it is hard to change the cells' proliferation path to differentiation without passaging the cells. However, this was but an exploratory small experiment, so it is hard to draw a robust conclusion from a single experiment.

Objective: Through morphological changes, assess if the MNPs change into MNs. **Results**: The MNPs did not undergo morphological changes that could tell they were MNs. Failure.

6.3.4 005-04 – Expansion of MNPs with MNEMi

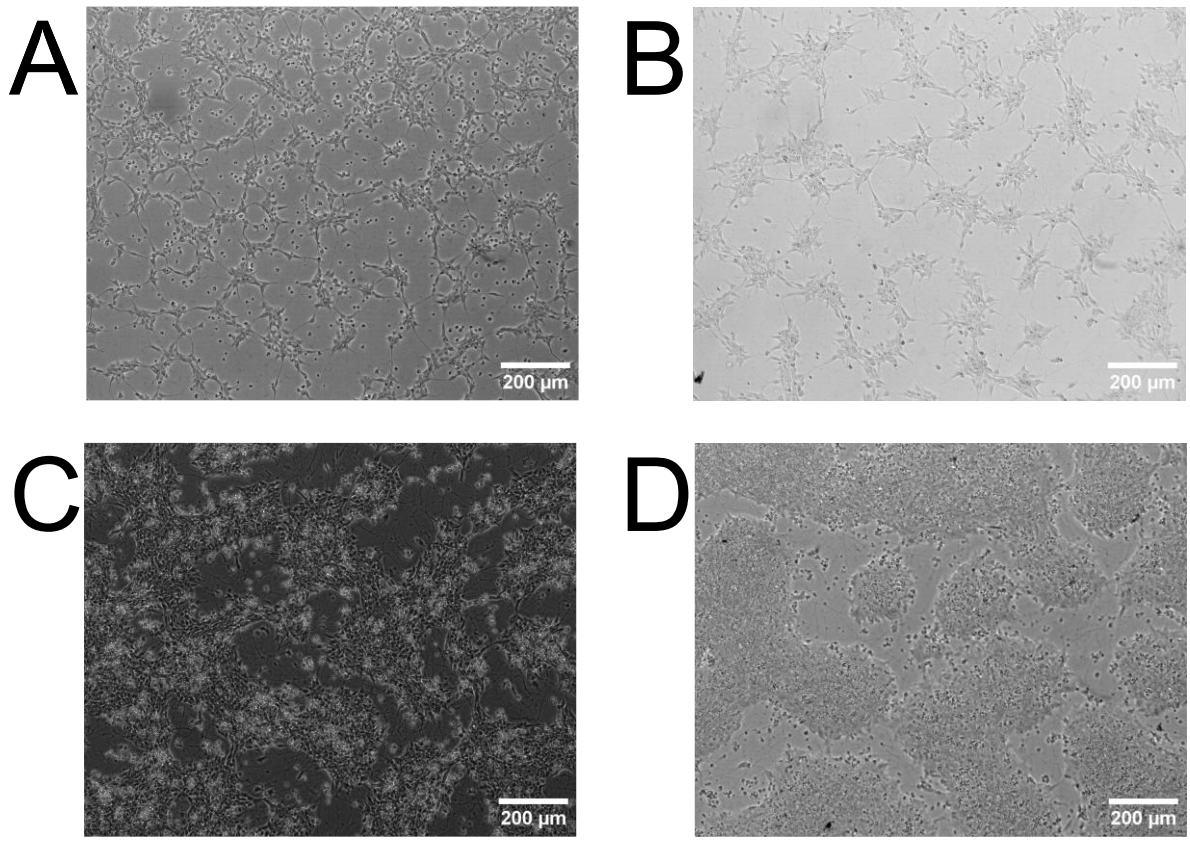

Figure 18. MNPs seeded with MNEMi on Geltrex coating for days A) 1, B) 2, C) 5, and D) 7.

Figure 18 shows the expansion of MNPs in a 24-well plate coated in Geltrex with MNEM since D0. The MNPs were grown for one week and achieved good morphology. These cells were further passaged from 2 wells of the 24-well plate to 5 wells of the 24-well plate and into 6 wells of the 12-well Ibidi slides. This result established early the viability of Geltrex and MNEM for expansion, though the differentiation potential retention was still needed to be observed to call this a truly successful run.

Objective: Assess whether MNEMi is a viable plating medium compared to MNMM4P in increasing the number of MNPs and maintaining their differentiation potential. **Results**: MNPs were successfully plated with MNEMi for expansion, but not differentiation. Partial success.

6.4 006 – First Passaging

6.4.1 006-01 - Passaging protocol validation

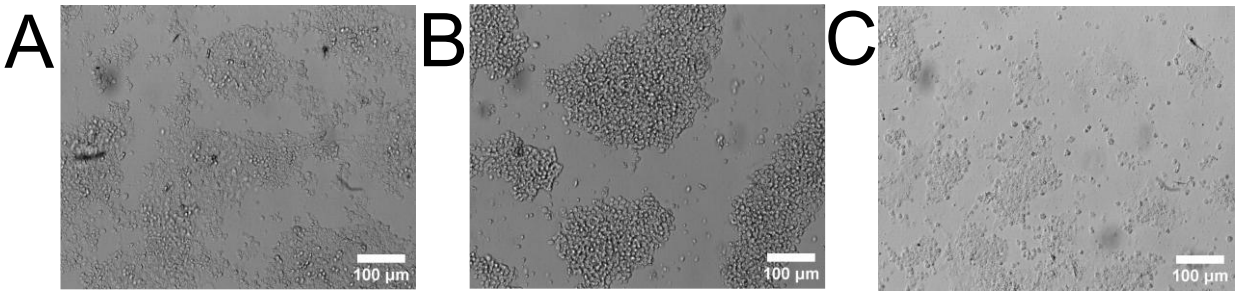

Figure 19. MNPs undergoing detachment following the protocol of Accutase after A) 5 minutes, B) 10 minutes, and C) 15 minutes.

Figure 19 shows the detachment progress of the MNPs after being incubated with Accutase. Though the protocol calls for 5-10 minutes of incubation time to have suspended cells, this was never observed for the MNPs. It was then suggested that it was possible to detach them by pipetting up and down the Accutase with the cells to have them lift off. This was proven to be successful and that it also doesn't need to wait 15 minutes, since 10 minutes was found to have similar results.

Expansion potential after passaging

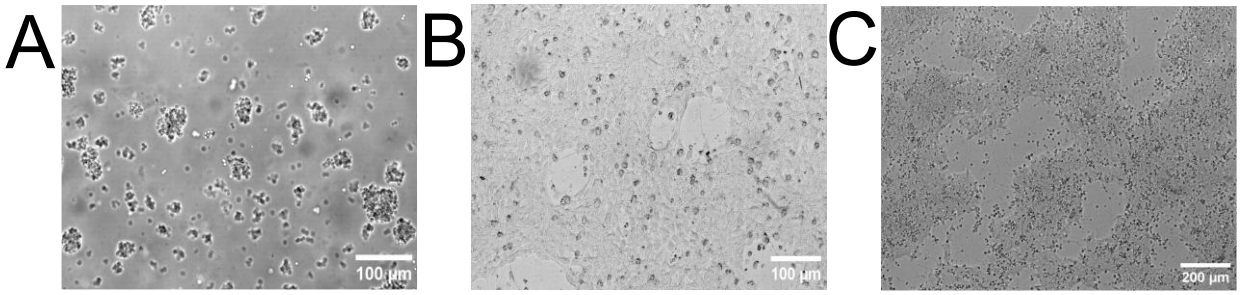

Figure 20. MNPs seeded with MNMM4P and then cultured with MNEM after their first passaging on Geltrex coating for days A) 0, B) 1, and C) 3.

Figure 20 shows the growth of the A+MNEM condition on its second passage on a 24-well plate with Geltrex coating. In this case, the cells of one well from the previous seeding were seeded on 2 wells of the new one. Unlike as before, MNEM was added from D0 instead from D1. The growth looks favourable as seen above and the in the last day the MNPs were frozen.

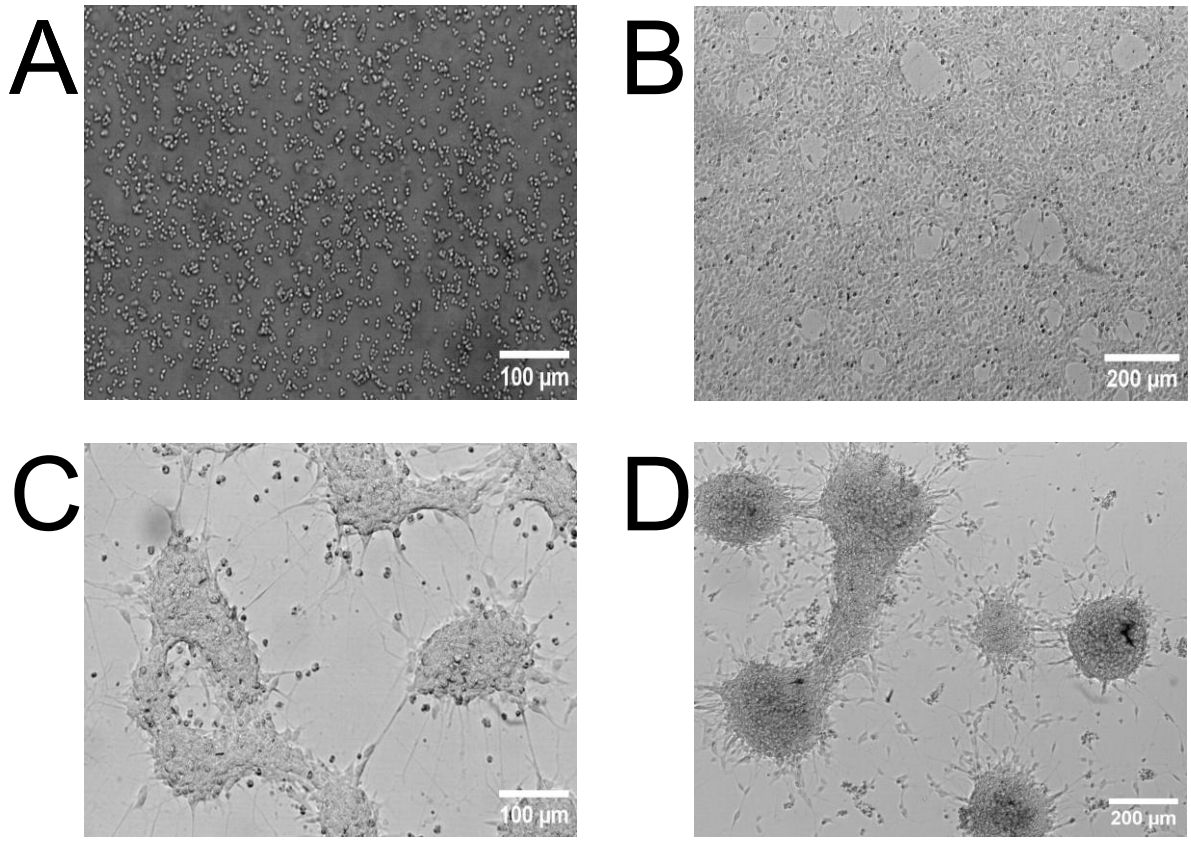

Figure 21. MNPs seeded with MNEMi and then cultured with MNEM after their first passaging on Geltrex coating for days A) 0, B) 1, C) 2 and D) 5.

Figure 21 shows the second passage of the MNEM condition as before. The cells continued to exhibit promising morphology by forming colonies and neurites. These same cells were passaged for differentiation as seen on Figure #. As stated before, five wells were seeded, and they achieved largely the same results. However, on day 5 (D) the MNPs started to compact even more within their colonies and started to create round, spheroidal masses that showed signs of detachment. At the time this behaviour was seen as positive, and it was not realized that the MNPs were detaching. The cells were subsequently frozen.

Objective: Passage cells successfully from one culture vessel to another. Success is determined by cell attachment on day 1 after passaging. **Results**: Cells were successfully passaged from one culture vessel. Success.

6.4.2 006-02 – Second run differentiation of MNPs to MNs

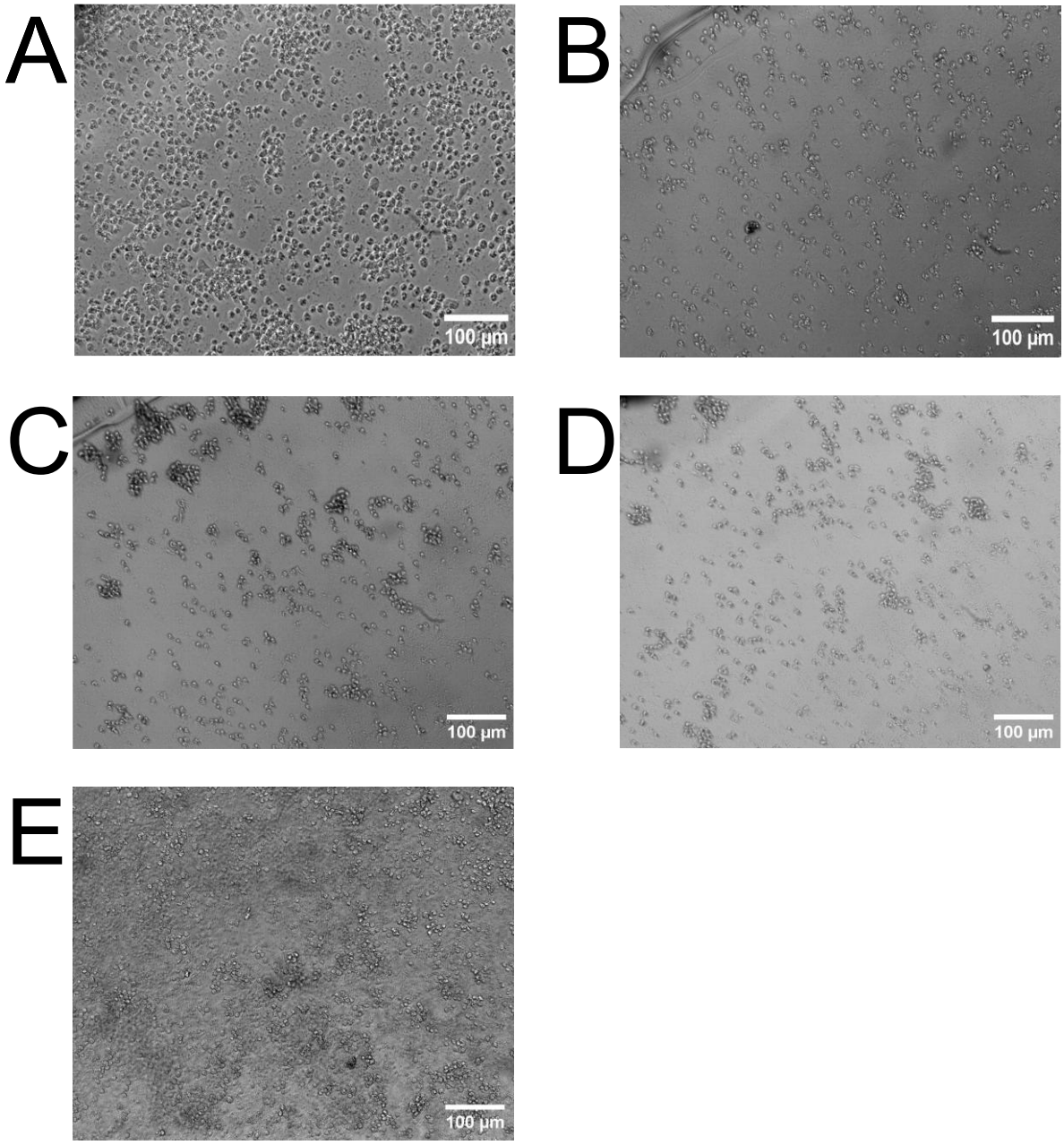

Figure 22. MNPs differentiated following Axol's protocol on 12-well Ibidi slides for days A) 0, B) 1, C) 2, D) 5 and E) 6

Figure 22 shows the attempted differentiation of the second passage from the MNEM condition. As it can be observed, this differentiation run was also a failure, although this was due to inadequate coating conditions from the PDL-VTN coating, as it was too dry when the cells were seeded. Alas, another thing not to do.

Objective: Differentiate successfully the MNPs to MNs for 15 days. The success is determined by morphological changes using the single reference image Axol has and positive staining for MNs, e.g. TUJ1. **Results**: The differentiation was not possible due to a coating mistake. Failure

6.5 007 – First thawed cryovial

6.5.1 007-01 – MNPs successfully survive after cryopreservation

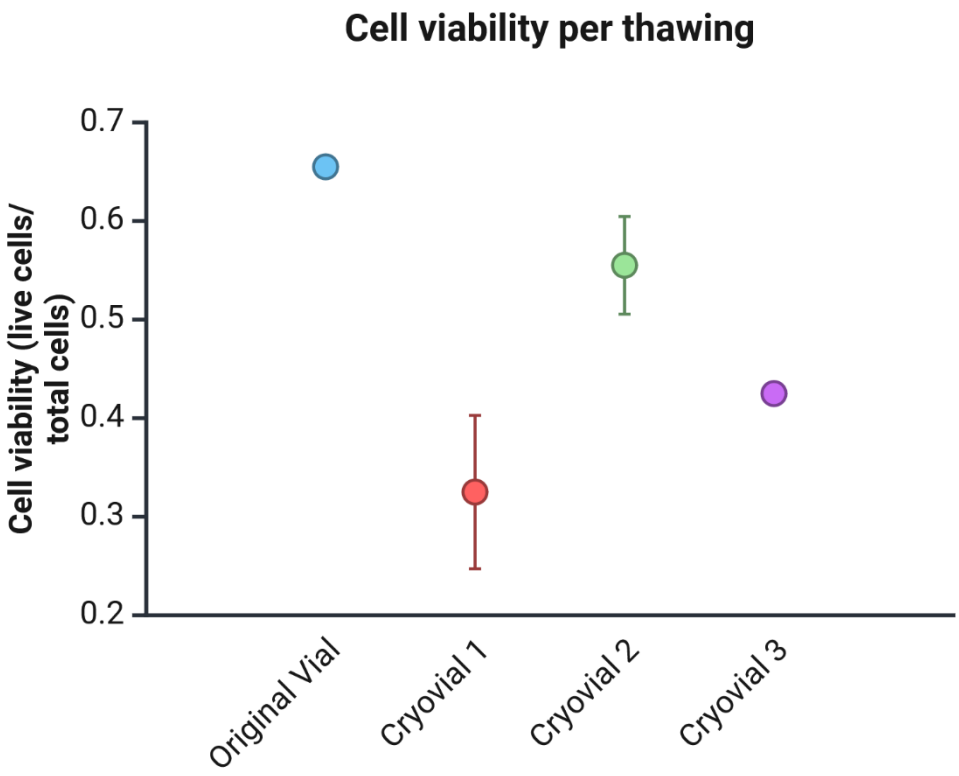

Figure 23. Plot of the viability of the cells after thawing.

Figure 23 shows a plot of the viability of the cells after thawing. While no cryovial was able to replicate the viability of the vial provided by Axol, the fact that cells were still alive and able to expand and differentiate is enough to call this a success.

Objective: Have enough living cells to seed for expansion and proliferation. The cells are assessed as living through the cell counter results and cell attachment on day 1 after thawing and seeding. **Results**: Enough cells survive to continue expanding them and differentiate them. Success.

6.5.2 007-02 – MNPs maintained differentiation potential after cryopreservation with Axol and MNDM

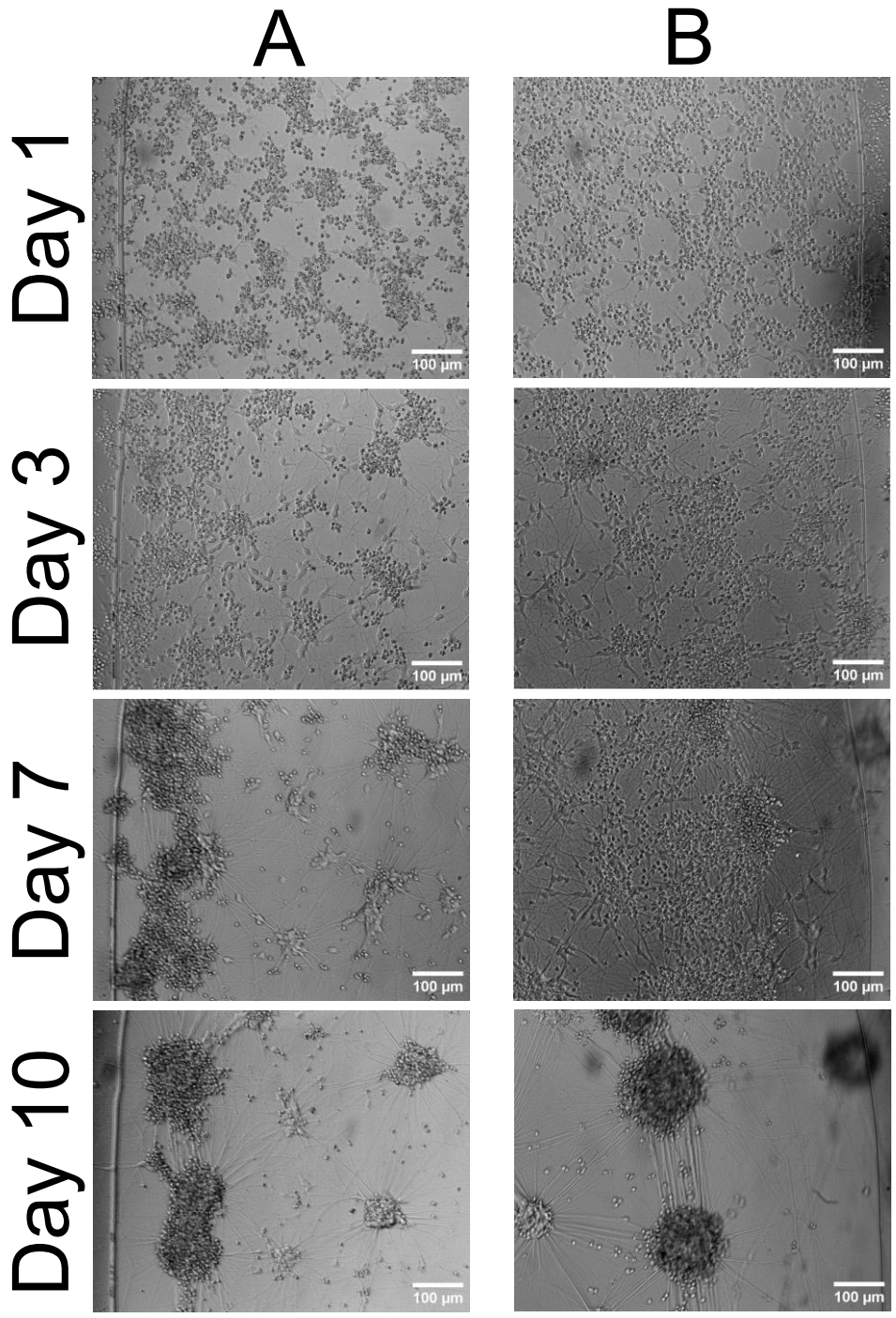

Figure 24. MNPs differentiated on a 12-well Ibidi slides following A) Axol's protocol and B) the MNDM protocol.

Figure 24 shows the differentiation of cells in a specific point of the 12-well Ibidi slides. These results comprise of the best images for a specific region of interest. It can clearly be seen the presence of agglomeration of the MNPs with neurite growth becoming thicker and more direct towards other cell clusters. This is the closest morphology yet to the reference provided by Axol, which is promising news.

The plan was to fix the cells on day 15, unfortunately, the water tray of the incubator dried during the weekend between day 10 and 13, which dried the cells and left them unrecognizable.

Objective 1: Demonstrate that after the cryopreservation protocol the MNPs can differentiate successfully to MNs for 15 days. The success is determined by morphological changes using the single reference image Axol has and positive staining for MNs, e.g. TUJ1. **Results**: Morphological changes were observed, but no neuron specific staining was performed. Partial success.

Objective 2: Have comparable results with the same assays as objective 1 using the MNDM differentiation protocol and Geltrex as the differentiation substrate. **Results**: MNDM had similar morphological results as Axol's CMNMM, but not staining as well. Partial success.

6.5.3 007-03 – MNPs maintained expansion potential after cryopreservation

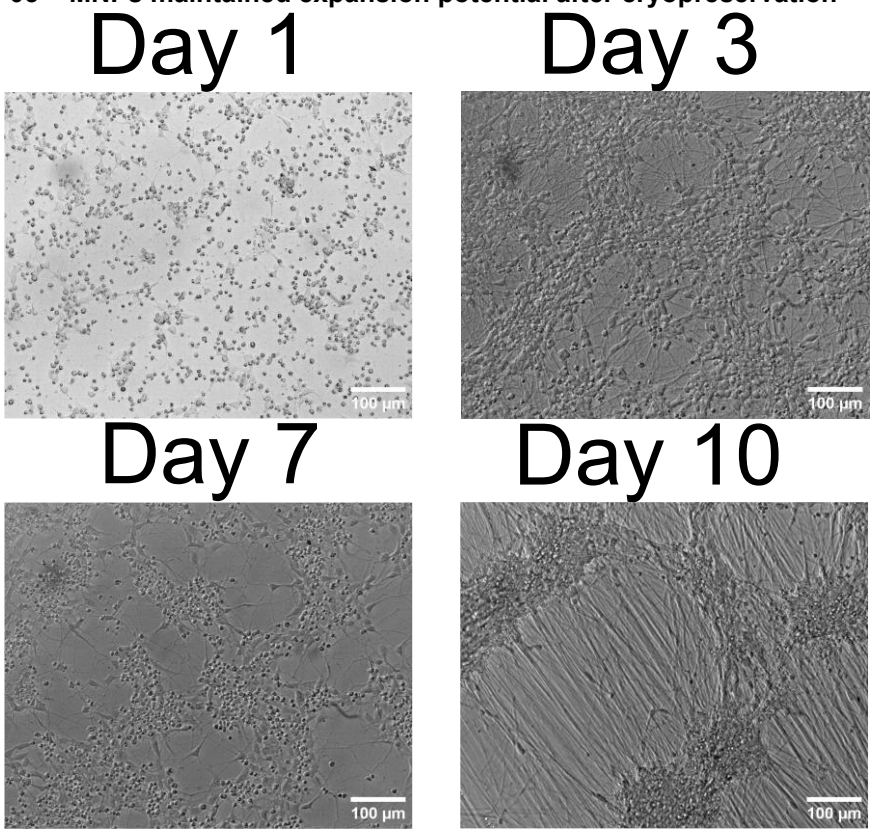

Figure 25. MNPs differentiated on a 24-well plate following the MNDM protocol.

Figure 25 was originally meant to show the expansion of cells, however, I made a mistake and changed the media for day 1 to MNDM instead of MNEM. This was realized the next day, so it was decided that rather than changing the medium yet again, the use of a 24-well plate made of plastic was good for differentiation of the cell comparable to the 12-well Ibidi glass slide. Just as in the previous experiment, there was an observed presence of agglomeration of the MNPs with neurite growth becoming thicker and more direct towards other cell clusters. An interesting point was found with this experiment, cell clusters tended to detach more readily with media changes, as shown on **Figure 25A**; this was not realized at the time as on day 13 the cells were found to be completely detached (**Figure 25B)**, and it was unclear if the drying up had something to do with it.

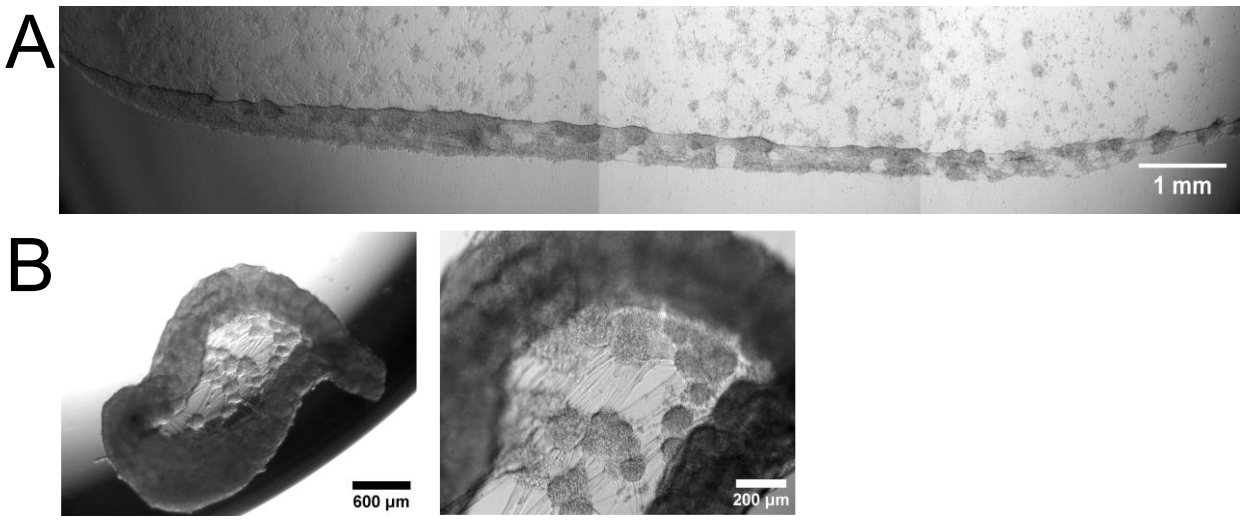

Figure 26. MNPs differentiated on a 24-well plate following the MNDM protocol. A) Zoom out of the well on day 10. B) Different magnifications of the detached cell culture on day 13.

Objective: Demonstrate that the MNPs can increase their number after undergoing the cryopreservation and thawing protocols. **Results**: No expansion was made. Failure

6.6 008 – Second thawed cryovial

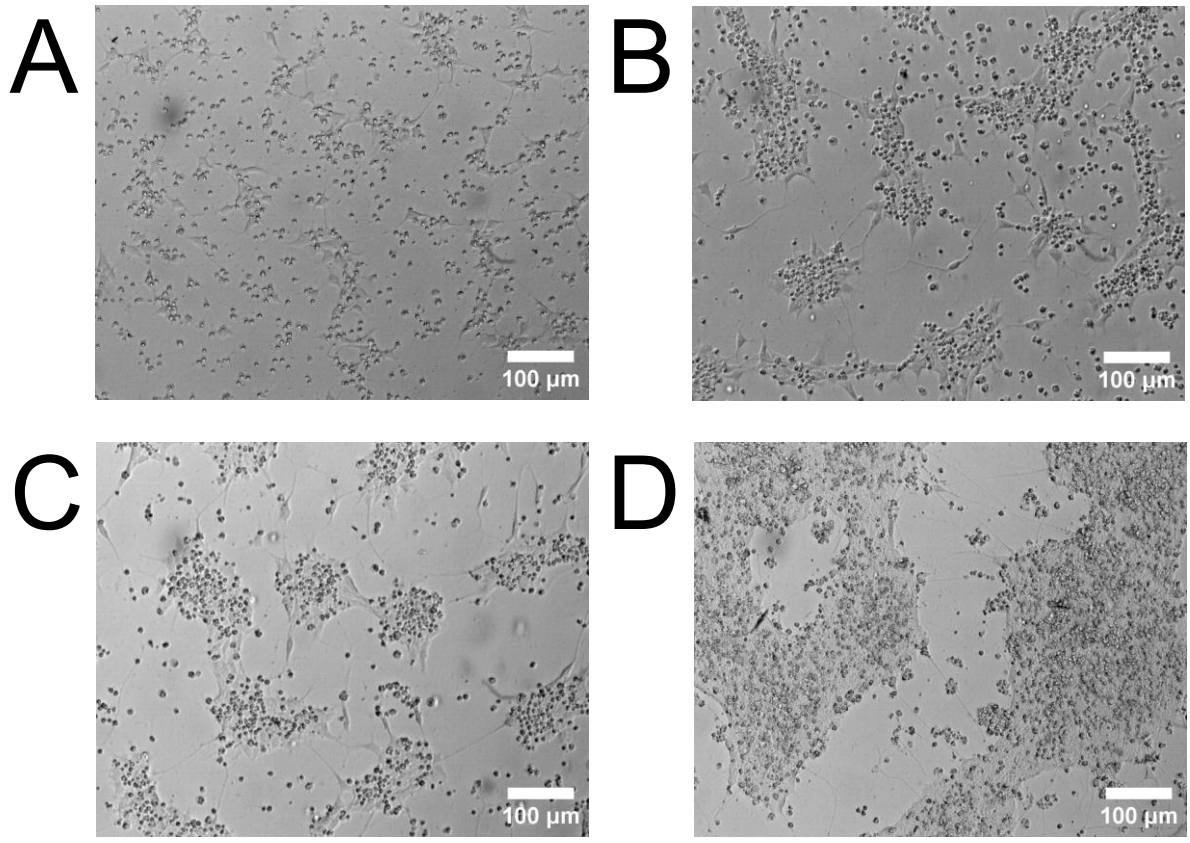

Figure 27. Evolution of MNPs expanded on a 24-well plate for day A) 1, B) 2, C) 3 and D) 6.

Figure 27 shows the expansion of MNPs after thawing. This time the protocol was followed correctly, and the images speak for themselves: expansion potential was maintained and cells got denser as seen on (D). The cells were subsequently passaged.
Objective: Demonstrate that the MNPs after cryopreservation maintain their expansion potential by their increase in number. **Results**: Cells were expanded. Success.

6.7 009 – Passage of the second thawed cryovial

6.7.1 009-01 – Comparison of PDL-VTN and Geltrex as coatings for the expansion protocol

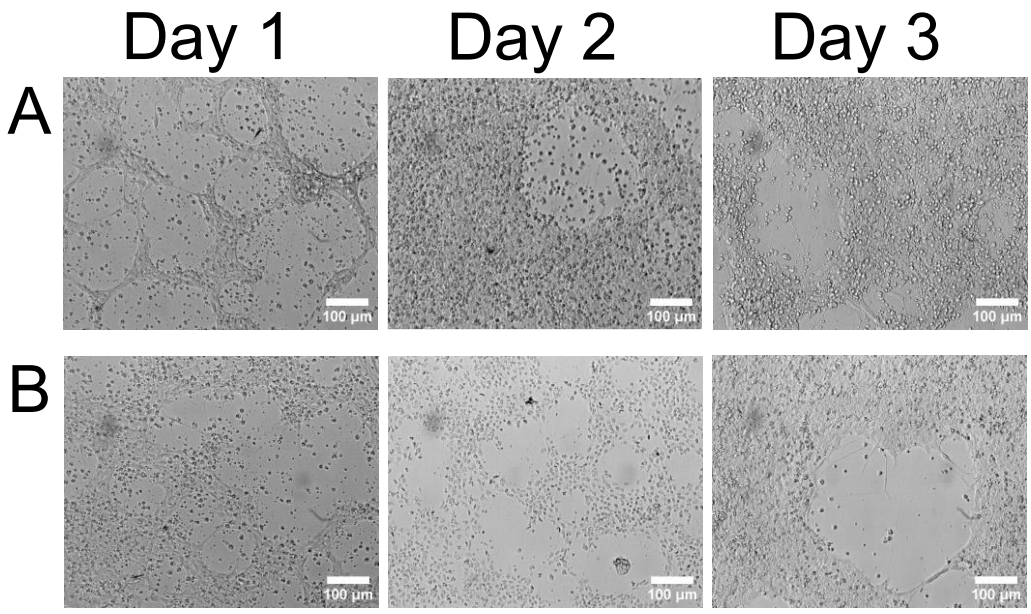

Figure 28. Evolution of MNPs expanded on a 24-well plate with A) Geltrex or B) PDL-VTN as a coating substrate.

Figure 28 shows the proliferation of the MNPs of the first passage of the second cryovial. The cells were initially qualitatively considered to be growing at a faster rate than expected, thus it was decided to passage them again on day 3 after seeding. Both conditions had similar profiles under the microscope, and both were passaged without issues. On the day of passage, the cells (after properly suspending) were counted per individual well following the counting protocol to quantify the expansion.

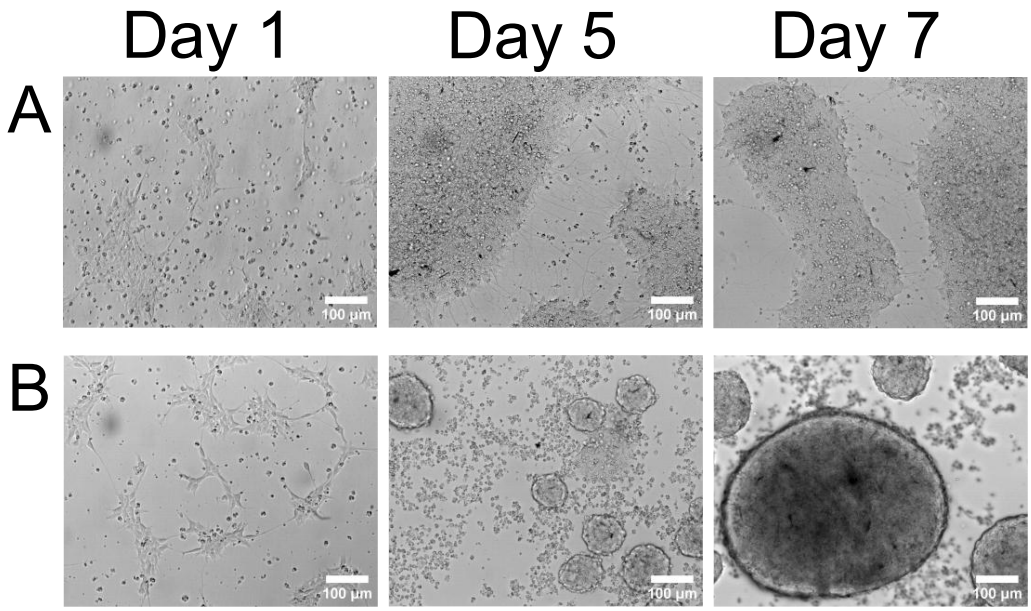

Figure 29. Evolution of MNPs expanded on a 24-well plate with A) Geltrex or B) PDL-VTN as a coating substrate.

Figure 29 shows the proliferation of the MNPs of the second passage of the second cryovial. Until day 4, the cells had similar profiles under the microscope, however, starting on day 5 the cells with the PDL-VTN coating started to detach in an unusual way. Instead of creating a monolayer and then detaching when doing a medium change, relatively small “colonies” unexpectedly started to detach before the medium change was done. The suspended clusters then started to fuse together as seen on day 7. The experiment continued until this point to observe if the effects would continue. On the day of passaging, the cells (after properly suspending) were counted per individual well following the counting protocol to quantify the expansion.

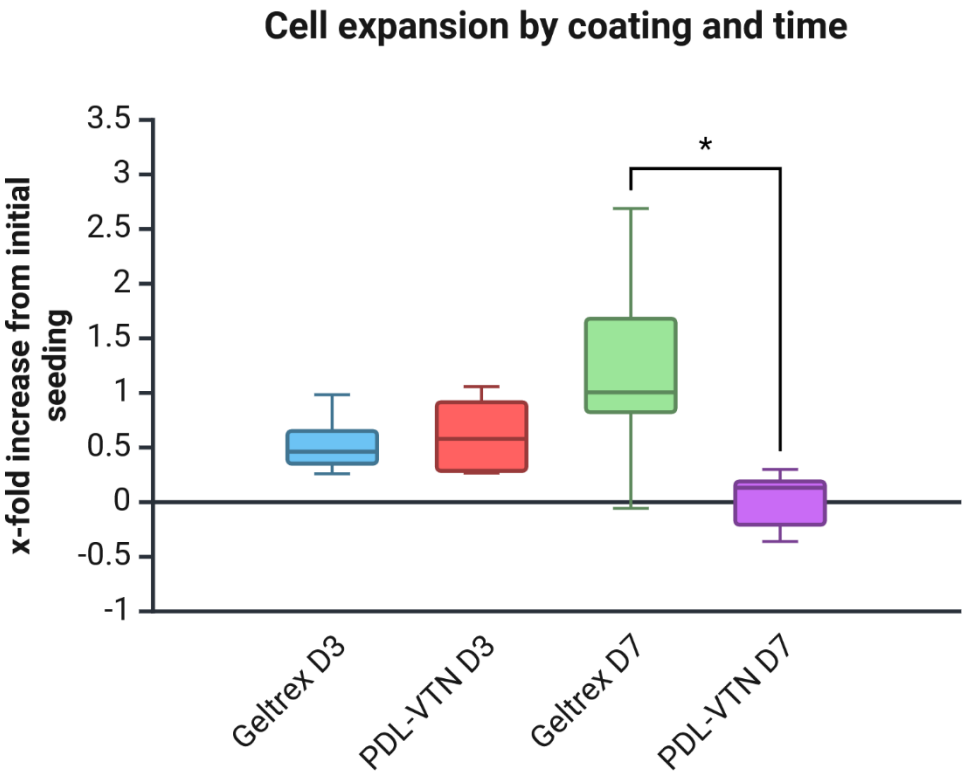

Figure 30. Box and whiskers plot showing the increase of number of cells relative to the seeding density. Done with BioRender.

Figure 30 shows the quantification of cell proliferation relative to the respective seeding density. In this case, D3 group corresponds to the first passage and D7 group corresponds to the second passage. As seen on the previous figure, the wells of the PDL-VTN group of the second passage presented unusual detachment of the cells, leading to lower values measured during the cell counting, with a well having less cells counted than originally seeded. This presents a challenge in drawing conclusions as there is a bias from the cell counting machine against cells clumped together. Nevertheless, it can be said that the early detachment of cells negatively impacts the proliferation potential of cells, contributing to the effect seen on the results. This data, along with the images, helps build the case that using PDL-VTN as coating substrate for expansion is not worth the effort.

Objective: Demonstrate if there is a difference in expansion with different coatings with an increase in number of cells on the day of passage. **Results**: A difference in number of viable cells was observed at a later timepoint between Geltrex and PDL-VTN. Success.

6.7.2 009-02 – Alternative differentiation protocol

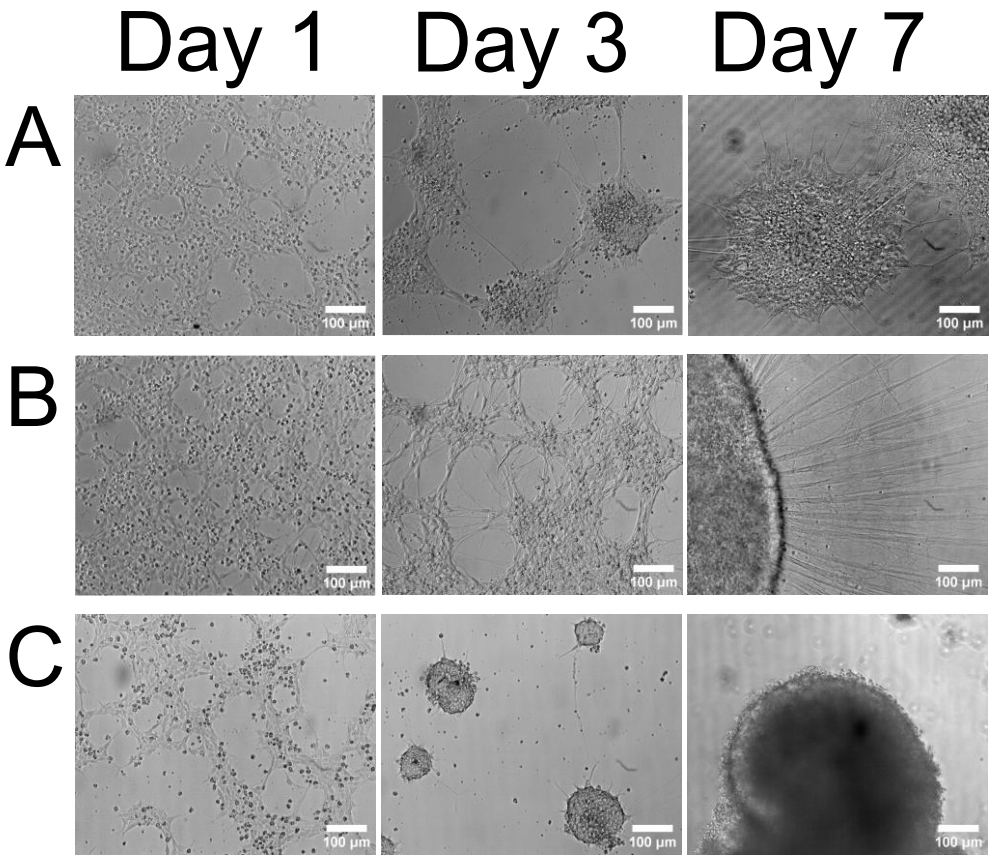

Figure 31. Differentiation of MNPs on 96-well plates cultured in A) MNDM, B) Axol's CMNMM, or C) MNEM with additional differentiation factors.

Figure 31 shows the differentiation evolution between the different groups. It was realized early that adding BDNF, CNTF, and GDNF would not produce the desired outcome. Instead, the cells were easily agglomerating and detaching from the coating without forming either a highly confluent monolayer or axonal growth**.** On the other hand, differentiation under the MNDM protocol was slower than expected, but promising, and the Axol's protocol differentiation actually detached as well, but with a clear formation of neurites.

Objective: Demonstrate whether there is potential of using MNEM also as a differentiation medium with the addition of factors that induce motor neuron differentiation. This is assessed by morphological changes. **Results**: The cells with MNEM+F did not share the morphological changes of the other differentiation media.

6.8 010 – Third passage of the second thawed cryovial

6.8.1 010-01 – Differences in cell density for differentiation

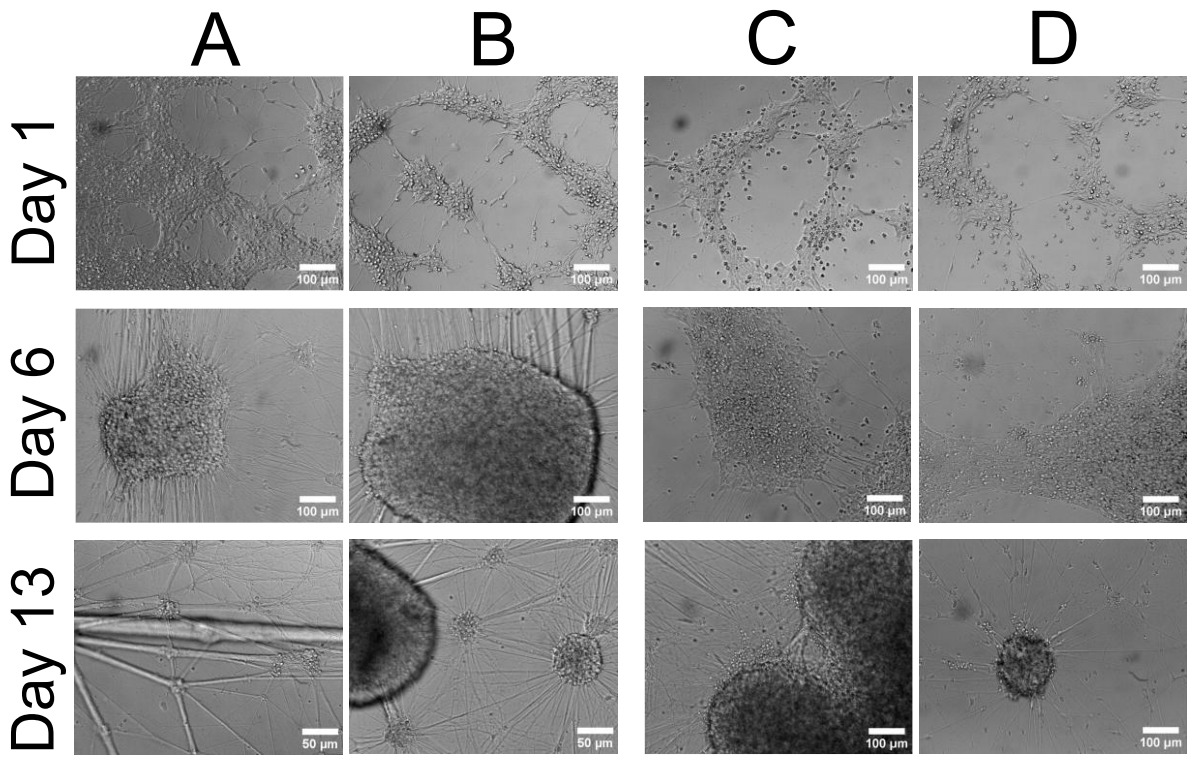

Figure 32. Differentiation of MNPs on 18-well Ibidi slides under different densities and media: A) Axol's CMNMM at 150k cells/cm^2, B) Axol's CMNMM at 220k cells/cm^2, C) MNDMM at 150k cells/cm^2, and D) MNDMM at 220k cells/cm^2.

Figure 32 shows the differentiation of MNPs under different seeding densities. As logically expected, more cells were seen under the higher density conditions and a formation of a monolayer was also quicker, but both looked qualitatively similar by the last day. Another visible difference was that the neurites of the CMNMM groups were thicker and the neuro-sphere they were connected to were also rounder and bigger than the MNDM groups. However, the resulting "more developed" neuro-spheres confirms that they are more easily detachable, and a higher confluency only accelerates this process a day or two.

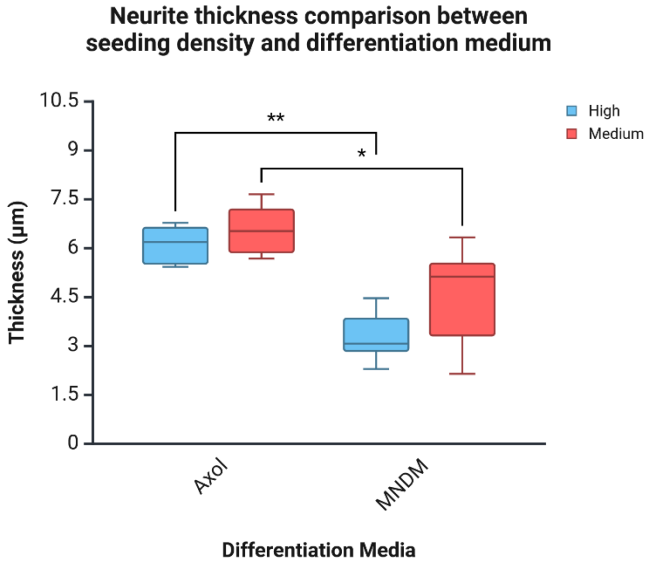

Figure 33. Box and whiskers plot showcasing differences in motor neuron neurite thickness between seeding density and media. * p<0.05. ** p<0.01.

Figure 33 shows the graph comparing the two groups of differentiation media with different seeding densities on day 13 after plating. This result confirms that the cells under CMNMM had a more robust differentiation when compared to the MNDM group. Another interesting result here is that the seeding density of 150k cells/cm^2 is higher than the 220k cells/cm^2 condition. There could be some explanations for this: 1) since the higher density leads to quicker monolayer creation, when neuro-spheres start to form they are closer together and can join with each other more easily or earlier than their lower density counterparts; 2) since only neurites in focus were measured, it could be a bias for larger neurites to be focused on and thus measured than smaller ones. Nevertheless, the results of the measurement and the images show that, given two-week experimental time, there are more disadvantages (waste of cells) than advantages when going for a higher seeding density .

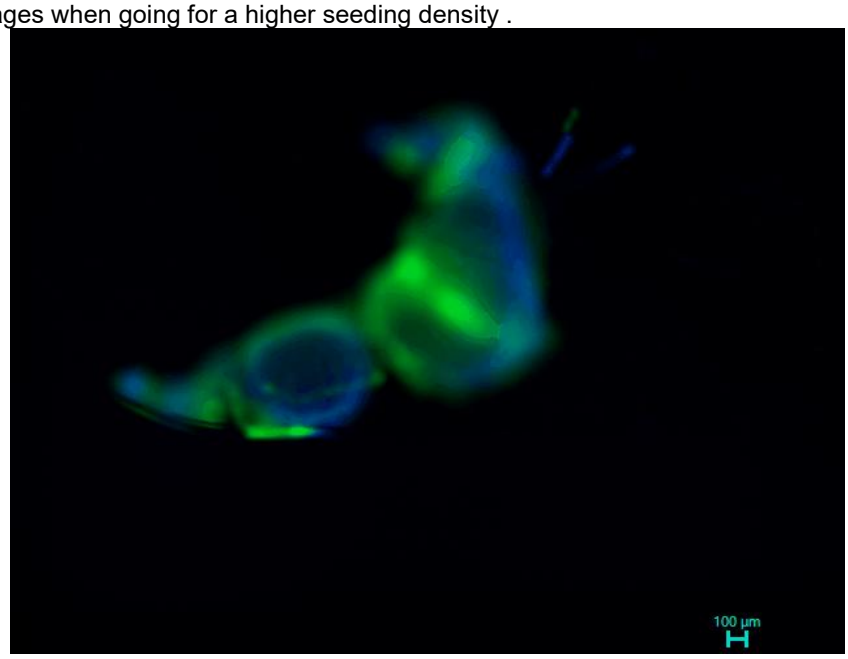

Figure 34. GIF spatial movie through different slices in the Z-axis of the Axol protocol cells differentiated until day 13. Green is MAP2 (neurofilaments) and blue is DAPI (nuclei).

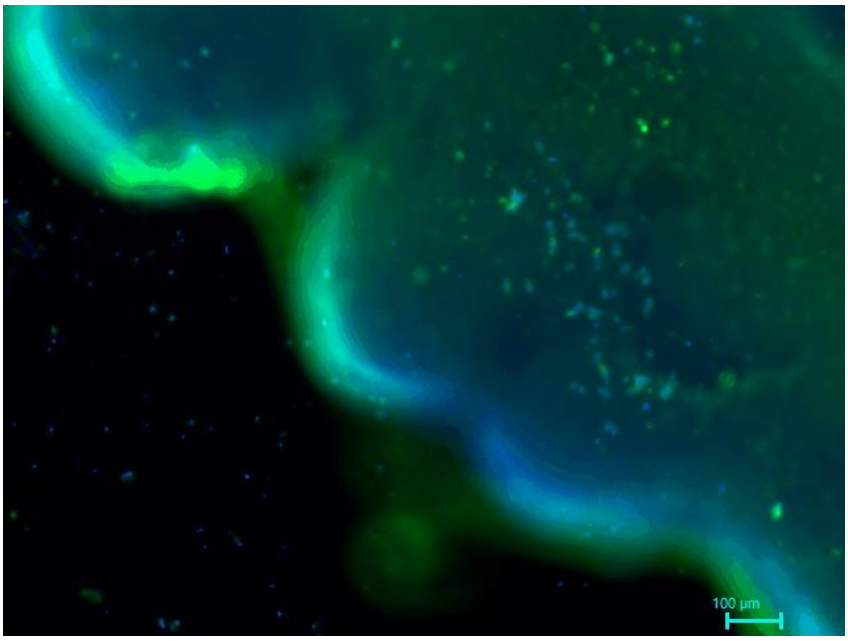

Figure 35. GIF spatial movie through different slices in the Z-axis of the MNDM protocol cells differentiated until day 13. Green is MAP2 (neurofilaments) and blue is DAPI (nuclei).

Figures 34 & 35 show the immunostaining results for the Ibidi slides, both from the 150k cells/cm^2 seeding condition, images from the 220k cells/cm^2 seeding condition were unavailable. The results show that the cells had neurofilaments present, which was expected; unfortunately, the observation of nicely defined neurites is significantly reduced due to the clustering of the cells because of the fixation and immunostaining procedures. Nevertheless, it is nice to have a neuron specific staining for the cells. **Objective**: Observe if higher seeding densities have an earlier differentiation than lower seeding densities, through morphological cues. **Results**: There is a slightly faster differentiation for higher densities, but not enough to justify the use of such density.

6.8.2 010-02 – Calcium imaging with the 010-01 cells

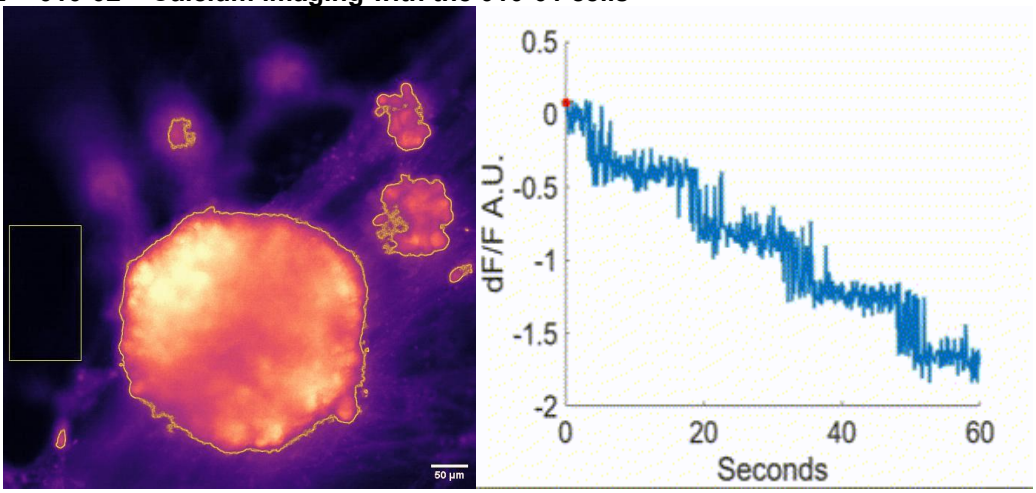

Figure 36. GIF movies of the Axol protocol cells differentiated on day 13 for one minute at 15x speed. 220k cells/cm^2 seeding condition on the right, left indicates intensity normalized to background. Intensity of calcium denoted by bright yellow (high intensity) to deep purple (low intensity).

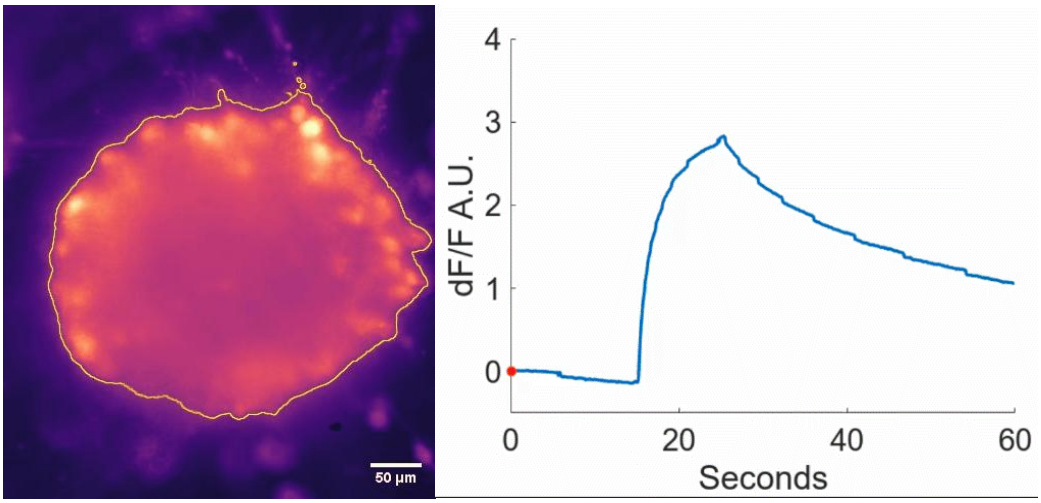

Figure 37. GIF movies of the MNDM protocol cells differentiated on day 13 for one minute at 15x speed. 220k cells/cm^2 seeding condition on the right, left indicates intensity normalized to background. Intensity of calcium denoted by bright yellow (high intensity) to deep purple (low intensity).

Figures 36 & 37 show the calcium imaging movies of the Ibidi slides for the 220k cells/cm^2 seeding conditions, due to time constraints, the cells from condition the 150k cells/cm^2 seeding conditions were not filmed. Their respective plots of the calcium imaging intensity of the ROIs normalized to the background intensity are found on the right, the ROI can be seen within a thin yellow line and the background region in a box with a yellow outline. Both samples move due to the presence of the electrodes in the imaging medium, which are hard to fasten in the well and tend to drift, moving the cells with them. In terms of stimulation, **Figure 37** shows the response of the cells to the stimulation with the release of calcium. While this is very nice to observe, this experiment must have better controls to ascertain that this is indeed electrical response from the cells and not a forceful disruption of the cells that leads to the release of calcium. Examples of such controls include: a dose of a neurotransmitter that triggers electrical activity (for physiological comparison), a dose of potassium chloride to force open voltage-gated channels (to observe the maximum intensity possible), and the introduction of an inhibitor for calcium release (as a negative control).

Objective: Observe spontaneous firing of the cells as understood by the intensity of calcium concentration. “Firing” is considered to be occurring when the intensity of the calcium signal is larger than both a previous moment in time in the same cell and relative to the background intensity. **Results**: No spontaneous activity was found, but a response to a stimulation was observed.

6.9 011 –Third thawed cryovial

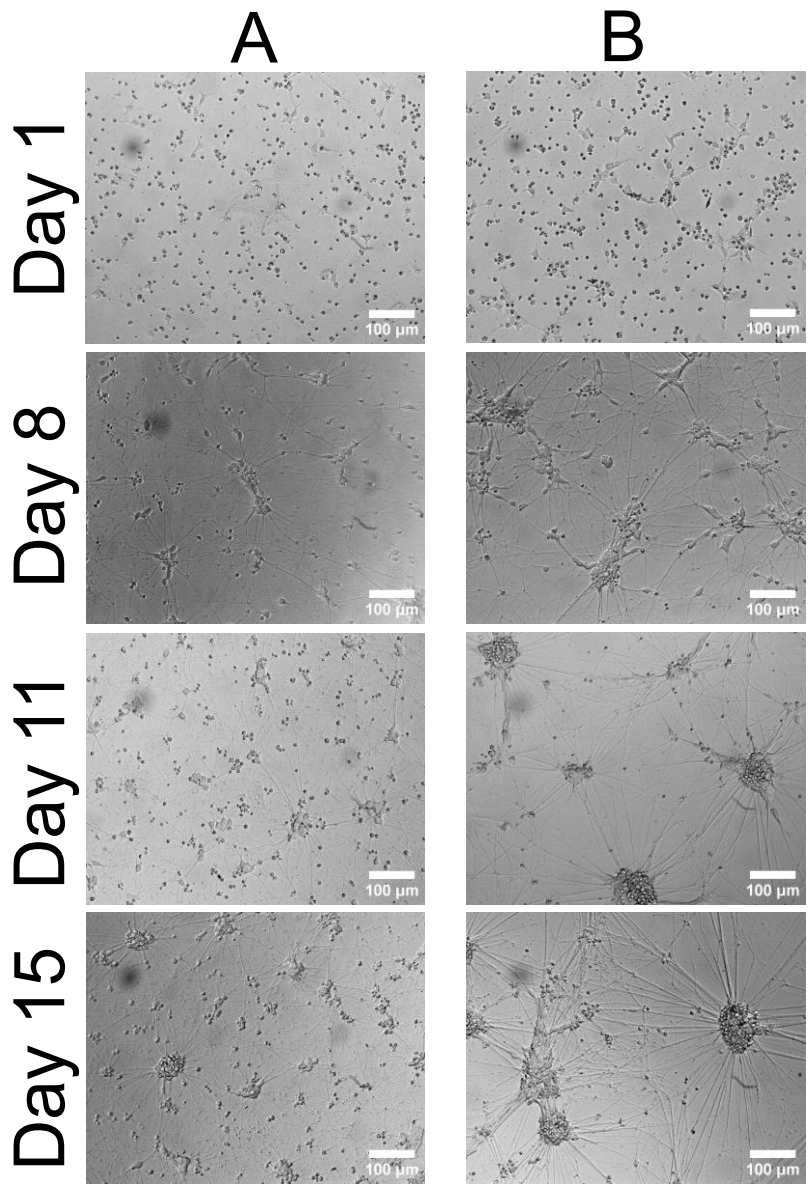

Figure 38. Differentiation of MNPs in a 96-well plate cultured with A) Axol's CMNMM or B) MNDMM.

Figure 38 shows the evolution of differentiation of the MNPs on a 96-well plate. This experimental run yielded a differentiation that was marked by comparably slow growth and the lack of detachment from the neuro-spheres present, as well as their reduced size due to slow growth. This slow growth is attributed to the fact that these cells were directly seeded for differentiation after thawing with a more robust protocol; thus, the cells did not have a proliferation stage that could have a clinging effect after the seeding, leading to more cells that can more easily aggregate together to form the neuro-spheres.
Objective: Continue to observe the robustness of the differentiation protocol compared to Axol's.
Results: Differentiation remained largely similar in terms of morphological changes.

6.10 012 – First passage of the third thawed cryovial

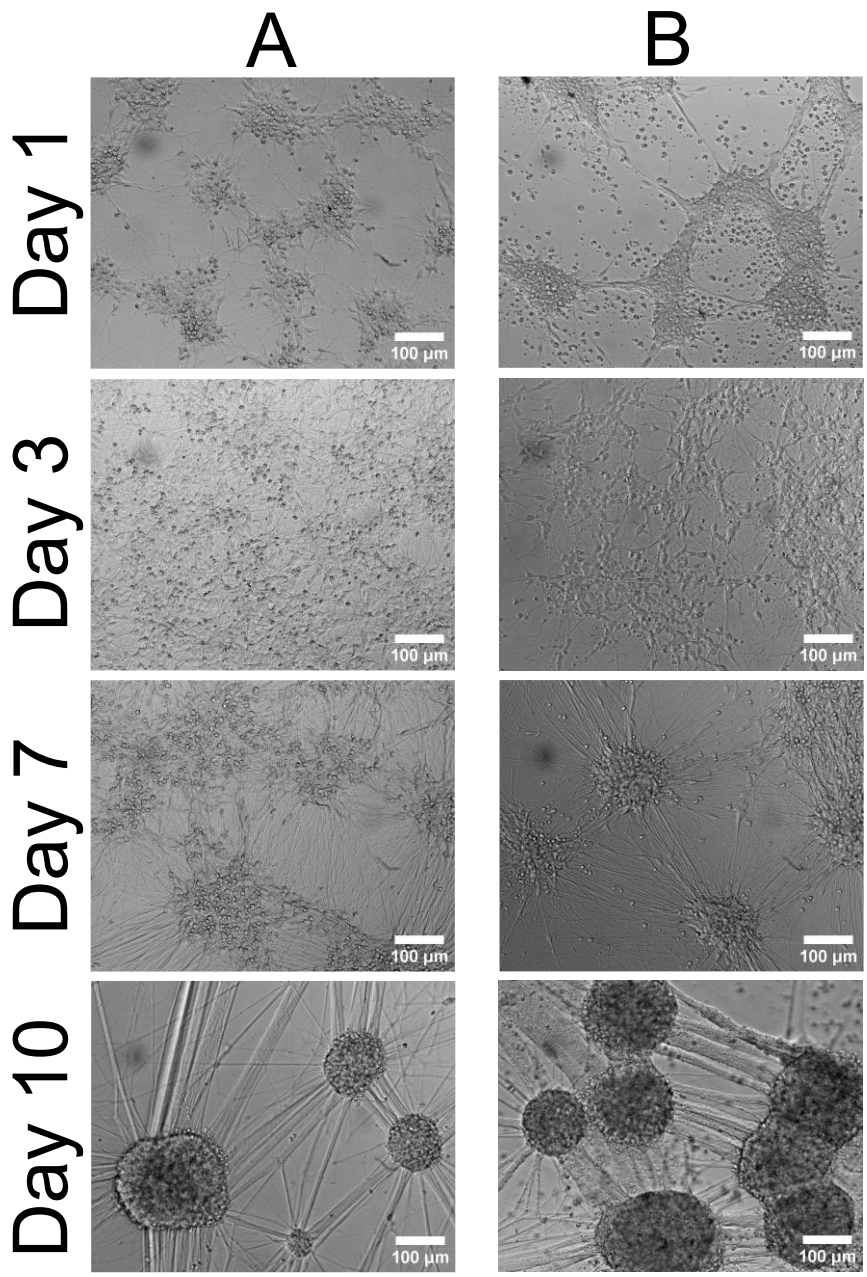

Figure 39. Differentiation of MNPs in a 96-well plate cultured with A) Axol's CMNMM or B) MNDMM.

Figure 39 shows the differentiation of the MNPs under the different media. This time the cells of both conditions looked more similar to each other, which is particularly helpful to help confirm the robustness of the differentiation protocol.

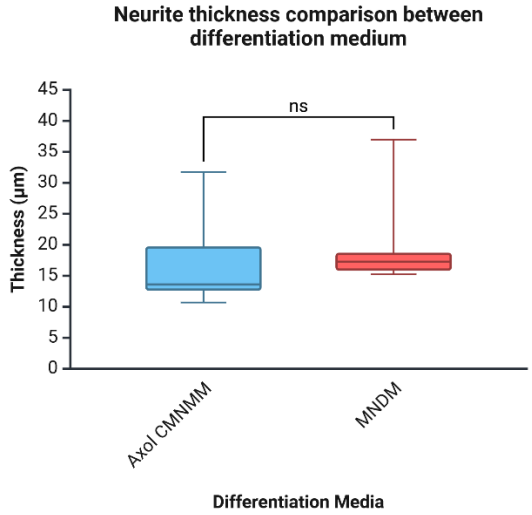

Figure 40. Box and whiskers plot showcasing differences in motor neuron neurite thickness between seeding density and media.

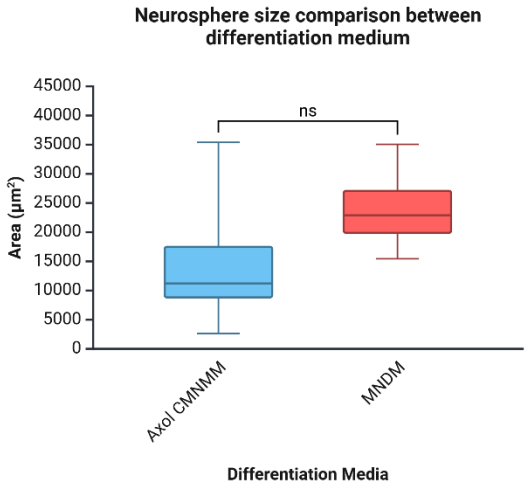

Figure 41. Box and whiskers plot showcasing differences in motor neuro-sphere sizes between differentiation media.

Figures 40 & 41 show plots comparing both differentiation media in neurite thickness and neuro-sphere size. The results show that for day 10 the differences between both conditions are not significant. This supports the robustness of the differentiation protocol of MNDM.

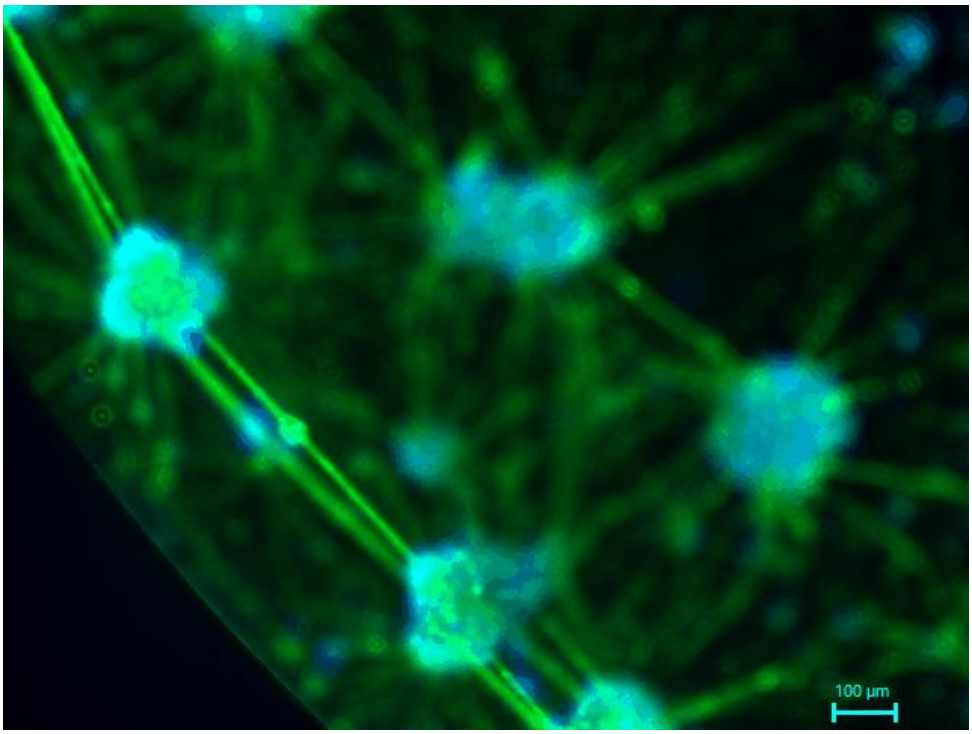

Figure 42. GIF spatial movie through different slices in the Z-axis of the Axol protocol cells differentiated until day 10. Green is MAP2 (neurofilaments) and blue is DAPI (nuclei).

Figure 42 shows the immunostaining result of the MNs with the media of Axol only. Unfortunately, the images of the cells of the MNDM protocol were unavailable. Extrapolating from the results of 010-01, I deduce that a similar figure would also be present for the MNDM protocol (source: my hopeful heart).

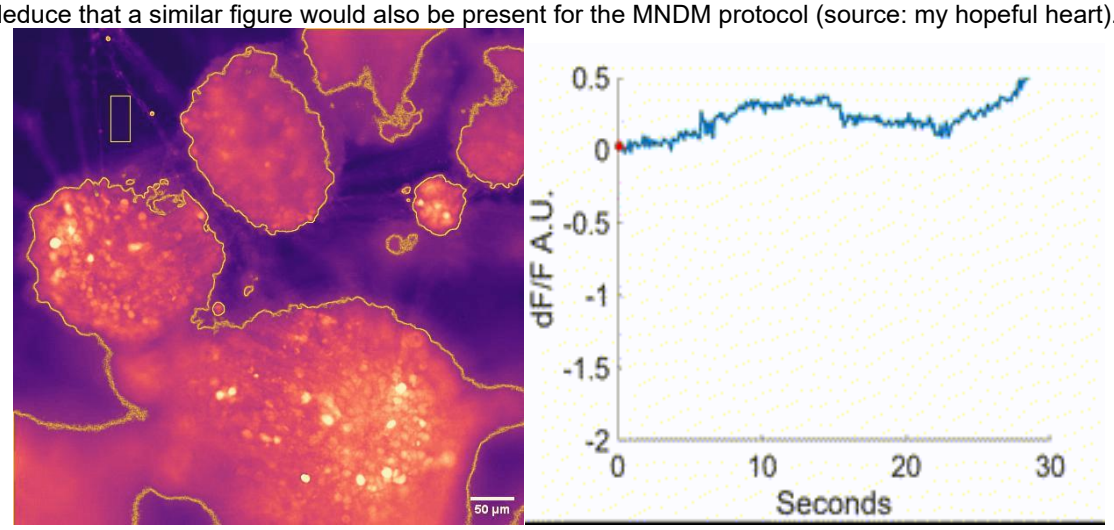

Figure 43. GIF movies of the Axol protocol cells differentiated on day 10 for 30 seconds at 15x speed. Left indicates intensity normalized to background. Intensity of calcium denoted by bright yellow (high intensity) to deep purple (low intensity).

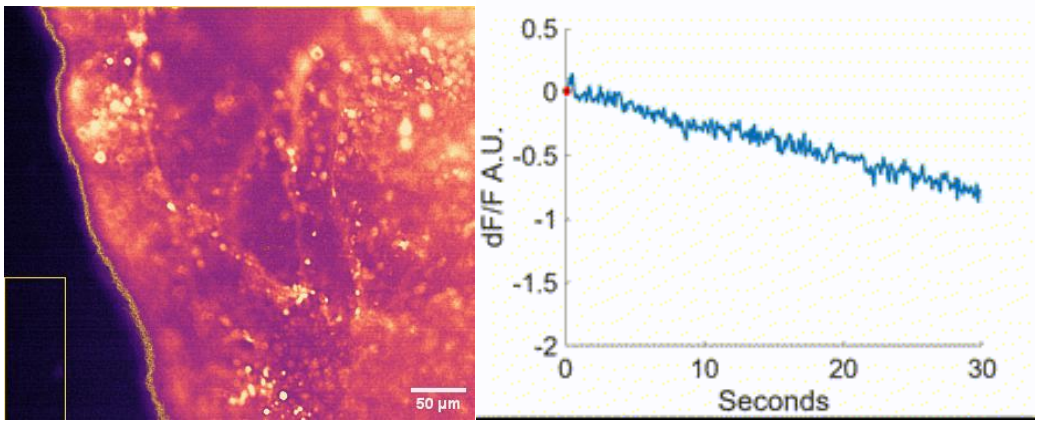

Figure 44. GIF movies of the MNDM protocol cells differentiated on day 10 for 30 seconds at 15x speed. Left indicates intensity normalized to background. Intensity of calcium denoted by bright yellow (high intensity) to deep purple (low intensity).

Figures 43 & 44 show the calcium imaging movies of the 96-well plate for both media conditions. Their respective plots of the calcium imaging intensity of the ROIs normalized to the background intensity are found on the right, the ROI can be seen within a thin yellow line and the background region in a box with yellow outline. This time there was no stimulation, since spontaneous firing was observed, finally. Not only could individual cells be observed firing, but sometimes there were widespread simultaneous firing from a neuro-sphere that propagated to the rest (unfortunately this was not recorded due to happening unexpectedly, but it happened twice). With this result, it can be said that the established protocol can definitively produce neurons capable of spontaneous and simultaneous firing, just as Axol bioscience has done with their protocol.

Objective: Demonstrate a more complete differentiation profile of the MNPs through electrical activity as seen by calcium imaging and immunostaining for neurofilaments. **Results**: MNs were achieved and confirmed via calcium imaging and MAP2 imaging.

6.11 013 – Second passage of the third thawed cryovial

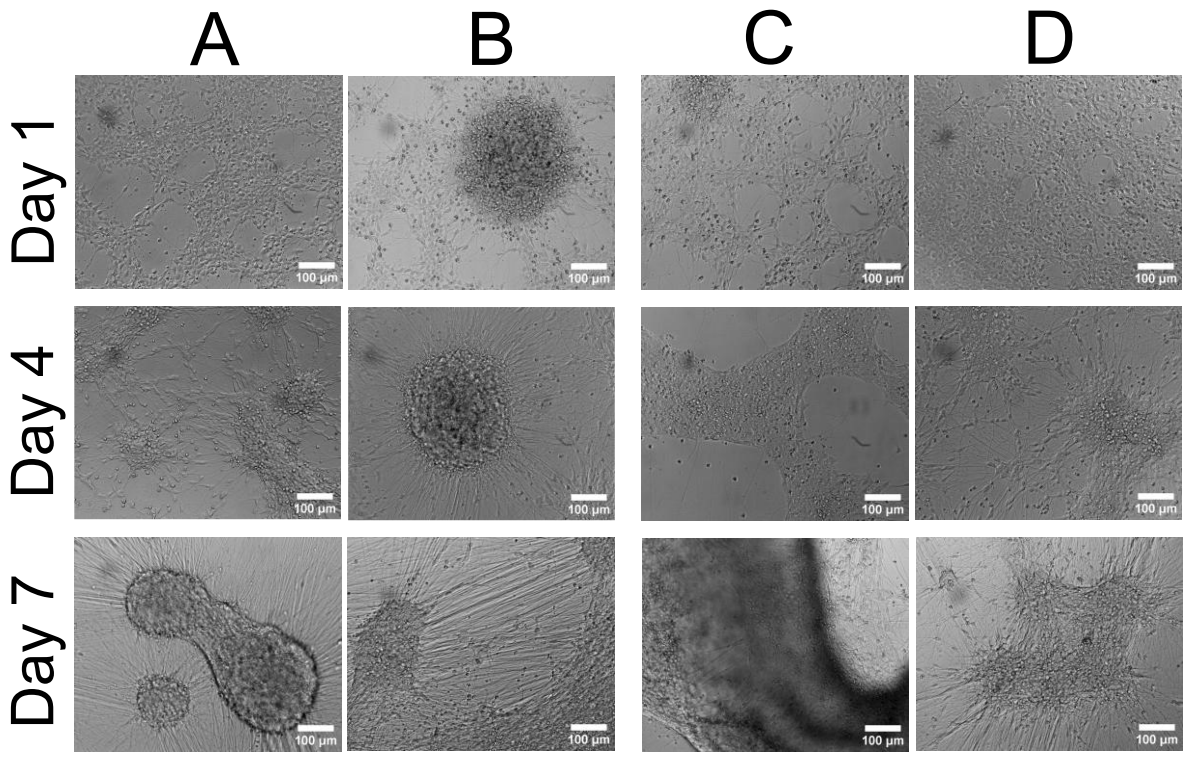

Figure 45. Differentiation of MNPs in a 96-well plate cultured with A) Axol's CMNMM, B) non-fresh CMNMM, C) MNDMM, and D) MNDMM+E since day 1.

Figure 45 shows the differentiation of the MNPs under the different media. For day 7, all the conditions showed the creation of neuro-spheres and neurite growth, however, for the CMNMM and MNDM groups, the cells readily detached. This may be explained for the MNDMM group due to an observed proliferation stage early in development that resulted in a later differentiation stage for the cells; while the CMNMM group had a much faster creation of neuro-spheres that easily detach from the substrate.

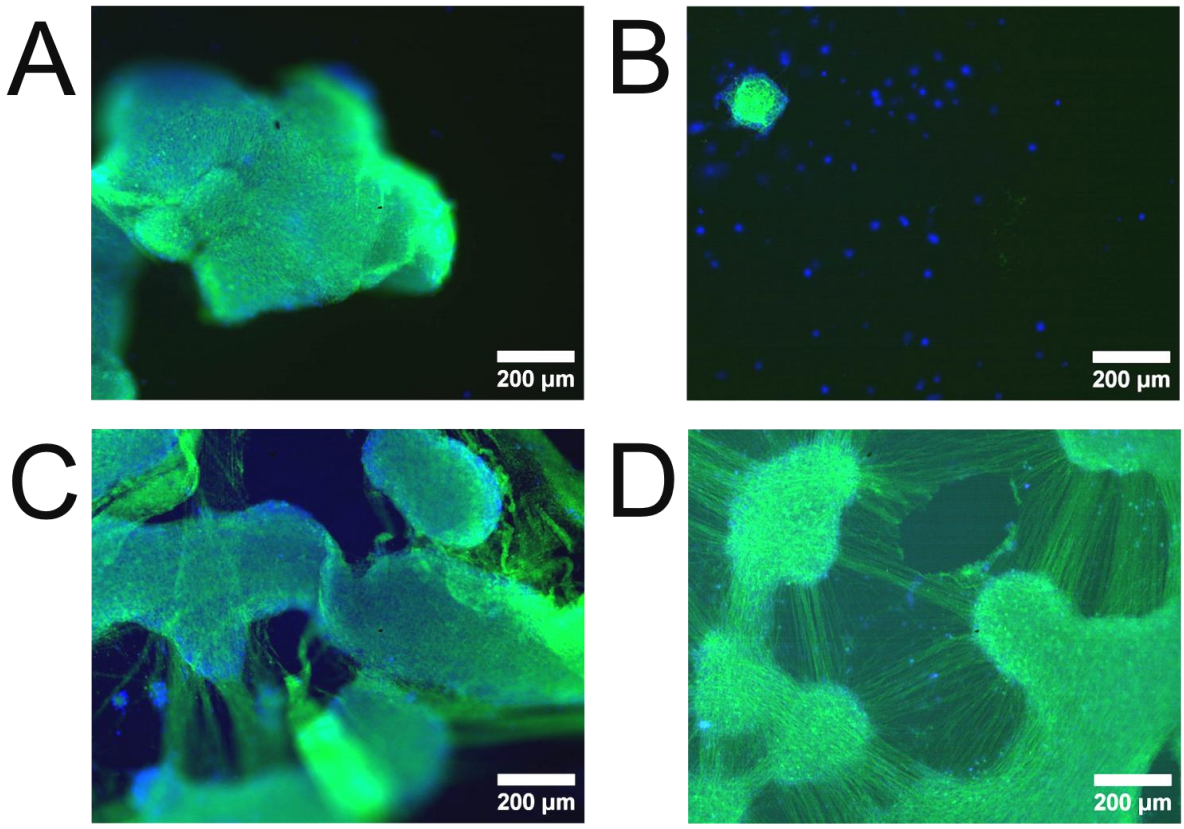

Figure 46. Actin (green) / DAPI (blue) staining for the cytoskeleton and nuclei respectively of the differentiated MNPs on day 7 under A) Axol's CMNMM, B) non-fresh CMNMM, C) MNDMM, and D) MNDMM+E since day 1.

Figure 46 shows the Actin/DAPI staining of the differentiated MNPs on day 7. It can clearly be seen that the CMNMM and non-fresh CMNMM did not have favorable results due to a tendency of the cells to detach from the wells substrate during the staining procedure. Which unfortunately made it hard to appreciate the connections made between the neuro-spheres. Although the MNDM group suffered from the same conditions, it was not to the same extent and the neurites actually helped stabilize the system. Fortunately, MNDM+E group suffered minor mechanical injuries, and the growth of the neurites can clearly be seen. One of the results worth noting is that there are cells growing around the neurites, this has been suspected from the brightfield images inconclusively, so the appearance of nuclei at this stage of differentiation raises the hopes that some MNPs may differentiate into satellite cells. This is, obviously, pure speculation from my part, but it is fun to think that there is a chance of an unintended coculture, which cannot be confirmed without the necessary immunoassays. Back to the point, this last experiment may indicate that after certain passages it may be wise to use such "accelerated" differentiation of the MNPs by adding Compound E from day 1 and avoid "proliferation inertia" of the cells.

Objective 1: Determine if non-fresh media still has a differentiation effect as compared to freshly made. **Results**: Differentiation still happens albeit slower.

Objective 2: Determine if the addition of compound E helps accelerate the differentiation as compared to the established protocol. **Results**: Addition of compound E on day 1 has a faster differentiation than normal MNDM.